

Unraveling the behavior of amagmatic geothermal systems through thermal–hydraulic simulations: insights from the Agua Blanca Fault, Baja California, Mexico

Inaugural dissertation
of the Faculty of Science,
University of Bern

presented by

Daniel Carbajal Martínez

from Mexico

Supervisor of the doctoral thesis:

PD Dr. Christoph Wanner

Co-supervisor:

Prof. em. Dr. Larryn W. Diamond

Institute of Geological Sciences

Unraveling the behavior of amagmatic geothermal systems through thermal–hydraulic simulations: insights from the Agua Blanca Fault, Baja California, Mexico 2023 by Daniel Carbajal Martinez is licensed under Attribution 4.0 International. To view a copy of this license, visit <http://creativecommons.org/licenses/by/4.0/>

**Unraveling the behavior of amagmatic geothermal systems through
thermal–hydraulic simulations: insights from the Agua Blanca Fault,
Baja California, Mexico**

Inaugural dissertation
of the Faculty of Science,
University of Bern

presented by

Daniel Carbajal Martínez

from Mexico

Supervisor of the doctoral thesis:
PD Dr. Christoph Wanner
Co-supervisor
Prof. em. Dr. Larryn W. Diamond

Accepted by the Faculty of Science.

Bern, 15.11.2023

The Dean
Prof. Dr. Marco Herwegh

Acknowledgments

I would like to express my sincere gratitude to my PhD supervisors, Christoph Wanner and Larryn Diamond, for their consistent guidance and for generously sharing their knowledge throughout my three years and three months of doctoral studies. They played a crucial role in shaping both the research presented in this thesis and my professional growth.

I first crossed paths with Christoph five years ago during a geothermal exploration campaign in Mexico, and since then, he has been an essential part of my professional life. When Christoph invited me to pursue my PhD studies in Switzerland, I enthusiastically accepted the offer, recognizing it as a unique opportunity to delve deeper into the understanding of amagmatic geothermal systems and to access a high level of education. Consequently, four years ago, I made my first trip to Switzerland to meet Larryn and present the results of my master's studies. Subsequently, both Christoph and Larryn agreed to be my doctoral advisors. However, the project was not guaranteed. Together, we drafted a research proposal to compete for the prestigious Swiss Government Excellence Scholarships, and our efforts bore fruit when the Eidgenössische Stipendienkommission für ausländische Studierende (ESKAS) approved the project. In September 2020, I began my doctoral journey. Therefore, I extend my gratitude to my supervisor and ESKAS for supporting my research project and providing the necessary financial, educational, and cultural resources to ensure the success of my doctoral studies under the best possible conditions.

I would like to express my gratitude to the co-authors of the research papers included in this thesis. A special thanks to Loïc Peiffer, who has been a guiding force and mentor since my master's studies when he served as my supervisor. I would also like to extend my thanks to Maren Brehme for agreeing to be a part of my thesis committee and to Marco Herwegh for chairing my doctoral defense. The University of Bern and its exceptional educational standards, as well as the professors who shared their knowledge through various courses, deserve my deepest gratitude. Special thanks to Jasmin Fahalli (ESKAS) and Sarah Antenen (UNIBE) for their invaluable assistance with administrative matters. A special thanks to my friends for their support during our countless discussions, celebrations and trips greatly enriched my international experience.

Last but absolutely paramount, I want to express my deep gratitude to my family, especially Karen. Living far from my family has never been easy but their unwavering love, and support throughout this journey have been my constant source of strength. Thank you all.

Summary

In view of the ongoing global challenges such as climate change, it is crucial to explore and develop energy sources that are sustainable. Amagmatic orogenic geothermal systems, situated within crystalline rocks along fault zones in regions that lack recent magmatic activity, represent promising renewable energy sources for heat exploitation and power generation. The reservoir temperatures in these systems can reach as high as 250 °C, even in the absence of a magmatic heat source. This remarkable thermal potential is due to heat transport by water that circulates deeply through fault networks. Previous studies have provided valuable insights into the behavior of such systems, but better understanding is required to enable effective exploration and assessment of their energy potential.

The main goal of this thesis is to provide a detailed description of the key parameters controlling the behavior of amagmatic orogenic geothermal systems, and thereby contribute to broader efforts to develop sustainable energy resources. To achieve this goal, multidisciplinary research techniques were employed, including geological, geochemical, and geophysical analyses, all integrated via thermal–hydraulic numerical simulations. The thesis is divided into three main parts: (i) introduction (Chapters 1 and 2), (ii) research papers (Chapters 3-6), and (iii) concluding remarks (Chapter 7). The research papers form the core of the thesis and cover three main topics:

- Topic I. Characterization of geothermal systems along the Agua Blanca Fault (ABF) in Baja California, Mexico (Chapter 3):

In the initial phase, thermal waters and dissolved gases were sampled from seven hot spring sites strung along a 90 km segment of the ABF. A combination of geochemical, petrophysical, and seismic hypocenter data with previous geodetic studies resulted in a conceptual model that explains the governing processes controlling these amagmatic geothermal systems. Hydraulic head gradients caused by the surface topography drive meteoric water deep into the fault system, where it is heated by the background geothermal gradient. Where the ABF crosscuts the Pacific coast, thermal springs are mixtures of infiltrated meteoric water and seawater. Geochemical analyses show that all the discharging thermal waters equilibrated with quartz at 100–220 °C, deep within the host fault. Accordingly, meteoric water has been deduced to have infiltrated to depths of at least 5–11 km into the brittle crust. Subsequently, the infiltrated water has ascended along preferentially permeable zones of the host fault system, eventually discharging in thermal springs at temperatures ranging from 37 °C at inland sites to 102 °C on the Pacific coast.

Notably, higher spring temperatures correlate positively with the degree of extensional displacement along the fault system, which serves as a proxy for fault permeability. All systems have a mantle He contribution ranging from 1–11% based on ^3He measurements, confirming its amagmatic origin. Correlations between hydraulic head gradients, residence times, and $^3\text{He}/\text{He}_{\text{total}}$ ratios of the thermal waters show that the hydraulic head gradient controls the length and depth of the flow paths. These findings reveal that the permeability of the ABF and its hydraulic head gradients are the key factors controlling the behavior of amagmatic orogenic geothermal systems.

- Topic II. 3D simulations of the La Jolla Beach system (Chapters 4 and 5):

The hottest subaerial geothermal system along the ABF is at La Jolla Beach. This system discharges thermal water up to 94 °C at the coastline, with a seawater content between 15 and 50%, and a mantle He contribution of less than 3%. The high discharge temperature at the beach, which to our knowledge is the hottest recorded in amagmatic systems worldwide, is attributed to a combination of factors, including the location of the spring within the highest permeability segment along the ABF and its location near a mountainous region of the coastline (up to 1 km in elevation). To gain deeper insights into the behavior of the La Jolla Beach system, three-dimensional (3D) thermal–hydraulic simulations using the software TOUGHREACT were performed for this case study. These simulations were conducted on a regional scale (up to $34 \times 12 \times 11.5$ km), including the topography and bathymetry of the study area to assess their role in controlling regional water circulation within the ABF. To constrain the simulations, the location, temperature, and salinity of the hot springs, and fault extension observed at La Jolla Beach were compared with the corresponding simulation results. Two distinct numerical simulation scenarios were explored:

(i) The first scenario considers the presence of a preferential upflow zone right beneath La Jolla Beach, within the ABF. (ii) The second scenario considers a more extended dataset, including the topography of the crystalline basement and the sediment distribution on the seafloor, based on previous studies. Moreover, this scenario accounts for not only the pressure of the seawater column but also the density and viscosity of seawater, both of which are temperature-dependent.

The results of the first scenario show that assuming the presence of a highly permeable upflow zone beneath La Jolla Beach is sufficient to match the observed discharge temperature at the right location. This demonstrates the importance of permeability in controlling the

discharge temperature of amagmatic geothermal systems.

The second simulation scenario shows that the discharge temperature observed at La Jolla Beach can also be matched at the right location without having to define a highly permeable upflow zone. To do so, the permeability of the entire ABF, as well as the permeability of the seafloor sediments that control the infiltration of seawater into the brittle continental crust, need to be taken into account. This scenario thus highlights the crucial role of dense seawater, which acts as a hydraulic barrier that forces thermal discharge right at the coast. In conclusion, the record high discharge temperature observed at La Jolla Beach likely results from the presence of a structural (i.e., permeability) anomaly within the host fault precisely at the coast where the hydraulic head is at its minimum. The combination of high hydraulic head gradients and elevated permeability leads to very high upflow rates and discharge temperatures of almost 100 °C despite the absence of any magmatic activity.

- Topic III: Functioning of global coastal geothermal systems (chapter 6):

The intriguing observations and numerical results of La Jolla Beach provided the motivation to explore whether other coastal geothermal systems worldwide behave in the same way. The results of generalized 3D thermal-hydraulic simulations using TOUGHREACT show that seawater incursion consistently blocks the seaward flow of groundwater through faults that intersect a coastline. This feature, combined with the hydraulic effects of fine-grained, low-permeability sediments that typically blanket the fault trace along the seafloor, systematically leads to discharges of thermal water at the coastline.

In conclusion, this doctoral thesis enhances our understanding of amagmatic orogenic geothermal systems, emphasizing the importance of factors like fault permeability, hydraulic head gradients, and the presence of permeability anomalies, but also highlights that they could form substantial thermal anomalies within the rocks surrounding the upflow zones. The findings suggest that sustainable energy exploration should prioritize valley floors and coastal zones intersected by regional fault zones. Under such ideal conditions with high hydraulic head gradients and elevated permeabilities, amagmatic geothermal systems lead to thermal anomalies within which the critical temperature threshold for power production (120 °C) is reached at shallow depths (<2 km). Exploitation of this largely petrothermal heat could constitute a significant sustainable energy source.

Contents

Part 1: Introduction	9
1. Preface.....	10
1.1. Context	10
1.2. Aim of the study	11
1.3. Thesis outline	12
2. Background.....	14
2.1. Geothermal energy	14
2.2. Plate tectonics and geothermal systems	15
2.3. Hydraulic driving force	20
2.4. Key hydraulic rock properties influencing fluid flow	21
2.5. Fault zone architecture	23
2.6. Thermal–hydraulic numerical simulations.....	25
Part 2: Research papers	31
3. Behavior of amagmatic orogenic geothermal systems: insights from the Agua Blanca Fault, Baja California, Mexico.....	32
Abstract	32
Plain Language Summary	33
3.1. Introduction	33
3.2. Materials and Methods	39
3.3. Results	44
3.4. Discussion	56
3.5. Summary and conclusions.....	65
Acknowledgments	66
Supplementary data	66
4. La Jolla Beach amagmatic geothermal system, Baja California, Mexico: controls on the thermal anomaly from 3D thermal–hydraulic simulations	67
Abstract	67
4.1. Introduction	68
4.2. Numerical simulator	71
4.3. Results and discussion.....	75
4.4. Conclusion.....	81
4.5. Acknowledgments.....	81
Supplementary data	81

5. Behavior of coastal amagmatic geothermal systems: modeling insights from La Jolla Beach, Baja California, Mexico.....	82
Abstract	82
Plain Language Summary	83
5.1. Introduction	83
5.2. Numerical simulations methodology	88
5.3. Results	96
5.4. Discussion	105
5.5. Conclusion.....	111
Acknowledgments	112
Supplementary data	112
6. Hot springs on ocean beaches: a global phenomenon	113
Abstract	113
6.1. Introduction	114
6.2. Model setup.....	117
6.3. Seawater as a hydraulic barrier	119
6.4. Influence of seafloor sediments.....	120
6.5. Conclusion.....	122
Acknowledgements	123
Supplementary data	123
6.6. Methods.....	124
Part 3: Concluding remarks	127
7. Conclusions.....	128
References.....	130
Declaration of consent.....	148
Curriculum vitae.....	148

Part 1: Introduction

1. Preface

On a global scale, human activity has led to the accumulation of greenhouse gases in the Earth's atmosphere, causing an increase of the Earth's surface temperature over the last century. To mitigate the phenomenon of global warming, the Paris Agreement proposes a transformative approach, based on the latest and most reliable scientific knowledge (COP21, 2015). Among the diverse scientific insights, renewable energy sources play a crucial role in addressing global warming. Geothermal energy, in particular, stands out as a promising and environmentally friendly alternative. This energy source harnesses the Earth's natural heat, which is then utilized to generate electricity and/or provide heating for industrial and residential purposes. As part of this vision, the present doctoral research aims to contribute to understanding the behavior of amagmatic orogenic geothermal systems. The results should enhance the success of exploration and exploitation of these energy resources, promoting an eco-friendly and sustainable future.

1.1. Context

Amagmatic geothermal systems occur in mountainous orogenic regions without recent magmatic activity. They are manifested by hot springs, which are spatially associated with regional-scale faults. The springs represent the discharge points of meteoric water that infiltrates at high altitudes, penetrates deep into the fault plane where it acquires heat from the wall rocks, and then rises through preferentially permeable upflow zones to low points in the valley floors or coastal zones (Diamond et al., 2018). These fault-hosted, topography-driven systems have been documented in various locations worldwide. They exhibit distinct regional crustal geothermal gradients, typically ranging from 20 to 30 °C km⁻¹, and reservoir temperatures of 100–250 °C, resulting in discharge temperatures up to 102 °C.

Despite their potential, amagmatic orogenic geothermal systems have received limited attention in past research (Wanner et al., 2019; Guillou-Frottier et al., 2023). To successfully explore and exploit these systems, understanding the topography of mountain ranges and the permeability of fault zones is crucial, as they act as driving forces and preferential pathways for fluid flow (Taillefer et al., 2018; Alt-Epping et al., 2022). The permeability of fault zones can be influenced by mineral precipitation–dissolution processes and tectonic-fault activity, which in turn affect the lifespan and fluid circulation of geothermal systems (Renard et al., 2000; Ingebritsen & Manning, 2010).

Previous investigations into amagmatic orogenic geothermal systems have provided valuable insights into the circulation of meteoric water within fault zones (López & Smith, 1995; Taillefer et al., 2018; Wanner et al., 2019; Alt-Epping et al., 2022). These studies have collected geochemical and structural information on these systems and employed thermal–hydraulic (TH) numerical simulations to constrain some of the major processes. However, significant knowledge gaps persist in our comprehension of amagmatic geothermal systems, which the present thesis aims to bridge. These gaps include quantification of the factors that control their behavior and formation, such as the temporal evolution of hydraulic gradients induced by topographic relief, the distribution and evolution of fault zone permeability, and the changing rates of heat and solute transfer from and to the rocks along the flow paths. Understanding the complexity of the rock–water interaction in these geothermal systems requires quantitative models that capture the coupling of hydraulic, thermal, chemical and mechanical processes through space and time. Whereas suitably comprehensive numerical modeling codes are being developed for this task, there remain many barriers to their realistic implementation, due to the difficulty of measuring or estimating the necessary input parameters in deep-reaching, tectonically active fault zones. Nevertheless, progress can be made at present by creatively using surface observations to calibrate three-dimensional, time-resolved numerical simulations that involve at least some of the key thermal–hydraulic couplings (e.g., Wanner et al., 2019). This is the approach adopted in the current study.

1.2. Aim of the study

The primary goal of this doctoral research is to conduct a comprehensive investigation into the behavior of amagmatic orogenic geothermal systems by focusing on the geothermally and tectonically active Agua Blanca Fault (ABF) in Baja California, Mexico. This research employs a multidisciplinary approach, integrating geological, geophysical, and geochemical data collected from the hot springs and rocks along the ABF. This dataset permits the development and implementation of 3D thermal–hydraulic simulations of the coastal geothermal systems at La Jolla Beach. As far as is possible, the simulations are constrained by field observations, but inevitably some assumptions need to be made. La Jolla beach turns out to be a prime example of a global phenomenon, whereby hot springs preferentially occur where the host orogenic fault intersects a coastline. Based on this finding, generalized simulations are performed to elucidate the underlying processes controlling this phenomenon, with implications for exploration for

geothermal energy.

Specific research questions addressed in this thesis are listed as follows:

- What are the key processes and variables that govern the spatial distribution of amagmatic systems?
- What is the role of preferential permeability pathways as well as hydraulic head gradients in shaping the thermal anomalies formed by amagmatic systems?
- What are the dominant mechanisms that control the location, temperature, salinity, and spatial extent of coastal amagmatic geothermal systems?

1.3. Thesis outline

This thesis is structured into six chapters:

- (i) Chapters 1-2 provide an introductory overview of geothermal systems, with a specific focus on amagmatic orogenic systems. It delves into the fundamental concepts of geothermal energy and the unique characteristics of different types of geothermal systems. Additionally, this background Chapter introduces selected key parameters controlling the behavior of amagmatic orogenic systems such as hydraulic head gradients, rock permeability, fracture porosity, thermal conductivity and fault architecture zone. Finally, the chapter emphasizes the importance of coupled, thermal–hydraulic numerical simulations that take into account the temperature dependence of water properties such as density and viscosity, in order to gain a deeper understanding of the behavior and dynamics of amagmatic orogenic geothermal systems. Thus, this Chapter provides the theoretical principles applied in the subsequent research chapters of the thesis.
- (ii) Chapters 3-6 are manuscripts that have or will be submitted to international, peer-reviewed journals. Chapter 3 presents a detailed exploration and characterization of the chosen study area, the Agua Blanca Fault in Baja California, Mexico. This Chapter presents geological, geochemical, and geophysical data that characterize seven orogenic amagmatic geothermal systems along the ABF. The Chapter also details the data collection (thermal water-gas and rock samples), methods, and instrumentation used in the study. The main outcome of the chapter is the formulation of a conceptual model describing the deep-water circulation and heat transfer mechanisms within the fault. It highlights the interplay of variable hydraulic head gradient and fault permeability controlling the behavior of the amagmatic geothermal systems along the ABF. The information and insights of this Chapter serve as a basis for the

two modeling studies presented in Chapters 3 and 4.

- (iii) Chapter 4 shows large-scale 3D thermal–hydraulic simulations conducted on the coastal amagmatic geothermal system of La Jolla Beach. These simulations aim to investigate the influence of surface topography, nearshore seafloor bathymetry and preferential permeable pathways on the remarkably high discharge temperatures (94 °C) at La Jolla Beach. Modeling results indicate that fluid upflow is controlled by the hydrostatic pressure from surface topography and the Pacific Ocean, and by the occurrence of highly permeable pathways forming preferential channels for thermal water discharge right beneath La Jolla Beach.
- (iv) Chapter 5 presents large-scale 3D thermal–hydraulic simulations of La Jolla Beach explicitly considering seawater density and viscosity, the distribution of unconsolidated sediments across the study area, the depth to the crystalline basement, and the local degree of tectonic extension of the ABF. The simulations are constrained by the observed temperature, salinity, extension, and location of the La Jolla Beach system. The aim is to understand why thermal water specifically discharges along the coastal zones. The simulations reveal a strong coupling of different processes. For instance, infiltrated seawater through the ABF essentially serves as a boundary that limits the circulation of meteoric water. However, the presence of sediments comes into play, reducing the quantity of infiltrated seawater and controlling the location of thermal water discharge right at the coastal zone. Moreover, the permeability of the fault significantly governs the upflow rate and temperature of the discharged thermal water. Consequently, the simulations demonstrate that the infiltration of meteoric water preferentially occurs through the ABF and not through the host rock.
- (v) Chapter 6 analyzes the worldwide distribution of coastal geothermal systems through a simplified 3D model setup in order to unravel the factors governing their behavior and location precisely at the intersection of the host fault with the coastline. The synthetic simulations show that coastal geothermal systems are strongly influenced not only by hydraulic gradients imposed by the inland topography but also by deep incursion of seawater into the permeable fault networks. Their precise location at the coastal zone depends on two main factors, the ocean acting as a hydraulic barrier for freshwater flow and the seafloor sediments acting as aquitards for seawater infiltration. Simulations reveal that these systems exceed the critical temperature threshold for power production of ~2 km below the coastline.
- (vi) Chapter 7 summarizes the main findings on the behavior of amagmatic orogenic geothermal systems presented in this thesis.

2. Background

2.1. Geothermal energy

Geothermal energy represents a promising source of constant, sustainable and renewable energy stored in the Earth. Over 99% of the Earth's volume has temperatures exceeding 1000 °C, and only 0.1% is colder than 100 °C (Stober & Bucher, 2013). To take advantage of this resource, geothermal power plants are required. Geothermal energy is used in various applications, such as electricity generation, space heating and cooling, aquaculture, drying of fruit, and melting of snow for freshwater supplies (Lund & Toth, 2021).

The dynamic interplay of conductive heat flow and radiogenic decay within the Earth's interior continually replenishes geothermal energy. The core of the Earth is at extremely high temperature (~5000 °C), generated by the decay of radioactive isotopes and the residual energy from initial gravitational compaction of the planet (Stober & Bucher, 2013). The average surface temperature of the Earth is 14 °C, whereas the temperature at the core-mantle boundary at ~3000 km depth is around 3000 °C. This temperature differential drives the global heat flow (Figure 2.1), with an average of 67 mW m⁻² for continents and 92 mW m⁻² for the ocean floor (Lucazeau, 2019). As a result, the Earth loses heat at a rate of 41–42 terawatts per year (Pollack et al., 1993; Lay et al., 2008; Lucazeau, 2019).

Despite its immense potential, the current use of geothermal energy for power generation is relatively small. With an installed capacity of 16127 MW in 2023 (ThinkGeoEnergy, 2022), just 0.04% of the Earth's total heat loss is currently harnessed. This highlights the vast, untapped potential of geothermal energy. Geothermal exploration normally focuses on regions manifesting surface evidence of the Earth's internal heat, such as volcanic centers and mid-ocean ridges exhibiting strong heat flow anomalies (Figure 2.1). However, the movement of fluids, notably thermal groundwater upwelling in regions with lower heat flow, is also important. These fluids transport heat by advection of meteoric water, resulting in significant shallow thermal anomalies below their discharge sites (Stober & Bucher, 2013).

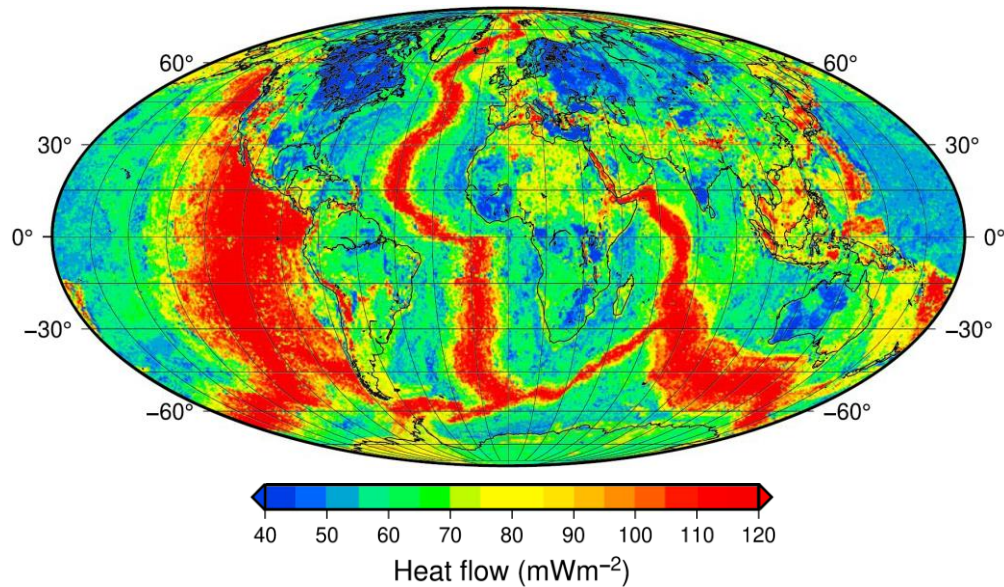


Figure 2.1. Heat flow map of the Earth taken from [Lucazeau \(2019\)](#).

2.2. Plate tectonics and geothermal systems

Plate tectonics determines the distribution and features of geothermal systems across the Earth (Figure 2.2). The crust of the Earth is segmented into three primary types of plate boundaries: divergent boundaries, where new oceanic plate material is created through seafloor spreading along mid-ocean ridges; convergent boundaries, where old oceanic lithosphere sinks into the Earth's mantle through subduction zones; and transform boundaries, where two plates slide past each other along faults ([Stern, 2018](#)). These distinct settings influence various aspects of geothermal systems, including the thermal regime and heat flow, the types of rocks present, stress regime, fault types, hydrogeologic and fluid dynamics, and the chemistry of the fluids involved ([Stober & Bucher, 2021](#)).

Geothermal systems exhibit unique surface characteristics, which are reflected in their fluid temperature, flow rate, solute chemistry, and in their potential applications. They can be classified into two main types: (i) geothermal systems in magmatically active provinces, including volcanic arcs and mature, active tectonic rifts; and (ii) amagmatic geothermal systems, which comprise basin-and-range extensional provinces (incipient rifts) and orogenic belts with mountainous topography (Figure 2.3) ([Jolie et al., 2021](#)). The magmatic systems derive thermal energy from magmatic heat sources, while amagmatic systems involve the circulation of meteoric water through fractures and faults, gaining heat from the background geothermal gradient.

2.2.1. Magmatic geothermal systems

Magmatic geothermal systems are predominantly found at active plate margins, where volcanic activity and crustal extension generate a high heat flux ($>200 \text{ mW m}^{-2}$). These systems derive their energy from magmatic heat sources ($>250 \text{ }^\circ\text{C}$), where meteoric water infiltrates and mixes with magmatic fluids, resulting in a reservoir fluid dominated by liquid and/or vapor phases (Figure 2.3) (Nicholson, 1993).

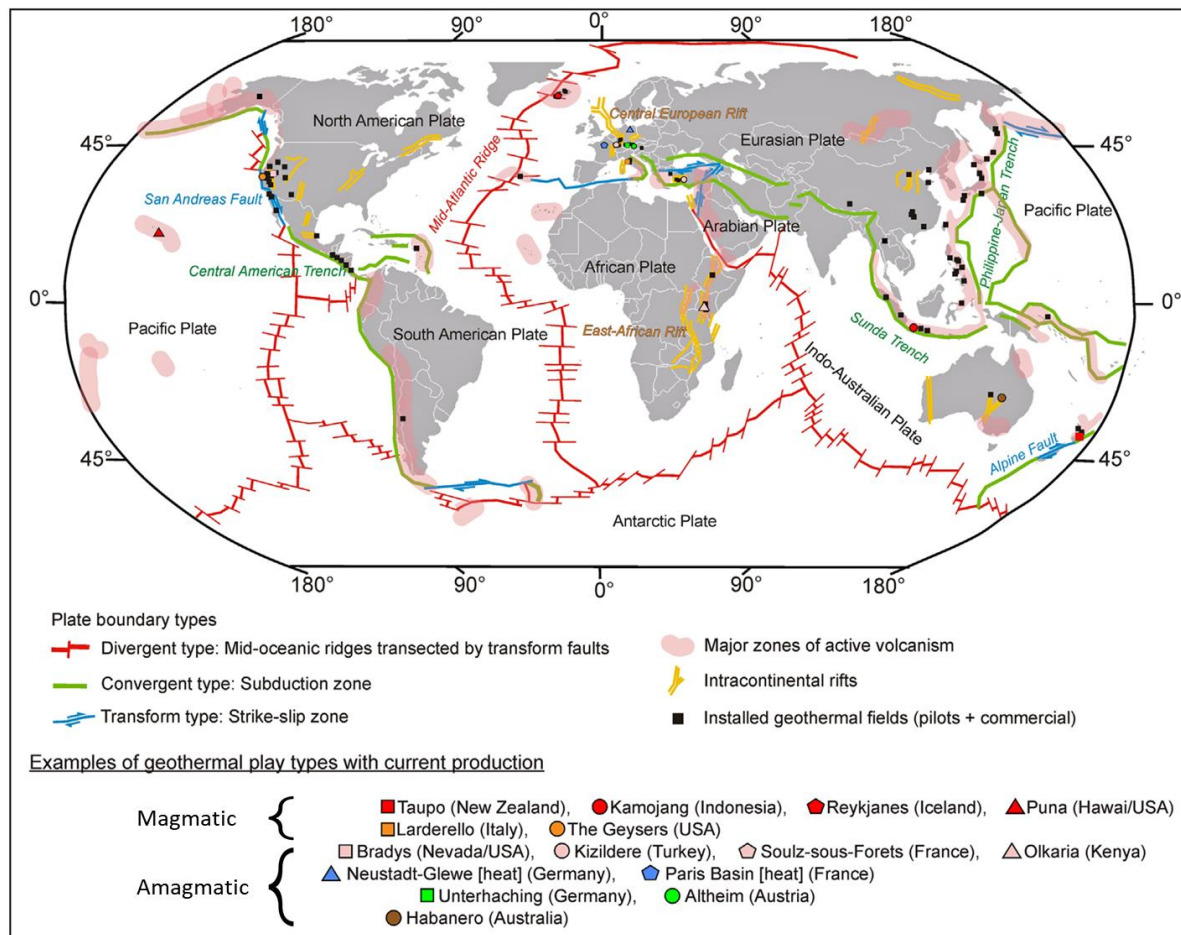


Figure 2.2. Worldwide distribution of geothermal fields and plate tectonic setting of the Earth. The geothermal fields are grouped into two categories magmatic and amagmatic systems. Modified from Moeck (2014).

The behavior of magmatic geothermal systems is influenced by three key factors: the magmatic heat source, topographic relief, and the permeable structures within these systems. These factors determine the fluid flow patterns, the distribution of alteration zones, and the types of fluid discharge (Nicholson, 1993). In areas with relief from arc volcanoes, lateral fluid

migration occurs, resulting in the frequent discharge of chloride-rich water ($>1000 \mu\text{g/g}$) from hot springs and geysers (Giggenbach, 1989). On the other hand, mature rifts with crustal thinning and low topographic relief at their centers create ideal conditions for the upflow of magmatic fluids. In this zone, chloride-rich water may mix with seawater, forming brines ($\text{Cl} > 10,000 \mu\text{g/g}$), while sulfate-rich water is found in lateral downflow zones of the system (Figure 2.3) (Truesdell et al., 1981).

Additionally, magmatic geothermal systems commonly emit gases such as CO_2 , H_2S , NH_3 , N_2 , H_2 , HCl and HF , with carbon dioxide and hydrogen sulfide being the main gases representing over 90% of the gas content (Scarpa et al., 1996). The mixture of magmatic gases and water causes significant changes to the original mineralogy of host igneous and country rocks, producing extensive alteration haloes. A typical surface alteration type is called argillitic, where acidic sulfate-rich water transforms the host rock into an a clay assemblage including kaolinite, smectite, and illite (Nicholson, 1993) and other minerals such as alunite and chalcedony. The magmatic heat can also mobilize pore-waters in the distal country rocks of intrusive complexes, leading to low-sulfidation (reduced redox, neutral pH, gas-poor) hot-spring discharges.

Examples of magmatic geothermal systems include Cerro Prieto in Mexico, Imperial Valley, The Geysers, and Roosevelt Hot Springs in the USA, Taupo Volcanic Zone in New Zealand, Awibengkok in Indonesia, the Kyushu volcanic arc in Japan, and Iceland (Figure 2.2) (Moeck, 2014).

2.2.2. Amagmatic geothermal systems

Amagmatic orogenic geothermal systems involve the circulation of meteoric water through fractures and faults, in response to topographically induced hydraulic gradients, whereby the water gradually gains heat as it penetrates deeper into the Earth (Alt-Epping et al., 2021). However, it is important to distinguish between two types of amagmatic geothermal systems, amagmatic extensional geothermal and amagmatic orogenic geothermal systems.

Amagmatic extensional geothermal systems are characterized by topographically driven circulation of surface water through faults and sedimentary units. These systems emerge in regions where continental-scale extension triggers crustal thinning, consequently leading to elevated heat fluxes. For example, in the northwestern part of the Basin and Range Province in western North America, these extensional geothermal systems have a heat flux of $85 \pm 10 \text{ mW}$

m^{-2} (Kennedy & Van Soest, 2007; McKenna & Blackwell, 2004).

In contrast, amagmatic orogenic geothermal systems present a different paradigm. They involve deep circulation of meteoric water through faults in crystalline rock, with an average crustal geothermal gradient ($<30\text{ }^{\circ}\text{C km}^{-1}$) and average heat flux values ($<65\text{ mW m}^{-2}$). The circulation of water is restricted to the upper crust above the brittle–ductile transition zone typically occurring at depths of 12–15 km. Owing to crystalloplastic deformation, the permeability beneath the brittle–ductile transition zone is very low, thereby restricting advective fluid flow to the upper, brittle part of the crust. Examples of amagmatic orogenic geothermal systems include the Canadian Rocky Mountains (Grasby & Hutcheon, 2001) and the Eastern Pyrenees in France (Taillefer et al., 2018).

Amagmatic geothermal systems are characterized by discharge of thermal water at the surface, often observed in the form of hot springs and fumaroles. The concentration of total dissolved solids is usually lower than in magmatic systems. Additionally, the infiltrated meteoric water carries dissolved gases, with nitrogen accounting for over 95% of the gas content. Diamond et al. (2018) have shown that meteoric water can penetrate up to 10 km deep into an orogenic system, reaching temperatures as high as $250\text{ }^{\circ}\text{C}$ even the absence of a magmatic heat source. The temperature that amagmatic geothermal systems can achieve is primarily influenced by fault permeability ($k_{\text{fault}} > 10^{-15}\text{ m}^2$), because it controls the depth of water infiltration and the discharge temperature (Moeck, 2014; Taillefer et al., 2018; Alt-Epping et al., 2022).

The capability to generate high temperatures without needing volcanic heat sources makes amagmatic geothermal systems attractive for exploration, as they can potentially be found wherever there is high topographic relief cut by fault zones. However, it is important to note that these systems have limitations, including relatively low rates of both heat and fluid flow ($<10\text{ L min}^{-1}$) (Diamond et al., 2018). They may therefore be better suited to petrothermal heat extraction (whereby the plume of hot rock around the water upflow zone is exploited via permeability stimulation and injection of water), rather than direct use of the heat carried by the discharging hot-spring water.

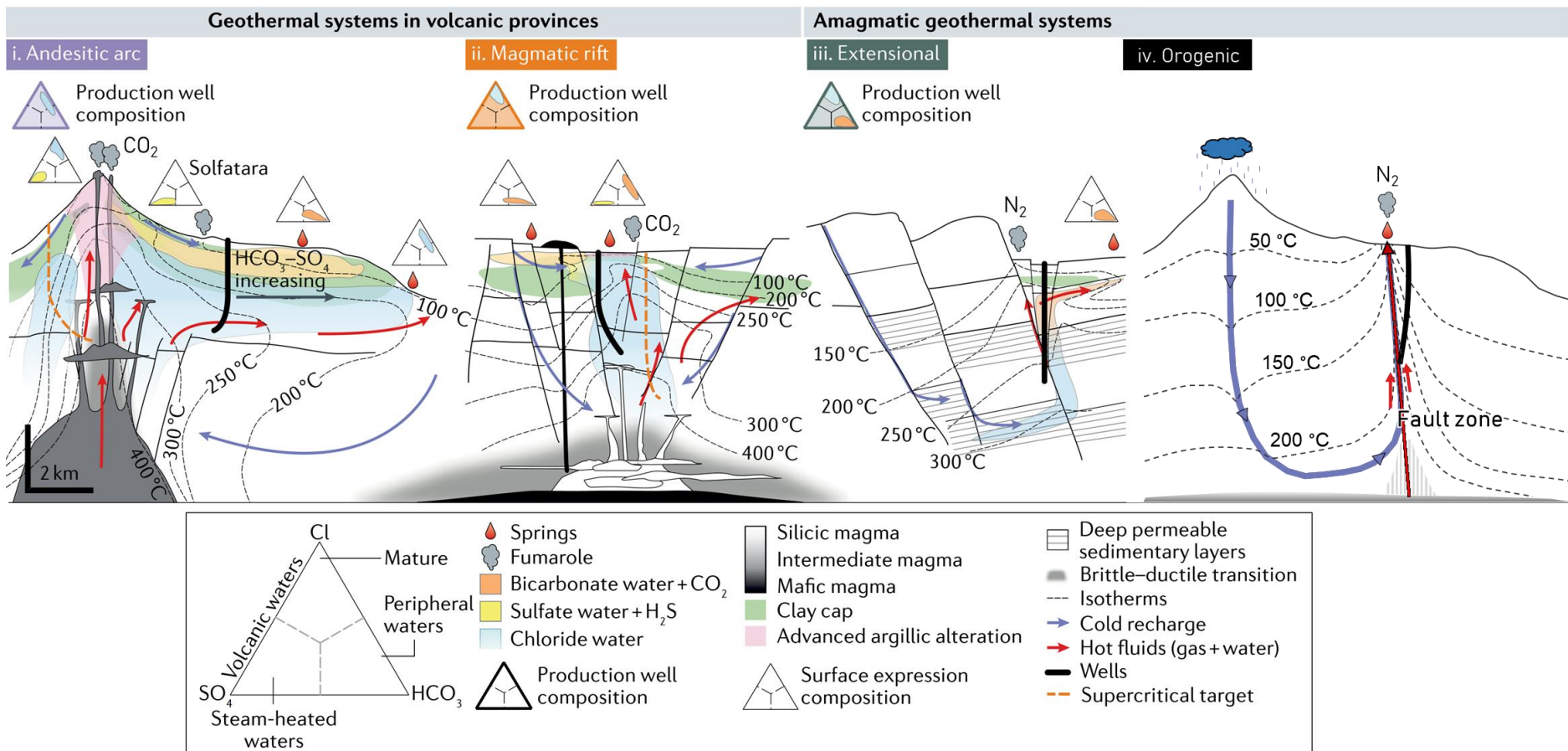


Figure 2.3. Conceptual models of magmatic and amagmatic geothermal systems. Specifically, in (i) volcanic arcs, (ii) mature magmatic rift environments, (iii) amagmatic extensional sedimentary environments (immature rifts), and (iv) amagmatic orogens with mountainous topography. Adapted from [Jolie et al. \(2021\)](#).

2.3. Hydraulic driving force

The movement of water in amagmatic orogenic geothermal systems is fundamentally driven by hydraulic head gradients. The hydraulic head gradients (∇P) indicate how the hydraulic head changes with respect to distance and allows the direction and rate of groundwater flow in a subsurface system to be determined. Hydraulic head (P) is a combination of pressure head (ψ) and elevation head (z) relative to a specific reference point or datum ($z = 0$) (Figure 2.4). It represents a measure of the total potential energy of water at a specific point within a groundwater system (Hubbert, 1940).

Regions with significant differences in topographic elevation are associated with variations in hydraulic heads. Water naturally moves from regions of higher hydraulic head to lower hydraulic head ($h_1 > h_2$; Figure 2.4) (Tóth, 2009). However, the water flux is also controlled by the permeability of the rocks. The relationship between water flux, hydraulic head gradients and permeability is described by Darcy's Law (Eq. 2.1) (Darcy, 1856):

$$\mathbf{u} = -\frac{k}{\mu}(\nabla P - \rho g) \quad (2.1)$$

In this equation u symbolizes the Darcy flux (m s^{-1}), which is the flux of the fluid through the porous medium (rock or unconsolidated sediment); k is the intrinsic permeability (m^2) of the medium, quantifying the ease of the medium to transmit fluids; μ is the dynamic viscosity of the fluid (Pa s), characterizing fluid resistance to flow; ∇P (Pa m^{-1}) is the hydraulic head gradient, ρ is the density of water (kg m^{-3}), and g is the acceleration due to gravity (m s^{-2}).

Darcy's Law encapsulates the fundamental principles of how fluids move within amagmatic orogenic geothermal systems, which are closely tied to mountainous regions. In these systems, changes in the elevation of the landscape drive the movement of water to deeper depths along interconnected fracture and fault zones. Elevated terrain is correlated with elevated hydraulic heads, whereas valley floors and coastal zones have lower hydraulic heads (Figure 2.4c).

Superimposed on the driving force of hydraulic head gradients is the buoyancy force resulting from spontaneous convection of fluid in the temperature field of the host fault. The relative strength of buoyancy typically depends on the local heat flow and rate of surface cooling (i.e., the steady-state background geothermal gradient) in competition with cooling or heating due to the fluid circulation (e.g., Alt-Epping et al., 2022).

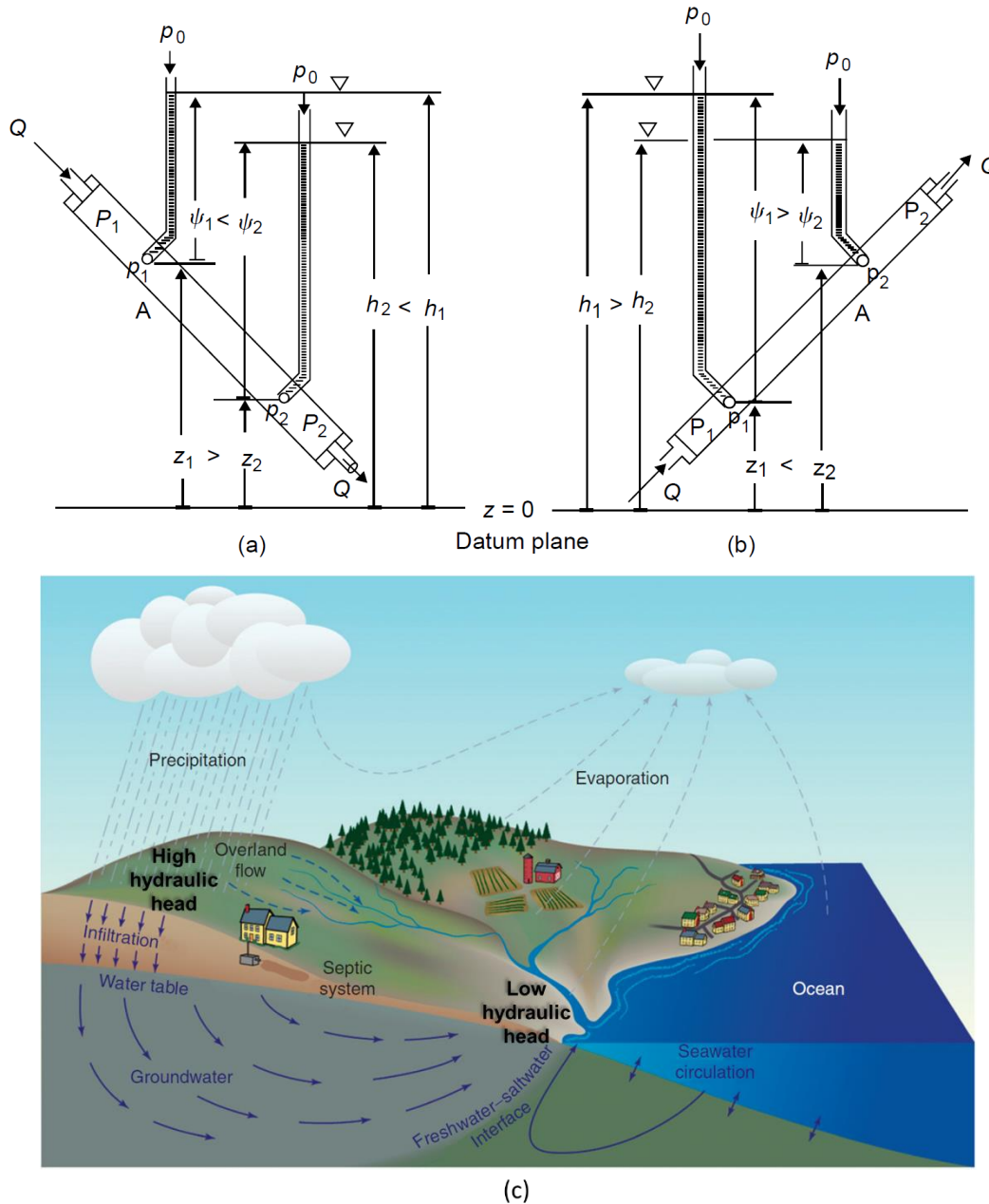


Figure 2.4. Effects of hydraulic head on water flow direction: (a) water movement from lower to higher pressure zones, (b) water flow from lower to higher elevation areas (Tóth, 2009). (c) Representation of groundwater flow from high topography (high hydraulic head) to valley floors or coastal areas (low hydraulic head), modified from (Mulligan & Charette, 2009).

2.4. Key hydraulic rock properties influencing fluid flow

In amagmatic orogenic geothermal systems, fluid usually circulates through crystalline rocks such as granites and gneisses. The way fluids move is influenced by important characteristics of

both the rocks and the fluids involved. These properties include permeability, fracture porosity, thermal conductivity and the specific heat capacity (the amount of heat the rock and water can hold). All of these properties determine how fluid is transported and how it thermally interacts with the host rock. Typical values for different host rocks are given in Table 2.1.

Permeability, denoted as k (m^2), can for instance be derived from hydraulic conductivity K (m s^{-1}) obtained from borehole hydraulic tests (Stober & Bucher, 2007). The relationship between permeability and hydraulic conductivity is defined by the equation:

$$k = K \frac{\mu}{g\rho} \quad (2.2)$$

Here μ represents the dynamic viscosity of the fluid ($\text{kg m}^{-1} \text{s}^{-1}$), g is the acceleration due to gravity (m s^{-2}), and ρ is the density of water (kg m^{-3}). Crystalline rocks generally exhibit permeability values within a low range of 10^{-18} – 10^{-16} m^2 (Evans et al., 1997; Stober & Bucher, 2007).

Porosity, represented as φ (%), is defined as the ratio of volume of the fluid-saturated pore space to the bulk volume of the rock, typically expressed as a percentage (Table 2.1). In the amagmatic orogenic geothermal systems, the effective advective flow may occur in both rock-matrix and fracture porosity (Stober & Bucher, 2007). However, in crystalline rocks, the contribution of matrix porosity to fluid flow is limited. Fracture porosity, created by a network of fractures with apertures typically ranging from 1 to 3 mm (Stober & Bucher, 2007), governs the amount of mobile water present in crystalline rocks.

The thermal behavior of rocks, such as their role as heat conductors or insulators, is defined by their thermal conductivity and heat capacity values. Thermal conductivity (λ) measures the ability of a material to conduct thermal energy. In contrast, specific heat capacity (Cp) quantifies the amount of heat energy required to raise the temperature of a given mass of the material by one degree Celsius at a constant pressure (Bergman, 2011).

In amagmatic orogenic geothermal systems, characterized by the absence of magmatic heat sources and by low conductive heat flow, the process of advection becomes crucial for efficiently moving a significant amount of heat. This is because the high specific heat capacity of water (Table 2.1) allows it to effectively absorb or deposit significant amounts of heat if its temperature is above that of its wall rocks.

Table 2.1

Permeability (k), porosity (ϕ), thermal conductivity (λ) and specific heat capacity (Cp) ranges of values of selected rocks and water (Emerson, 1990; Bergman, 2011; Bear, 2013; Siegfried & Helmut, 2004).

Rock	k (m ²)	ϕ (%)	λ (W m ⁻¹ K ⁻¹)	Cp (J K ⁻¹ g ⁻¹)
Granite	10 ⁻¹⁶ –10 ⁻¹⁸	0.1–2.3	1.3–4.0	0.8
Limestone	10 ⁻¹⁵ –10 ⁻¹⁶	2–35	0.8–1.5	0.8
Sandstone	10 ⁻¹³ –10 ⁻¹⁴	5–25	0.7–1.7	0.8–0.9
Basalt	10 ⁻¹⁴ –10 ⁻¹⁵	2–20	0.5–2.0	0.8–0.9
Shale	10 ⁻¹⁷ –10 ⁻²⁰	10–40	1.0–1.5	1.4
Water			0.6	4.18

2.5. Fault zone architecture

In orogenic amagmatic geothermal systems, water flow occurs along interconnected fracture networks and faults. Fractures are essentially cracks or fissures in rocks usually caused by tectonic, thermal or unloading (exhumation) stresses. A fault is a surface where rock masses have moved relative to each other in response to a shear stress (Van der Pluijm & Marshak, 2004). In contrast, fracture sets termed joints may show no shear offset. Fracture networks are particularly common around major orogenic faults under periodic ruptures, where the interplay between permeability and fluid dynamics are linked to the seismic cycle (Sibson, 1994).

The fault zone architecture comprises distinct components, such as fault cores and damage zones, surrounded by the host rock formation (wall rock). These components play a critical role in determining fluid flow patterns (Faulkner et al., 2010). Fault cores consist of single slip surfaces, clay-rich gouge zones, brecciated and altered areas, or cataclasite zones at the centimeter scale. In contrast, at the meter scale, the flanking damage zones may encompass subsidiary features like faults, veins, fractures, and even cleavage and folds if the fault is in the ductile regime (Caine et al., 1996).

Fault zones can exhibit a single fault core, possibly accompanied by interconnected subsidiary faults (Figure 2.5a). Alternatively, the fault core may branch and interconnect, incorporating damaged rock lenses (Figure 2.5b; Mitchell & Faulkner, 2009). These characteristics give rise to distinct hydraulic zones within the fault zone. If the fault core contains fine-grained gouge (crushed rock, often clay-rich), then it may act as a low-permeability

boundary for fluid migration, whereas the surrounding damage zone exhibits high permeability (Yehya & Rice, 2020). Typical values for damage zones range from 10^{-16} to 10^{-14} m². In contrast, the permeability of the core ranges from 10^{-20} to 10^{-17} m² (Evans et al., 1997). Alterations in the architecture of fault zones can lead to significant modifications in permeability structure, subsequently affecting the patterns of fluid flow (Caine & Forster, 1999).

Most geothermal systems with intermediate-temperature to high-temperature (≥ 125 °C to ≥ 225 °C) are usually found along normal and strike-slip fault zones, often within complex zone of interactions. These zones include fault terminations, step-overs, intersections, accommodation zones, displacement transfer zones, and pull-aparts. In these areas, there is a notable increase in porosity and concentration of fractures and hence enhanced permeability, facilitating sustained fluid flow over time (Figure 2.6) (Jolie et al., 2021).

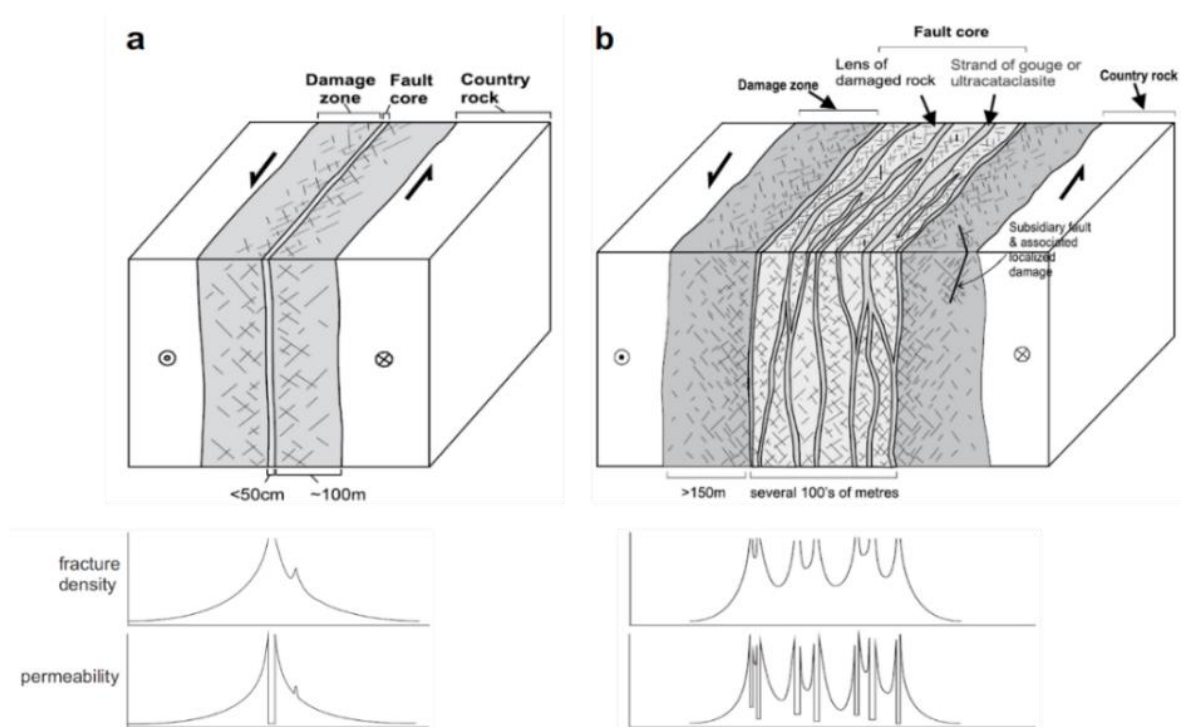


Figure 2.5. Fault architecture, (a) single fault core, (b) multiple fault cores, adapted from (Faulkner et al., 2010) and (Mitchell & Faulkner, 2009).

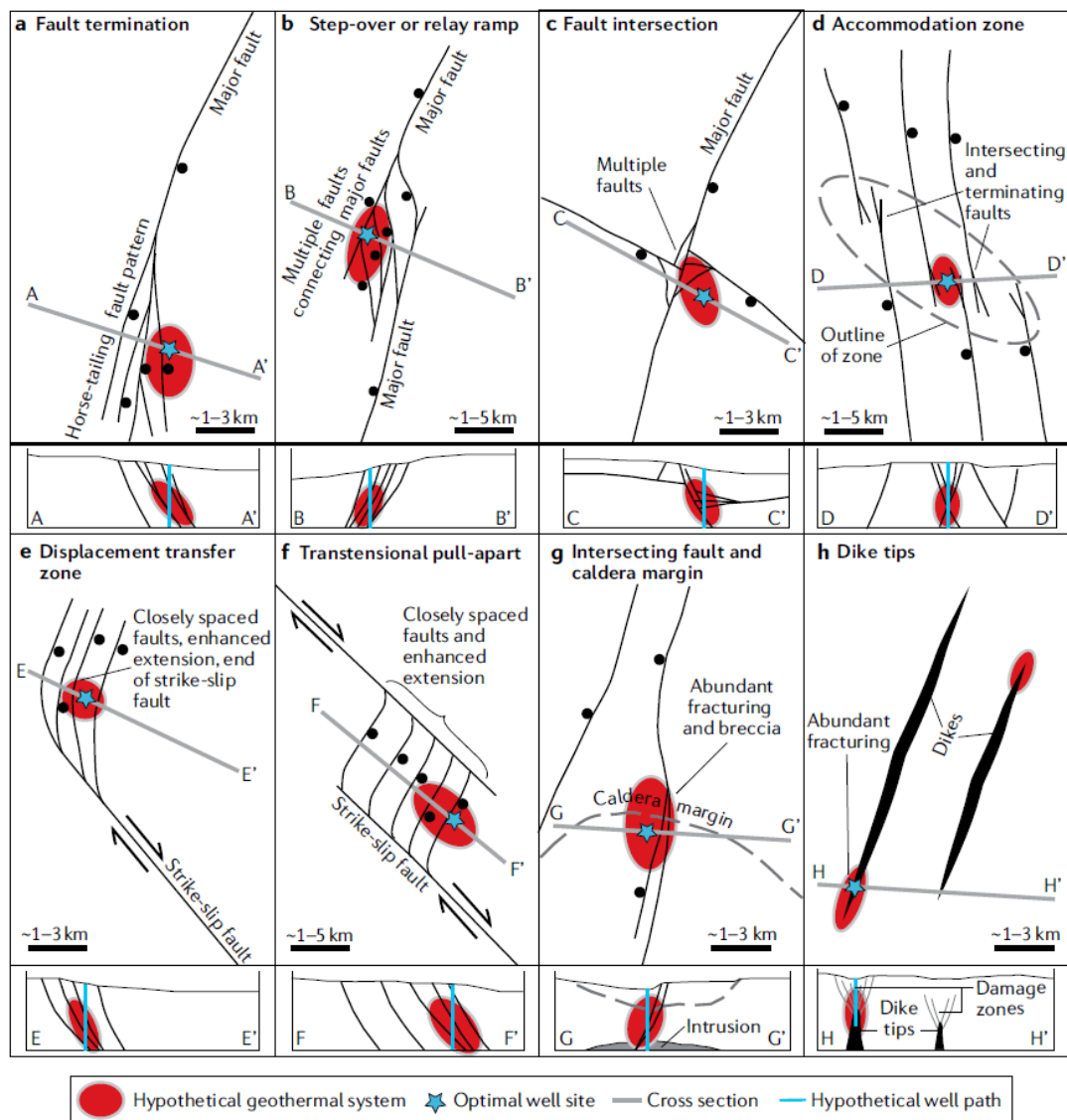


Figure 2.6. Ideal structural settings for geothermal exploration and exploitation from [Jolie et al. \(2021\)](#).

2.6. Thermal–hydraulic numerical simulations

Numerical simulations such as those coupling thermal, hydraulic, mechanical, and chemical processes are a powerful tool to quantitatively study geothermal systems. The coupling of these processes is numerically captured by governing equations and constitutive laws, encompassing the conservation of fluid mass (Darcy’s Law), energy (e.g. heat), solute mass, and solid mass (Figure 2.7; [Steeffel et al., 2005](#)). Such coupling between thermal and hydraulic processes is crucial because properties like density and viscosity, which influence fluid flow (Eq. 2.1 and 2.2), are highly dependent on temperature.

To carry out the thermal–hydraulic (TH) numerical simulations, the software TOUGHREACT (Pruess et al., 1999) was employed by switching off chemical reactions between the different fluids involved and the host rock through which fluid flow occurs. Nevertheless, chemical and isotopic compositions of thermal waters were used to develop conceptual model of the studied geothermal systems and thus to constrain the corresponding TH simulations. The following steps describe the iterative modeling workflow applied throughout this thesis: (1) Development of a conceptual model based on geological, geochemical and geophysical data, (2) generation and numerical discretization of a three-dimensional geological model, (3) definition of initial and boundary conditions, (4) model calibration, (5) model verification and validation by comparing modeling results with geological, geochemical, and geochemical observations and (6) updating of the conceptual model and redoing steps (2) to (5).

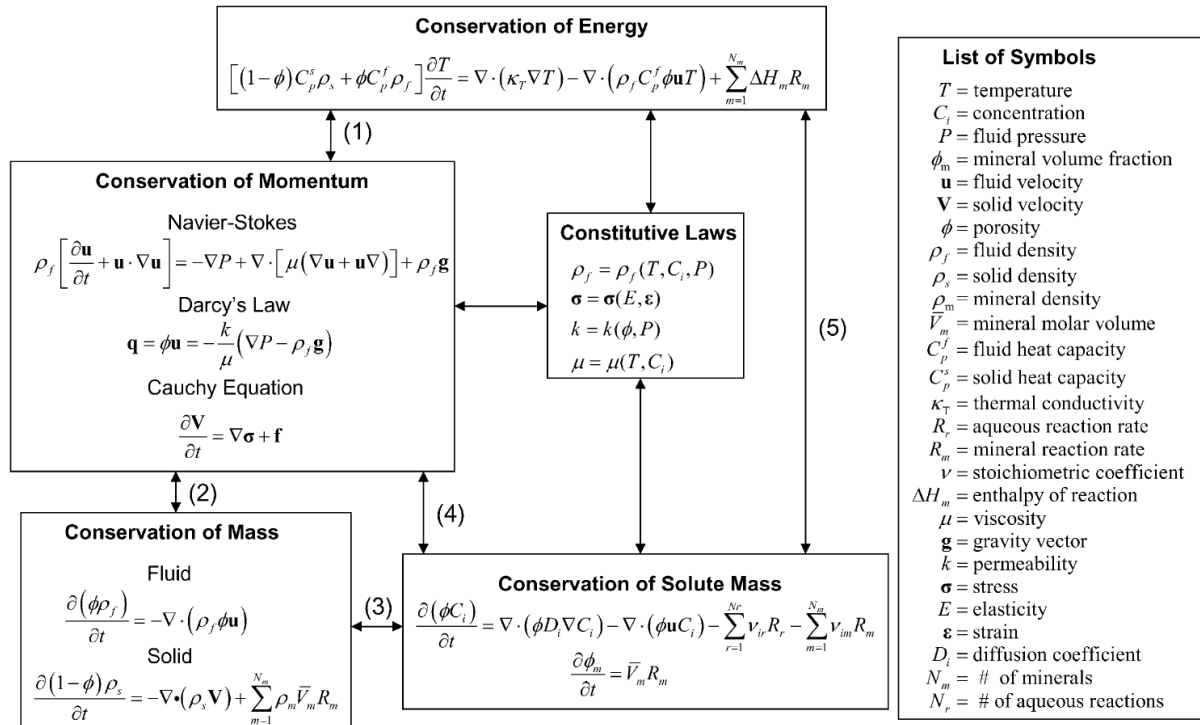


Figure 2.7. Governing conservation equations and constitutive laws for a coupled reactive transport system involving a single fluid phase, taken from Steefel et al. (2005).

TOUGHREACT employs a continuum model, which is a mathematical and physical framework based on the principle of mass and energy conservation to express the laws of physics (Steefel & Maher, 2009). The principle of the mass conservation equation captures the inflow, outflow, internal generation, and consumption of substances (Figure 2.7) (Lichtner, 1996) and is

represented mathematically as:

$$\textit{Accumulation} = \textit{Inflow} - \textit{Outflow} + \textit{Sources} - \textit{Sinks} \quad (2.3)$$

where *Accumulation* quantifies any increase or decrease of mass and/or energy within the chosen control volume. *Inflow* accounts for the mass or energy entering the control volume from its boundaries, while *Outflow* represents the mass and/or energy exiting the control volume into the surrounding environment. *Sources* are additional contributions of mass and/or energy originating within the control volume, while *Sinks* are processes occurring within the control volume that either remove or consume the mass and/or energy.

The conservation equations are typically formulated as partial differential equations (PDEs) (Figure 2.7), describing how system parameters change across space and time. To solve the PDEs numerically, the model domain needs to be discretized into a series of representative elementary volumes (REV) (Lichtner, 1996). Over each REV, system properties such as pressure, temperature, porosity, and permeability are averaged. Their size thus depends on the degree of heterogeneity or spatial resolution required in the specific model. The system properties within REVs change over time intervals based on the initial and boundary condition assigned. This method is called integral finite difference and there are various approaches to numerically define derivatives with respect to time and space such as forward, backward, and central differences (Lichtner, 1996; Sullivan & Sullivan, 2016). In addition to the definition of an REV, initial and boundary conditions need to be specified to numerically solve the PDEs. Initial conditions are the parameter values that define the spatial differentials at the beginning of the simulation. In contrast, boundary conditions define the spatial differentials at the edges and in the whole model. There are two main types of boundary conditions. The first is termed a Dirichlet condition, which specifies the exact values of a quantity at the boundaries (e.g., temperature). The second is a Neumann condition, which specifies the rate of change of the relevant variables at those boundaries (e.g., heat flux) (Pruess & Narismhan, 1985; Steefel & Maher, 2009; Seigneur et al., 2019).

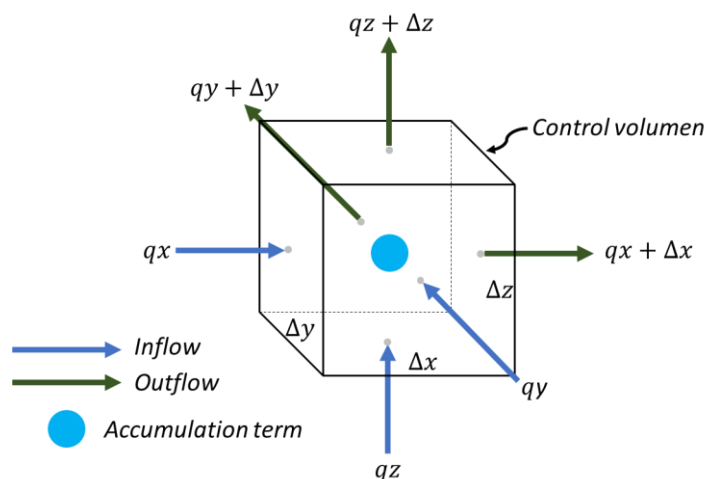


Figure 2.7. Control volume to represent the mass conservation principle, adapted from (Steefel & Maher, 2009).

2.6.1. Water and heat flux equations

To understand how TOUGHREACT conducts TH simulations, this section presents the fundamental equations the code uses to model the transport of water and heat. The equation describing the change in fluid mass (Δm_w) accumulation over time is:

$$\Delta m_w = \Delta(\rho_w \varphi) \quad (2.4)$$

This equation indicates that the change in fluid mass (Δm_w) is proportional to the change in water density (ρ_w) multiplied by the porosity (φ) over time within the control volume (Steefel et al., 2005).

The inflow and outflow terms capture the movement of fluid mass across the boundaries of the control volume:

$$Inflow = \frac{A\Delta t\rho_w q(x) + A\Delta t\rho_w q(y) + A\Delta t\rho_w q(z)}{V} \quad (2.5)$$

$$Outflow = \frac{A\Delta t\rho_w q(x + \Delta x) + A\Delta t\rho_w q(y + \Delta y) + A\Delta t\rho_w q(z + \Delta z)}{V} \quad (2.6)$$

Equation (2.5), calculates the inflow of fluid mass into the control volume, summing contributions from different directions. The terms $q(x)$, $q(y)$, and $q(z)$ ($\text{m}^3 \text{ water m}^{-2} \text{ s}^{-1}$) represent the volumetric flow rates across the area (A) perpendicular to each spatial axis (x , y , z). The term $A\Delta t\rho_w$ reflects the volume of fluid entering the control volume within the time interval (Δt), where ρ_w denotes the density of the fluid (kg m^{-3}). Dividing by the total volume V gives the inflow rate per unit volume. Similarly, Equation (2.6) represents the concept of outflow from the control volume.

Equations (2.7) and (2.8) express changes in fluid mass content within the control volume (sources and sinks), accounting for differences between inflows and outflows across boundaries. They provide a discrete representation of flux divergence across adjacent boundaries.

$$\Delta(\rho_w \varphi) = \Delta t \rho_w \left[\frac{q(x)}{\Delta x} + \frac{q(y)}{\Delta y} + \frac{q(z)}{\Delta z} \right] - \Delta t \rho_w \left[\frac{q(x + \Delta x)}{\Delta x} + \frac{q(y + \Delta y)}{\Delta y} + \frac{q(z + \Delta z)}{\Delta z} \right] \quad (2.7)$$

$$\frac{\Delta(\rho_w \varphi)}{\Delta t \rho_w} = \left[\frac{q(x) - q(x + \Delta x)}{\Delta x} + \frac{q(y) - q(y + \Delta y)}{\Delta y} + \frac{q(z) - q(z + \Delta z)}{\Delta z} \right] \quad (2.8)$$

Considering an infinitesimally small control volume ($\Delta x, \Delta y, \Delta z \rightarrow 0$), the change in water mass per volume (or water content) is equivalent to the negative sum of derivatives (or negative divergence) of fluxes, including sources and sinks ($\pm S$). This fluid mass conservation equation can be expressed as:

$$\frac{1}{\rho_w} \frac{\partial(\rho_w \varphi)}{\partial t} = -\frac{\partial q_x}{\partial x} - \frac{\partial q_y}{\partial y} - \frac{\partial q_z}{\partial z} \pm S \quad (2.9)$$

Equation (2.10) establishes the link between the balance mass conservation equation and the water flux equation, which is represented by Darcy's Law (Eq. 2.1) together with the consideration of sources and sinks ($\pm S$). Equation 2.10 shows only the divergence flux in x direction.

$$\frac{1}{\rho_w} \frac{\partial(\rho_w \varphi)}{\partial t} = -\frac{\partial q_x}{\partial x} \pm S = \frac{\partial}{\partial x} \left[-\frac{k}{\mu} \frac{\partial(\nabla P - \rho g)}{\partial x} \right] \pm S \quad (2.10)$$

Equation 2.11 shows the conservation of fluid mass, where \mathbf{q} is the Darcy velocity (m s^{-1}).

$$\Delta m_w = \frac{\partial(\rho_w \varphi)}{\partial t} = -\nabla(\rho_w \mathbf{q}) \pm S \quad (2.11)$$

The continuum approach extends to the balance of heat content (ΔH) over time within the control volume influenced by the divergence of heat fluxes across different directions (x, y, z) (Xu et al., 1999b), expressed as follows:

$$\Delta H = \frac{\partial(c_m \rho_b T)}{\partial t} = -\frac{\partial j_{hx}}{\partial x} - \frac{\partial j_{hy}}{\partial y} - \frac{\partial j_{hz}}{\partial z} \pm S \quad (2.12)$$

In this equation, ΔH represents the change in heat content (J m^{-3}), c_m is the specific heat capacity ($\text{J K}^{-1} \text{m}^{-3}$) per bulk volume (ρ_b), T represents the temperature (K).

Heat fluxes (j_h) in equation (2.12) are describe through conductive and convective heat fluxes as follows:

$$\frac{\partial(c_v T)}{\partial t} = -\frac{\partial j_h x}{\partial x} \pm S = \frac{\partial}{\partial x} \left[\lambda \frac{\partial T}{\partial x} - \mathbf{q} x c_w T \right] \pm S \quad (2.13)$$

In this equation, the volumetric bulk heat capacity ($\text{J K}^{-1} \text{m}^{-3}$) is represented as $c_v = \frac{\rho_b}{c_m}$, the term λ represents the heat conductivity ($\text{W m}^{-1} \text{K}^{-1}$), indicating the efficiency of a material to conduct heat. The $\frac{\partial T}{\partial x}$ term represents the temperature gradients, while the product $\mathbf{q} x c_w T$ accounts for the convective heat flux attributed to Darcy velocity ($\mathbf{q} x$) in the divergence flux in x direction, where c_w is the volumetric heat capacity of water ($\text{J K}^{-1} \text{m}^{-3}$).

Equation 2.14 shows the conservation of energy:

$$\Delta H = \frac{\partial(c_v T)}{\partial t} = -\nabla(\lambda \nabla T - \mathbf{q} c_w T) \pm S \quad (2.14)$$

Equations (2.11) and (2.14) show how hydraulic (fluid) and thermal (heat) processes are coupled. This means that the amount of heat moving through an REV depends on fluid flow (\mathbf{q} in Eq. 2.14). At the same time, the properties of fluid flow such as density and viscosity are temperature-dependent. It is important to note that the water velocity and the heat flux transferred within an REV in a specific time, are affected by the permeability, porosity and hydraulic pressure and the bulk volumetric heat capacity.

Part 2: Research papers

3. Behavior of amagmatic orogenic geothermal systems: insights from the Agua Blanca Fault, Baja California, Mexico

Daniel Carbajal-Martínez^{1,*}, Christoph Wanner¹, Larryn W. Diamond¹, Loïc Peiffer^{2,3}, John M. Fletcher², Claudio Inguaggiato² and Manuel Contreras-López⁴

¹ Rock–Water Interaction Group, Institute of Geological Sciences, University of Bern, Switzerland

² Departamento de Geología, Centro de Investigación Científica y de Educación Superior de Ensenada (CICESE), Ensenada, Baja California, México.

³ Unidad La Paz (ULP), Centro de Investigación Científica y Educación Superior de Ensenada (CICESE), La Paz, Baja California Sur, México.

⁴ Laboratorio Universitario de Geoquímica Isotópica (LUGIS), Instituto de Geofísica, Universidad Nacional Autónoma de México (UNAM), Ciudad de México, México

Submitted to *Geochemistry, Geophysics, Geosystems*, July 2023.

Abstract

Amagmatic geothermal systems within regional-scale orogenic faults are promising renewable resources for heat and possibly electricity production. However, their behavior needs to be better understood to improve exploration and assessment of their energy potential. To provide more insight, we report geochemical, geological, and geophysical studies from seven hot spring sites strung along a 90 km segment of the Agua Blanca Fault (ABF), which traverses a mountainous region of northern Baja California, Mexico. Our results show that topographic heads drive infiltration of meteoric water deep into basement rocks, where it is heated according to the local geothermal gradient. Our diverse dataset provides strong evidence that the flow system, magnitude, and location of the thermal anomalies are primarily controlled by the permeability of the ABF system and the hydraulic head gradients. The hot water ascends along preferentially permeable zones, discharging at temperatures from 37 °C in inland springs to 102 °C on the Pacific coast. Higher temperatures correlate positively with the degree of extensional fault displacement (a proxy for fault permeability). Correlations between hydraulic head gradients, residence times, and $^3\text{He}/\text{He}_{\text{total}}$ of the thermal waters show that the hydraulic head gradient controls the length and depth of the flow paths. Long paths to great depths lead to long water

residence times and high $^3\text{He}/\text{He}_{\text{total}}$ fractions. Optimal conditions at the coast allow the 120 °C temperature threshold for electricity production to be reached at relatively shallow depths (<2 km), demonstrating the potential of orogenic geothermal systems for petrothermal exploitation.

Plain Language Summary

The deep circulation of meteoric water in areas not affected by volcanic heat represents underexplored renewable energy sources for heat or electricity production. A challenge for exploration is that the processes and forces that drive hot water circulation in such systems are not fully understood. To obtain new insights, we undertook a geochemical, geological, and geophysical study of seven hot spring sites strung along a 90 km long fault zone across the northern Baja California Peninsula in Mexico. Our data show that rainwater infiltrates deep into mountainous areas and modifies its chemical composition and temperature, in the absence of any magmatic heat source. We also discovered that the local permeability of the fault zones controls the discharge temperature of the hot springs and, thus, the amount of thermal energy that could be potentially exploited from such systems. Other relevant system parameters, such as the depth of water infiltration and the subsurface water residence time, are controlled by the differences in water pressure under high and low points in the topography and by the distance between the point of infiltration of rainwater and its subsequent discharge location.

3.1. Introduction

Regional-scale faults in mountainous orogens often host hot springs with potential as geothermal resources, even in areas where magmatic heat is absent and heat fluxes are moderate (Wanner et al., 2019). The springs are the discharge sites of meteoric water that has infiltrated at high altitudes, circulated deep into the fault plane where it has acquired heat from the wall rocks and then ascended through preferentially permeable upflow zones to low points in the topography (e.g., López & Smith, 1995; Menzies et al., 2016; Alt-Epping et al., 2022; Stober et al., 2022). Meteoric water circulation through the purely brittle realm of the host fault is driven by high hydraulic heads induced by the rugged topography and elevated fault permeabilities. Penetration depths of meteoric water are deduced to be as high as 9–10 km (Diamond et al., 2018), and in some cases meteoric water may penetrate the transiently ductile deformation realm (for which additional driving forces are required; McCaig, 1988; Upton et al., 1995; Menzies et al., 2014).

Worldwide occurrences of such amagmatic orogenic geothermal systems include those in the Canadian Rocky Mountains ([Grasby & Hutcheon, 2001](#)), Lérida province in the Pyrenees in Spain ([Asta et al., 2010](#)), Da Qaidam in China ([Stober et al., 2016](#)), Brigerbad in Switzerland ([Sonney & Vuataz, 2008](#)), the Eastern Pyrenees in France ([Taillefer et al., 2018](#)), Huangshadong in China ([Tian et al., 2023](#)), along the Alpine Fault in New Zealand ([Sutherland et al., 2017](#); [Coussens et al., 2018](#)), along the Lishan Fault in Taiwan ([Chen, 1985](#); [Upton et al., 2011](#)) and the Nepalese Himalaya ([Whipp & Ehlers, 2007](#)). These fault-hosted, topography-driven systems are characterized by regional crustal geothermal gradients typically between 20 and 30 °C km⁻¹ (with exceptionally higher gradients in the Alpine Fault, New Zealand; [Sutherland et al., 2017](#)), by temperatures of 100 to at least 250 °C at the greatest depths of water circulation, and by spring temperatures of 25–102 °C.

Prolonged heat extraction from the wall rocks by water moving along the base of the circulation loop and its redeposition into the wall rocks of the upflow path can create large, three-dimensional, plume-like thermal anomalies beneath the discharge sites ([Wanner et al., 2019](#)). At depths within the reach of drilling (e.g., 2 km), the temperatures in these plumes can exceed the 120 °C threshold for electricity generation. Thus, although discharge rates are normally modest, the plumes of hot rock below the springs can be viewed as targets for petrothermal exploitation, presumably requiring artificial hydraulic stimulation to facilitate heat extraction ([Wanner et al., 2019](#)).

To improve exploration strategies for this geothermal play, a better understanding is required of how they behave, particularly the controls on their locations and magnitudes. We have therefore undertaken a geochemical, geophysical, and geological study of orogenic geothermal systems along the Agua Blanca Fault (ABF) in Ensenada, NW Baja California, Mexico. We chose this topographically rugged area because it exhibits three favorable features: (1) seven geothermal systems are strung out along a ~90 km stretch of the fault, permitting quantitative correlation of hydraulic head gradients with the physicochemical properties of the springs; (2) water discharge temperatures vary along the fault from 37 to 102 °C, the latter being worldwide the hottest and therefore most prospective amagmatic system to our knowledge; (3) the host fault is active and the rates and magnitudes of tectonic extension along its segments have been quantified ([Wetmore et al., 2019](#); [Gold et al., 2020](#)), allowing qualitative assessment of permeability variations along the fault.

In this paper, we take advantage of these features to explore how the interplay of variable

fault permeability and hydraulic head gradients control the location and discharge temperatures of the springs. To enable this treatment, we present new analyses of spring compositions, including major solutes, pH, temperature, dissolved gases, O–H stable isotopes, and He–Ne radiogenic isotopes. We calculate water residence times and reservoir temperatures and interpret earthquake hypocenters to estimate depths to the brittle–ductile transition zone (BDTZ) and geothermal gradients. Finally, we identify recharge zones from O–H stable isotopes and topographic maps, calculate hydraulic head gradients, and integrate our collective results with structural data from the literature. As well as providing new insight into the hydraulic controls on the geothermal systems, our new data and correlations will serve as calibration targets for future 3D numerical simulations of water circulation through the ABF, from which additional parameters can be quantified and conclusions drawn for exploration strategies.

3.1.1. Geology and geothermal manifestations of the study area

The study area is located in the northwest of the Baja California Peninsula, Mexico (Figure 3.1a) and encompasses the northwestern sector of the geological province known as the Peninsular Ranges Batholith. The rocks in this province (Figure 3.1b) can be divided into three tectonostratigraphic groups (Gastil et al., 1975): (i) Pre-batholithic rocks, consisting of a Triassic–Jurassic belt of metamorphosed quartz-bearing sandstone, argillite, and minor carbonate rocks located in the eastern part of the study area. Part of the same group is the Alisitos Formation, an Aptian–Albian belt of volcanic (andesite to dacite) and volcanoclastic (tuff and pyroclastic) rocks interbedded with sedimentary mudstone, sandstone, and limestone along the western flank of Baja California; (ii) Batholithic rocks of Cretaceous age dominated by tonalite (73 vol.%), granodiorite (23 vol.%), with minor gabbro and diorite (2 vol.%), and quartz monzonite (2 vol.%). These underlie the entire study area, having been emplaced successively from west to east between 140 and 80 Ma (Gastil, 1975; Ortega-Rivera, 2003); (iii) Post-batholithic rocks comprising the Late Cretaceous Rosario Group of marine mudstones, sandstones and granitic conglomerates; Eocene–Paleocene marine mudstones and sandstones; and Miocene volcanic rocks (rhyolite, andesite, and basalt).

The study area is recognized as an active tectonic zone encompassing three steeply dipping dextral fault systems: Agua Blanca Fault (ABF), Tres Hermanos Fault (THF), and San Miguel-Vallecitos Fault (SMVF) (Figure 3.1b). These collectively host a total of seventeen geothermal systems, manifested by hot springs, submarine fumaroles, domestic thermal wells,

and coastal thermal anomalies (Figure 3.1b, c). Chemical and isotopic analyses of water and gas discharges from some of these geothermal systems have confirmed their meteoric origin and have revealed no evidence of a magmatic heat source. This observation aligns with the absence of post-Miocene magmatic rocks in the area (Vidal et al., 1981; Gastil & Bertine, 1986; Polyak et al., 1991; Beltrán-Abaunza & Quintanilla-Montoya, 2001; Arango-Galván et al., 2011; Barry et al., 2020).

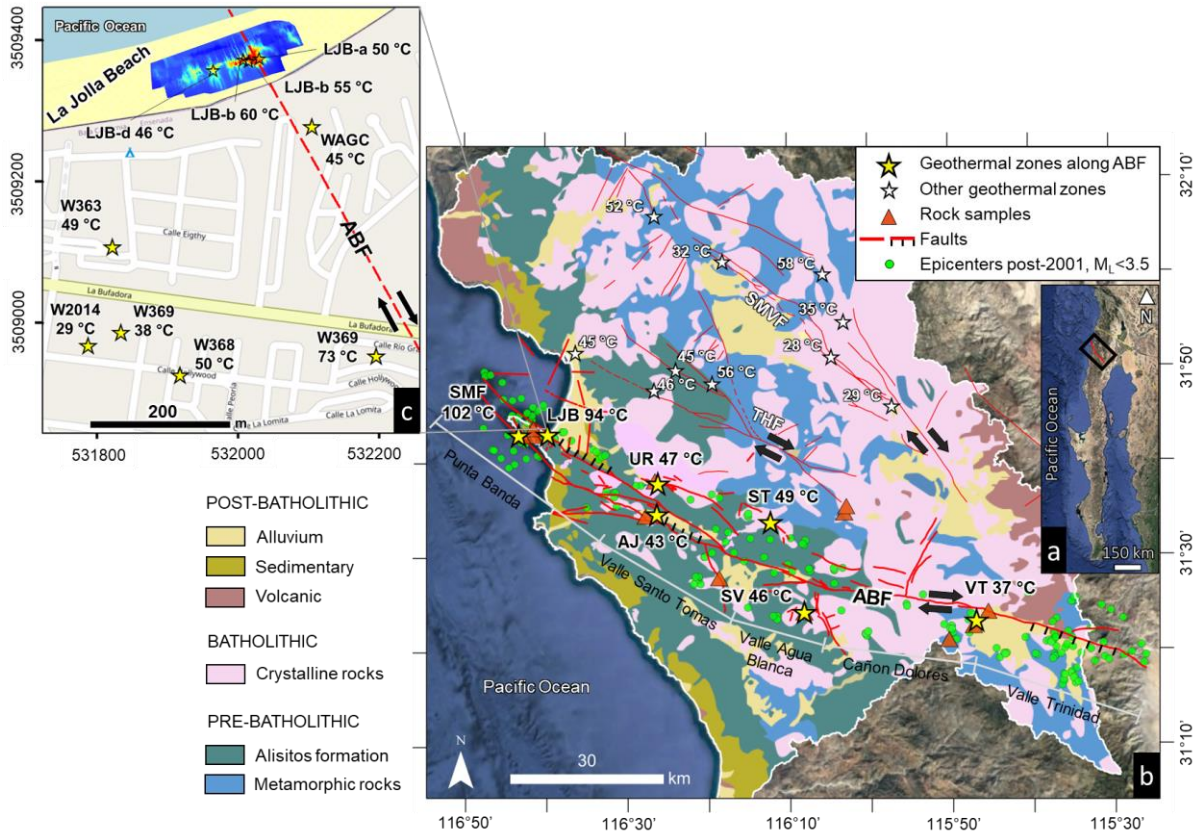


Figure 3.1. Location of the study area and its geological and geothermal features. a) Location in Baja California, Mexico, highlighted by a black rectangle. b) Geological map modified from Gastil et al. (1975) with locations of seventeen orogenic amagmatic geothermal systems (stars) along fault traces (red lines). Yellow stars mark the thermal waters reported in this study, divided into five geographic zones (labelled Punta Banda in the northwest to Valle Trinidad in the southeast) to facilitate discussion. c) Detailed location of La Jolla Beach thermal anomaly (Carbajal-Martínez et al., 2020) and its surrounding domestic thermal wells (UTM 11N coordinates).

The present study focuses on amagmatic geothermal systems occurring along the active ABF (Figure 3.2a). This subvertical, west–northwest-trending (276–302°) dextral–normal fault first became active between 3.3 and 1.5 Ma (Wetmore et al., 2019). It is transtensional along its ~150 km exposed length (downthrown to the north in the NW and to the south in the SE) and traverses nearly the entire Baja California Peninsula, extending beneath the Pacific Ocean in the northwest (Figure 3.2a). The ABF has several branches, recognizable from geomorphological features such as triangular facets, deviated streams, vegetation lines, and uplifted marine terraces (Allen et al., 1960; Rockwell et al., 1989). Although seismic events with magnitudes up to 3 are relatively infrequent compared to San Miguel-Vallecitos Fault (Figure 3.1b), earthquakes with magnitudes of 6–7 occur at a recurring interval of 75–200 years in the central zone of the ABF (Ortega-Rivera et al., 2018).

Thermal waters discharge in five valleys intersected by faults belonging to the ABF system. From southeast to northwest, these are Valle Trinidad, Cañon Dolores, Valle Agua Blanca, Valle Santo Tomas, and the coastal plains flanking the Punta Banda Peninsula (Figure 3.2b). Geologic and geodetic studies in these valleys indicate consistent slip rates of 2–4 mm year⁻¹ over ~10 kyr time scales (Wetmore et al., 2019; Gold et al., 2020). However, these valleys exhibit diverse extends of strike-slip along different sections. In Valle Trinidad, Cañon Dolores, and Valle Agua Blanca, the fault exhibits maximum strike-slip of up to 10–12 km. Conversely, the northwest section, comprising Valle Santo Tomas and Punta Banda, shows only 5–7 km of strike-slip. It is important to note that this section has undergone higher total dip-slip displacement (north side down) with values of 1.16 km and 1.25 km, respectively (Wetmore et al., 2019). Geodetic block modelling, along with previous geological assessments of slip direction, has revealed an increased occurrence of fault-perpendicular extension towards the southeast (3–10%) and northwest (5–15%), with lower values observed throughout the central part of the fault (<2%) (Wetmore et al., 2019). Notably, the area with the highest extension of the ABF coincides with the location of the hottest thermal waters along the coast of the Punta Banda Peninsula, specifically at La Jolla beach (LJB, 93 °C) and at a submarine fumarole (SMF, 102 °C) (Vidal et al., 1981; Carbajal-Martínez et al., 2020).

The study area is characterized by rugged topography (Figure 3.2a), which provides the potential energy to drive meteoric water deep into the ABF (Tóth, 1962, 2009). The main trace of the ABF intersects both ridges and valleys, reaching a maximum elevation of 1100 m a.s.l. (Figure 3.2b). Figure 3.2b also shows two topographic profiles parallel to the main trace of the

ABF, one offset by 1.5 km to the north, the other to the south. These indicate that the elevated northern side of the fault (up to ~1600 m a.s.l.) serves as the main recharge catchment for water infiltrating the ABF. The only exception is at the Punta Banda Peninsula, where elevations are higher on the southern side of the ABF (up to ~1000 m a.s.l.).

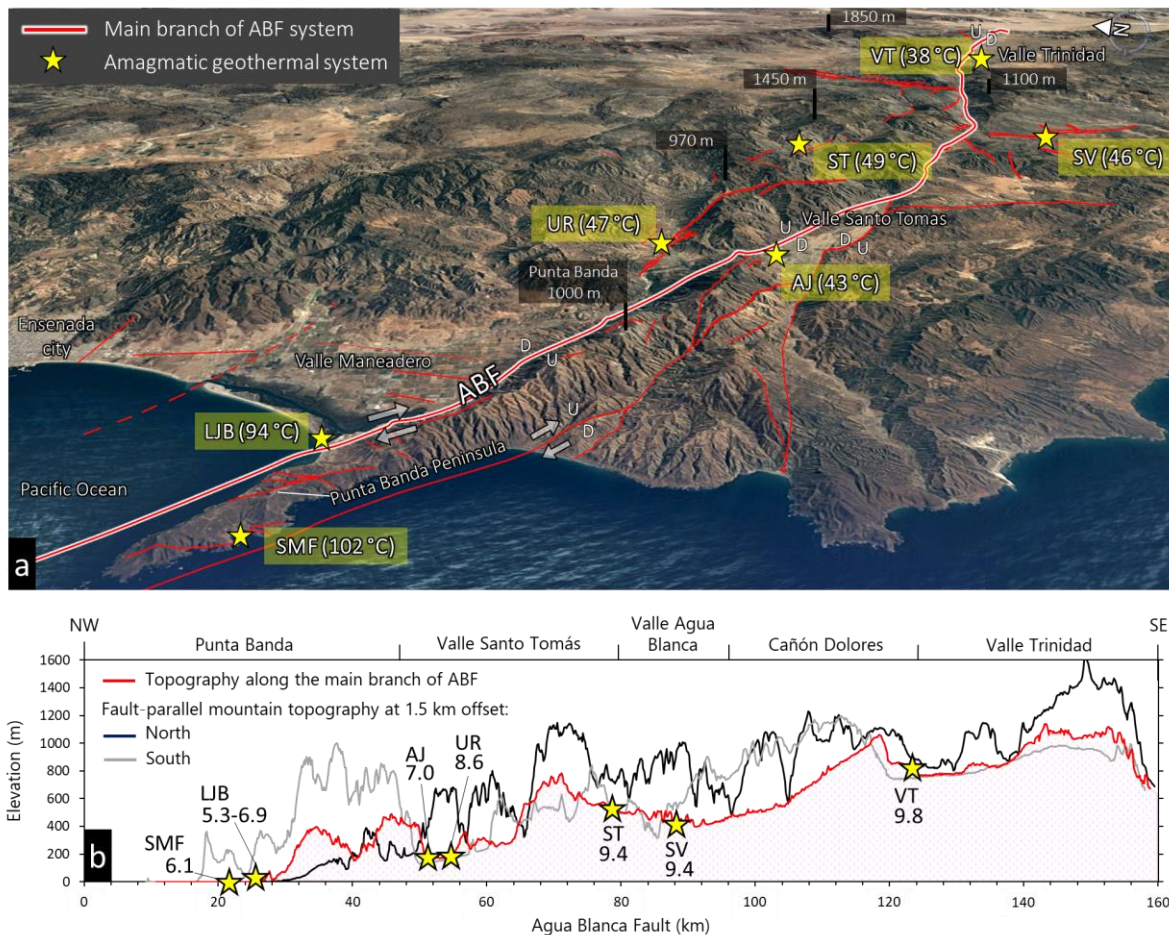


Figure 3.2. Oblique aerial view and topographic profile of the study area. a) 3D view highlighting the rugged topography, the location of amagmatic geothermal systems linked to the dextral Agua Blanca Fault (ABF), and the discharge temperatures of thermal springs. As indications of scale, the distance between the two fault branches on either side of the Punta Banda Peninsula is approximately 4 km, and the Valle Trinidad spring (VT) lies 135 km from La Jolla Beach (LJB). The fault exhibits both dip-slip movement upwards (U) and downwards (D). b) Topographic elevation profile displaying the main trace of the ABF (in red), as well as two additional profiles (in black and gray) that run 1.5 km parallel to the north and south of the main trace of the fault. Vertical axis exaggerated ~20 times. Numbers beside spring names show pH values of the thermal waters.

3.2. Materials and Methods

3.2.1. Water sampling and analysis

Fourteen thermal waters (hot springs, domestic thermal wells, intertidal seeps) located along the ABF were sampled in 2018 and 2019 (Table 3.1). On-site measurements were made for pH (to within ± 0.05 units with an OAKTON 150), temperature (to within ± 0.4 °C with a HANNA HI 93503 thermocouple), and electrical conductivity (EC, to within $\pm 1\%$ with a Thermo Scientific Orion 105A conductivity meter). Samples were filtered through a $0.45\ \mu\text{m}$ MILLIPORE filter and collected in 50 mL High-Density Polyethylene (HDPE) bottles. Samples for cation analysis were acidified using ultra-pure HNO_3 . Alkalinity was determined on-site on filtered water samples by titration with a $0.02\ \text{M}$ H_2SO_4 solution using bromocresol green and phenolphthalein as indicators.

Analyses were conducted at the geochemical laboratory of the Istituto Nazionale di Geofisica e Vulcanologia–Palermo (INGV–PA), Italy. Anion concentrations were determined using a Dionex ICS-1100 ion chromatograph and cations by Inductively Coupled Plasma Optical Emission Spectroscopy (ICP-OES) with a Jobin Yvon Ultima 2 spectrometer. Analytical uncertainty is $\leq 1\%$ for concentrations above $1\ \text{meq L}^{-1}$ and $\geq 5\%$ for lower concentrations. Values of $\delta^{18}\text{O}$ and $\delta^2\text{H}$ were determined by Continuous-Flow Isotope Ratio Mass Spectrometry (CF-IRMS). For $\delta^{18}\text{O}$, a Thermo Delta V mass spectrometer was used, while $\delta^2\text{H}$ values were determined using a Thermo Delta XP mass spectrometer. The isotopic ratios are expressed in δ -notation (‰) relative to Standard Mean Ocean Water (SMOW). Uncertainties are less than $\pm 0.1\text{‰}$ for $\delta^{18}\text{O}$ and $\pm 1\text{‰}$ for $\delta^2\text{H}$.

3.2.2. Gas sampling and analysis

Dissolved gases were sampled in $120\ \text{cm}^3$ glass flasks following the methodology of [Capasso & Inguaggiato \(1998\)](#) and [Inguaggiato & Rizzo \(2004\)](#). The gas phase in equilibrium with the water sample inside the glass flask was analyzed on an Agilent® 7890 gas chromatograph at the INGV–PA to determine N_2 , O_2 , and CO_2 with an analytical uncertainty of $\leq 5\%$. The resulting dissolved gas concentrations are reported in $\text{cm}^3\ \text{STP g}^{-1}\ \text{H}_2\text{O}$ ($0\ \text{°C}$ and $100\ \text{kPa}$) as calculated using Bunsen coefficients (Table 3.2, [Weiss, 1971](#); [Capasso & Inguaggiato, 1998](#); [Hamme & Emerson, 2004](#)).

Helium isotopes (^3He and ^4He), Ar, and ^{20}Ne dissolved in the water samples were analyzed. The gas phase in equilibrium with the water sample inside the glass flask was analyzed

with a GVI-Helix® SFT mass spectrometer, yielding raw ${}^3\text{He}/{}^4\text{He}$ isotopic ratios, R_{raw} , to within >3% analytical uncertainty. The R_{raw} ratios were normalized to the atmospheric ratio ($R_{\text{a}} = 1.40 \times 10^{-6}$; Sano & Wakita, 1985) and reported as $R_{\text{raw}}/R_{\text{a}}$ values (Table 3.2). Argon and Ne isotopes were analyzed with Helix MC-GVI and Thermo Scientific Helix MC Plus mass spectrometers, respectively, with analytical uncertainties <3%. The $R_{\text{raw}}/R_{\text{a}}$ values were corrected for air contamination (R/R_{a}) following Hilton (1996):

$$R/R_{\text{a}} = ((R_{\text{raw}} \times X) - 1) / (X - 1) \quad (3.1)$$

$$X = ({}^4\text{He}/{}^{20}\text{Ne})/({}^4\text{He}/{}^{20}\text{Ne})_{\text{air}} \times (\beta_{\text{Ne}}/\beta_{\text{He}}) \quad (3.2)$$

where X is the air-normalized ${}^4\text{He}/{}^{20}\text{Ne}$ ratio of the dissolved gases, $({}^4\text{He}/{}^{20}\text{Ne})_{\text{air}} = 0.318$, $\beta_{\text{Ne}} = 10.62$, and $\beta_{\text{He}} = 8.78$ are Bunsen coefficients for solubility of Ne and He in pure water (Weiss, 1971) assuming that meteoric water recharge occurs at the average temperature of the study area (17 °C).

3.2.3. ${}^4\text{He}$ production rate and water residence times

To estimate the average ${}^4\text{He}$ production rate in the study area, thirteen plutonic and volcanic rocks representing the most abundant lithology and chemical composition in the study area were sampled along the ABF (Figure 3.1b). Rock samples were processed following the Peters & Pettke (2017) methodology. This involved fine milling and pressing powder pills of the samples before measuring the concentrations of major elements and the parent radionuclides U and Th by Laser Ablation Inductively Coupled Plasma Mass Spectrometry (LA-ICP-MS) at the University of Bern, Switzerland (Table S3.1). A GeoLas-Pro 193 nm ArF Excimer laser system (Lambda Physik, Göttingen, Germany) was used coupled with an ELAN DRC-e quadrupole mass spectrometer (Perkin Elmer, Waltham, MA, USA). Data were reduced using the SILLS software (Guillong et al., 2008). Average detection limits for SiO_2 , Na_2O , K_2O , Th, and U are 0.0001 to 0.012 $\mu\text{g g}^{-1}$, and standard deviations of the concentrations are 0.034 to 0.536.

In crustal rocks, ${}^4\text{He}$ is produced from α -decay of ${}^{235}\text{U}$, ${}^{238}\text{U}$ and ${}^{232}\text{Th}$, and it eventually dissolves into any groundwater present. Therefore, high ${}^4\text{He}$ concentrations typify groundwaters with long subsurface residence times (Andrews & Lee, 1979). In granitic rocks, the concentrations of U and Th are high, and dissolved ${}^4\text{He}$ concentrations may exceed the aqueous solubility of helium (Marine, 1979). Water residence times can be estimated from the ${}^4\text{He}$ production rate (${}^4\text{He}_{\text{pro}}$) in the wall rocks along the groundwater flowpath and the ${}^4\text{He}$ present in

the thermal waters in excess of that due to equilibrium with the atmosphere upon recharge (Torgersen, 1980; Kulongoski et al., 2008). This excess ^4He , corrected for air contamination ($\text{cm}^3 \text{ STP g}^{-1} \text{ H}_2\text{O}$), is calculated as follows:

$$^4\text{He}_{\text{ex}} = ^4\text{He}_s - ^4\text{He}_{\text{ASW}} - (^{20}\text{Ne}_s - ^{20}\text{Ne}_{\text{ASW}} \times (\text{He/Ne})_{\text{ASW}}) \quad (3.3)$$

where $^4\text{He}_s$ and $^{20}\text{Ne}_s$ ($\text{cm}^3 \text{ STP g}^{-1} \text{ H}_2\text{O}$) are concentrations measured in the sample, $^4\text{He}_{\text{ASW}}$ and $^{20}\text{Ne}_{\text{ASW}}$ are the concentrations in pure air-saturated water at the mean annual recharge temperature of 17 °C (4.52×10^{-8} and $1.89 \times 10^{-7} \text{ cm}^3 \text{ g}^{-1} \text{ H}_2\text{O}$, respectively), and $(\text{He/Ne})_{\text{ASW}}$ is the He/Ne ratio in air-saturated water (0.2882, Weiss, 1971). When $^{20}\text{Ne}_s < ^{20}\text{Ne}_{\text{ASW}}$, Eq. (3.3) reduces to

$$^4\text{He}_{\text{ex}} = ^4\text{He}_s - ^4\text{He}_{\text{ASW}} \times (^{20}\text{Ne}_{\text{ASW}} / ^{20}\text{Ne}_s) \quad (3.4)$$

The He production rate ($^4\text{He}_{\text{pro}}$, $\text{cm}^3 \text{ yr}^{-1} \text{ g}^{-1} \text{ H}_2\text{O}$) is defined as

$$^4\text{He}_{\text{pro}} = \rho_r A \times (1.19 \times 10^{-13} \times \text{U} + 2.88 \times 10^{-14} \times \text{Th}) \times (1 - \phi) / (\phi) \quad (3.5)$$

where ρ_r is the bulk density of the wall rock (g cm^{-3}), ϕ is the fracture porosity through which advective water flow occurs, A is the fraction of He produced in the rock that is subsequently released into the groundwater (here A is assumed to be equal to 1), and U and Th are the uranium and thorium concentrations in the rock ($\mu\text{g g}^{-1}$), with decay rates of 1.19×10^{-13} and $2.88 \times 10^{-14} \text{ cm}^3 \text{ STP } ^4\text{He yr}^{-1} \mu\text{g}^{-1}$, respectively (Kulongoski et al., 2008). To solve Eq. (3.5), we used the average concentrations of $1.2 \mu\text{g g}^{-1} \text{ U}$ and $4.9 \mu\text{g g}^{-1} \text{ Th}$ in the rocks along the ABF (Table S3.1). Ignoring any deep crustal flow entering the system, the water residence time is given by the ratio $^4\text{He}_{\text{ex}} / ^4\text{He}_{\text{pro}}$ (Eqs. 3.3–3.5).

3.2.4. Hypocenter depths and rheological models

We used a multi-step approach to estimate the regional geothermal gradients along the ABF, which are essential for understanding the thermal regime of the area and estimating the fluid circulation depth by solute geothermometry. First, we identified the depth of the BDTZ based on the depths of earthquake hypocenters. Rheological models were then employed to determine

the local temperature and hence geothermal gradient that are consistent with the independently determined variations in BDTZ depth along the ABF.

The BDTZ is a depth range within the Earth's crust where the mechanical behavior of rocks changes from brittle fracturing to ductile flow (Sibson, 1983). Its depth depends on several factors, including temperature, pressure, strain rate, active shear zone thickness, and rock composition (e.g., Brodi & Iizuka, 1993a, 1993b; Dragoni, 1993; Brodi, 1996; Bonner et al., 2003; Erkan & Blackwell, 2009; Zuza & Cao, 2020). To determine the depth of the BDTZ along the ABF we analyzed the depth distribution of crustal hypocenters, following a well-established methodology similar to previous studies (Michailos et al., 2020; Zuza & Cao, 2020). The seismic data set is comprised of 190 earthquakes recorded since 2001 (Figure 3.1b; Supplementary Material: “Hypocentral_Depths_dataset.xlsx”). Of these, 116 events with magnitudes of 1.0 to 3.3 and with hypocentral uncertainties less than 60% were selected from RESNOM (2017). In addition, 74 events with magnitudes of 1.5 to 2.1 and with hypocentral uncertainties less than 1 km were sourced from Frez et al. (2004). From the normalized cumulative frequency distributions of these hypocenter depths, we determined the 5th and 95th percentiles. We then applied a weighted linear regression to the filtered depth data and to the filtered depth errors and calculated their standard deviations. To evaluate the precision of our analysis, we computed the residuals and standard deviations of the regressions, yielding the uncertainty in depth of the seismically determined BDTZ. The Python code for these estimations is provided in the Supplementary Material (“Hypocentral_Depths_Analysis.py”).

The next steps were to fit rheological models to the BDTZ depths as inferred above and calculate the geothermal gradients along the three sections of the ABF. The models incorporate a combination of frictional (brittle) and quasi-plastic (ductile) deformation mechanisms to describe the deformational behavior of rocks in the BDTZ, as follows. The transition between these two mechanisms occurs gradually over a range of temperatures and stresses.

The frictional regime (e.g., brittle) is represented by Byerlee's Law. This widely-used empirical relationship predicts the strength of faults based on the coefficient of sliding friction and the applied differential stress (Eq. 3.6). This equation relates the shear stress (τ) and the effective normal stress (σ_n) (MPa) acting upon the fault plane during sliding. For immature faults like the ABF, which have poorly-developed gouge zones and limited recent slip, Byerlee's Law predicts coefficients of sliding friction (μ) between 0.6 and 0.8 and fault strengths exceeding 100 MPa (σ_n) at seismogenic depths (Byerlee, 1978; Marone, 1995). We treat the fault rock

along the entire ABF as a homogeneous granite, since at the large scale the Peninsula Batholith is ubiquitous at depth, likely including at depths relevant to the BDTZ (Gastil et al., 1975; Ortega-Rivera 2003). At the local scale, the fault also traverses rheologically weaker greenschist-facies metavolcanic and metasedimentary rocks of the Alisitos Formation, which occupy the interstices between individual granite plutons. However, their exact distribution at depth is unknown. We therefore use a typical coefficient of friction (μ) for granite between 0.6 and 0.7 (Chester, 1995; Ikari et al., 2011).

$$\tau = \mu\sigma_n \quad (3.6)$$

In the ductile regime, dislocation creep dominates the deformation behavior of quartz, especially at high temperatures, resulting in plastic deformation of the granite (Sibson, 1982). Therefore, the appropriate constitutive flow law for this process is modeled by the Power Law Creep equation (Eq. 3.7).

$$\sigma_d = [\dot{\epsilon}/A_1]^{1/n} \exp[E^*/RT] \quad (3.7)$$

where σ_d is the differential stress (MPa) representing the difference between maximum and minimum principal stresses inducing deformation through dislocation creep, $\dot{\epsilon}$ is the plastic strain rate (s^{-1}), A_1 is a material constant ($MPa^{-n} s^{-1}$), E^* is the activation energy ($kJ mol^{-1}$), n is the stress exponent (dimensionless), R is the gas constant ($8.31 J mol^{-1} K^{-1}$), and T is the temperature ($^{\circ}C$). To solve Eq. 3.7, we used the experimental values of wet granite, for which $n = 1.9$, $E^* = 137 kJ mol^{-1}$, and $A_1 = 2.0 \times 10^{-4} MPa^{-n} s^{-1}$ (Ranalli & Murphy, 1987).

The effects of different assumed slip rates (2, 3 and 4 $mm yr^{-1}$) and fault widths (0.1, 0.5 and 1 km) were tested to estimate feasible strain rates for the ABF, resulting in values from 6.3×10^{-14} to $1.3 \times 10^{-12} s^{-1}$. With these parameter values (Table S3.2), the rheological models successfully reproduced the depths of the BDTZ estimated by the hypocenter analysis and allowed derivation of regional geothermal gradients. Although these models utilize assumed values of lithology, coefficient of friction, and fault widths at depth along the ABF, the calculated BDTZ depths provide an internally consistent approximation for the regional geothermal gradients.

3.3. Results

3.3.1. Water chemistry

Thermal springs are the primary surface expression of geothermal systems along the ABF, with up to six such springs occurring at each site. Table 3.1 lists the physicochemical parameters of the sampled thermal waters. Towards the northwest along the fault, discharge temperatures increase from 37 to 102 °C, while pH decreases from 9.8 to 5.3 (Figure 3.2b). The total concentrations of dissolved solids (TDS) show a remarkably wide variation, which divides the samples into two geographic groups: inland versus coastal–submarine (Table 3.1). The inland samples are located far from the ocean (>30 km, Figure 3.2b) and have low TDS of 0.3–0.9 g L⁻¹, whereas the coastal–submarine samples are more saline with TDS of 8–19 g L⁻¹. The coastal–submarine group includes waters from six shallow domestic thermal wells, the coastal thermal anomaly at La Jolla beach (Figure 3.1c), and the fumarolic submarine field. The solutes in all thermal waters are dominated by Na and Cl, with the coastal–submarine samples exhibiting an enrichment in Ca, Li, B (Figure 3.3a), and SiO₂ compared with seawater. All thermal water samples show a strong linear correlation between Na and Cl concentrations ($R^2 = 0.99$; Figure 3.3b), reflecting binary mixing with seawater. In contrast, Mg concentrations are depleted in the coastal–submarine samples compared to the binary seawater mixing line (Figure 3.3c), demonstrating that Mg does not behave conservatively.

3.3.2. Stable O–H isotopes of thermal waters

Values of $\delta^{18}\text{O}$ and $\delta^2\text{H}$ in the thermal waters range from -3.5 to -8.5‰ and -25.4 to -61‰, respectively (Table 3.1). Inland samples fall in the $\delta^{18}\text{O}$ and $\delta^2\text{H}$ ranges values of modern rainfall in southern California and Baja California (Williams & Rodoni, 1997; Kretzschmar & Frommen, 2013) and have delta values lower than coastal–submarine samples and local seawater (in which $\delta^{18}\text{O}$ is -0.6 and $\delta^2\text{H}$ is -3.5‰; Figure 3.3d). Most thermal water samples plot close to the Global Meteoric Water Line (GMWL, Craig, 1961), demonstrating their meteoric origin. The deviation from the GMWL observed for the coastal–submarine waters is consistent with the admixture of seawater, in accord with the correlations between Na and Cl concentrations (Figure 3.3b) and between $\delta^2\text{H}$ and Cl values (Figure 3.3e).

To estimate the fraction of admixed seawater (F_{sw}) in the coastal–submarine samples, we assume a binary mixing model:

$$F_{sw} = (Cl_{tw} - Cl_{mw}) / (Cl_{sw} - Cl_{mw}) \quad (3.8)$$

where Cl_{tw} is the Cl concentration measured in the thermal water sample, and Cl_{mw} and Cl_{sw} are the concentrations of Cl in meteoric water and seawater, respectively. Given the low Cl concentrations in the inland waters, we assume that the meteoric water is Cl-free for this calculation, and we use our measured Cl concentration in local seawater ($18,967 \text{ mg L}^{-1}$, Table 3.1) as a seawater endmember. This mass balance reveals that the coastal–submarine samples contain between 25 and 57 mass% seawater (Table S3.3). These fractions allow reconstruction of the initial isotopic signatures of the coastal–submarine samples before their mixing with seawater ($\delta^{18}O_i$ and δ^2H_i), e.g., for oxygen:

$$\delta^{18}O_i = (\delta^{18}O_{tw} - F_{sw} \times \delta^{18}O_{sw}) / (1 - F_{sw}) \quad (3.9)$$

Figure 3.3f shows the initial $\delta^{18}O_i$ and δ^2H_i values for the coastal–submarine samples (Table S3.3), which are close to the inland thermal waters and the GMWL. The same binary mixing model was used to calculate the theoretical discharge temperature of the thermal springs to correct for cooling caused by the admixture of seawater. This resulted in unmixed discharge temperatures between 33 and 212 °C for the coastal–submarine samples (Table S3.3).

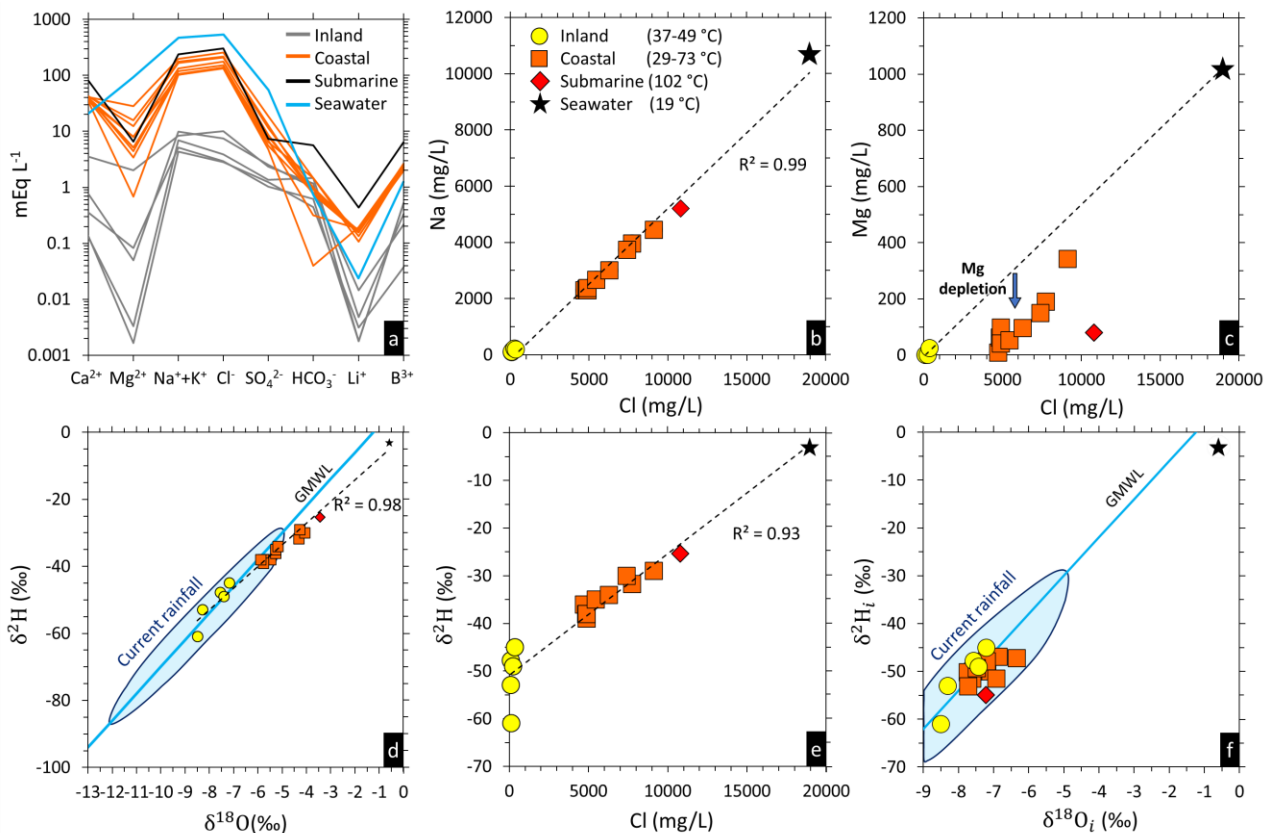


Figure 3.3. Element and stable O–H isotope correlations in thermal water samples. a) Schoeller diagram of thermal waters sampled along the Agua Blanca Fault. b) Sodium vs. chlorine concentrations indicating binary mixing between seawater and thermal waters. All thermal water samples were considered in estimating the R^2 value of 0.99. c) Magnesium vs. chlorine concentrations illustrating the Mg depletion of coastal–submarine samples compared to the conservative mixing trend with seawater. d) Plot of $\delta^{18}\text{O}$ vs. $\delta^2\text{H}$ indicating that the thermal waters are of meteoric origin. Current $\delta^{18}\text{O}$ and $\delta^2\text{H}$ values of rainfall in southern California and Baja California are represented by a blue oval (Williams & Rodoni, 1997; Kretzschmar & Frommen, 2013). e) Plot of $\delta^2\text{H}$ vs. Cl showing that the coastal–submarine waters contain admixed seawater. f) Initial values of O–H isotopes ($\delta^{18}\text{O}_i$ and $\delta^2\text{H}_i$), with coastal–submarine waters corrected for the admixture of seawater (see text; exact values provided in Table S3.3). GMWL: global meteoric water line (Craig, 1961).

Table 3.1

Chemical and isotopic compositions of thermal waters collected along the Agua Blanca Fault. Individual solute concentrations are given in mg L⁻¹. T_{Geot} values are temperatures calculated from solute geothermometers. Stable isotope ratios are expressed as δ values (‰) relative to Standard Mean Ocean Water (SMOW).

Class	Type	Sample	T^u (°C)	T_{Geot} (°C)	pH	TDS (g L ⁻¹)	Na ⁺	K ⁺	Mg ²⁺	Ca ²⁺	Li ⁺	Cl ⁻	SO ₄ ²⁻	Br ⁻	HCO ₃ ⁻	F ⁻	SiO ₂	$\delta^{18}O$ (‰)	δ^2H (‰)		
Inland	Spring	VT	37	105 ^b	9.8	0.51	156	1.9	0.04	2.65	33	137	66	bdl	90	2.1	53.5	-8.5	-61.0		
		SV	46	103 ^b	9.4	0.34	100	1.1	0.02	2.7	22	100	59	bdl	27	3.3	45.9	-7.6	-47.8		
		ST ^d	49	108 ^b	9.4	0.37	118	1.5	1.0	7.1	NM	105	49	bdl	38	11.6	41.4	-8.3	-53.0		
		UR	47	112 ^b	8.6	0.75	225	3.1	0.6	15.2	100	266	121	0.8	61	4.5	52.7	-7.4	-49.0		
	Well	AJ	43	121 ^b	7.0	0.88	192	3.2	24.6	70.7	12	357	113	1.1	72	1.8	43.3	-7.2	-45.0		
Coastal	Wells at La Jolla	W368	50	113 ^c	6.9	8.60	2341	93.6	61.8	766.3	1126	4849	386	15.5	56		48.0	-5.5	-38.0		
		W369	73	132 ^c	5.3	8.11	2289	112.0	8.2	685.1	1355	4714	231	17.3	2.4		68.8	-5.3	-36.0		
		W363	30	137 ^c	6.5	8.63	2208	93.6	61.8	766.3	1149	4849	386	bdl	56		74.9	-5.8	-38.0		
		W2014	29	128 ^c	6.2	8.53	2294	82.2	97.8	700.4	924	4894	312	bdl	90		63.0	-5.8	-39.0		
	Thermal anomaly La Jolla beach	W367	38	138 ^c	6.5	8.52	2370	100.5	41.6	729.6	1171	4888	264	bdl	49	bdl		75.5	-5.9	-38.0	
		WAGC	45	147 ^c	6.4	9.50	2659	108.7	53.1	802.1	1255	5442	332	bdl	20			85.8	-5.3	-35.0	
	Submarine	Vent	LJB-a	50	156 ^c	6.8	13.63	3961	145.6	190.0	832.9	1089	7738	614	23.7	46			82.8	-4.3	-31.7
			LJB-b	55	158 ^c	6.7	12.99	3733	140.5	150.2	846.9	1120	7396	557	21.7	61			87.3	-4.1	-30.0
			LJB-c	60	152 ^c	6.4	10.86	3002	122.1	95.8	786.2	1183	6279	420	21.3	46			87.2	-5.2	-34.0
			LJB-d	46	137 ^c	6.9	15.96	4440	161.4	342.6	819.7	743	9120	904	33.4	90			53.1	-4.3	-29.0
Submarine	Vent	SMF ^d	102	128	6.1	18.95	5200	410.0	80.0	1600.0	3000	10800	351	NM	347	1.8	156	-3.5	-25.4		
Seawater	Seawater	SW	19	-	8.1	34.20	10729	329.9	1021.3	413.0	165	18967	2610.2	67.4	45	bdl	2.3	-0.6	-3.0		

bdl: Data below detection limit; ^a Measured discharge temperature of spring;

^c Temperatures calculated using unmixed quartz geothermometer;

NM: not measured; ^b Temperature calculated using Na/K geothermometer;

^d Data from [Vidal et al. \(1981\)](#) and [Zúñiga \(2010\)](#).

3.3.3. Gas chemistry of thermal waters

Nitrogen is the dominant gas dissolved in the thermal waters, with concentrations ($1.0\text{--}2.3 \times 10^{-2} \text{ cm}^3 \text{ STP g}^{-1} \text{ H}_2\text{O}$, Table 3.2) mostly higher than that in air-saturated water (ASW) ($1.2 \times 10^{-2} \text{ cm}^3 \text{ STP g}^{-1} \text{ H}_2\text{O}$, Table 3.2). The volume ratios of N_2/Ar in inland and coastal thermal waters (10–38) approach that in ASW (38.6). In contrast, the submarine sample SMF has an N_2/Ar ratio of 160. According to Vidal et al. (1982), such a value may originate from the decomposition of nitrogenous compounds in sediments. The second most abundant gas is O_2 , which has a lower concentration ($1.4\text{--}25 \times 10^{-4} \text{ cm}^3 \text{ STP g}^{-1} \text{ H}_2\text{O}$) than ASW ($66 \times 10^{-4} \text{ cm}^3 \text{ STP g}^{-1} \text{ H}_2\text{O}$). Depletion in O_2 is likely due to its reduction by reaction with wall rocks during deep fluid circulation. Most of the thermal waters have lower CO_2 concentrations ($0.1\text{--}0.3 \times 10^{-3} \text{ cm}^3 \text{ STP g}^{-1} \text{ H}_2\text{O}$) than ASW ($0.3 \times 10^{-3} \text{ cm}^3 \text{ STP g}^{-1} \text{ H}_2\text{O}$). The exceptions are three samples from shallow wells W368, W369, and AJ, which have higher values ($4\text{--}17 \times 10^{-3} \text{ cm}^3 \text{ CO}_2 \text{ STP g}^{-1} \text{ H}_2\text{O}$), presumably due to microbial activity in the wells.

Concentrations of ^4He are in the range $0.6\text{--}6.2 \times 10^{-6} \text{ cm}^3 \text{ STP g}^{-1} \text{ H}_2\text{O}$ (Table 3.2) and are up to 13–136 times higher than ASW ($4.55 \times 10^{-8} \text{ cm}^3 \text{ STP g}^{-1} \text{ H}_2\text{O}$). The volume ratios of $^4\text{He}/^{20}\text{Ne}$ are 7–92 times higher than those measured in ASW (0.28). The concentrations of ^4He and ^{20}Ne in coastal samples were recalculated (Table 3.2) assuming binary mixing with air-saturated seawater (ASSW), using the He and Ne concentrations in ASSW at 17 °C (3.83×10^{-8} and $1.60 \times 10^{-7} \text{ cm}^3 \text{ g}^{-1} \text{ H}_2\text{O}$; Sano & Takahata, 2005) and the estimated seawater fractions (Table S3.3).

The $^3\text{He}/^4\text{He}$ ratios were corrected for air contamination and seawater mixing (R) and normalized to the value of air (denoted R/R_a), varying from 0.06 to 0.94. The coastal samples contain the lowest ^4He concentrations ($0.6\text{--}1.7 \times 10^{-6} \text{ cm}^3 \text{ STP g}^{-1} \text{ H}_2\text{O}$), $^4\text{He}/^{20}\text{Ne}$ ratios (2–5), and R/R_a ratios (0.06–0.26). As helium shows negligible isotopic fractionation during water–gas interaction, the R/R_a value can be used to track the origin of the gas in terms of the air, mantle, and crust endmembers. Figure 3.3 shows R/R_a versus $^4\text{He}/^{20}\text{Ne}$ ratios for ASW ($R/R_a = 1$), radiogenic crust ($R_r = (R/R_a)_{\text{radiogenic}} = 0.015$, Sano & Wakita, 1985), and the mantle as represented by MORB (Mid-Ocean Ridge Basalt). For the MORB endmember, we used the highest R/R_a value measured in the Alarcón basin in the nearby Gulf of California ($R_m = (R/R_a)_{\text{MORB}} = 8.38$; Castillo et al., 2002). Figure 3.4a indicates that He dissolved in the thermal waters derives mainly from radiogenic decay.

The fractions of mantle helium (F_m) in the waters were calculated from the R values in Table 3.2 according to the following equation (modified from Sano & Wakita, 1985):

$$F_m = (R - R_r) / (R_r + R_m) \quad (3.10)$$

with the remainder ($1 - F_m$) being equal to the fraction of radiogenic helium (F_r). This shows that mantle ^3He makes up less than 11% of the total He in the samples (Figure 3.4a). Notably, the lowest mantle contributions (0.6–2.9%) are found in the coastal samples (Table 3.2). Owing to the lack of ^{20}Ne analyses of the submarine sample SMF (Vidal et al., 1982) and of an $^3\text{He}/^4\text{He}$ analysis of the subaerial sample ST (Zúñiga, 2010), the mantle and radiogenic He contributions in these springs cannot be estimated.

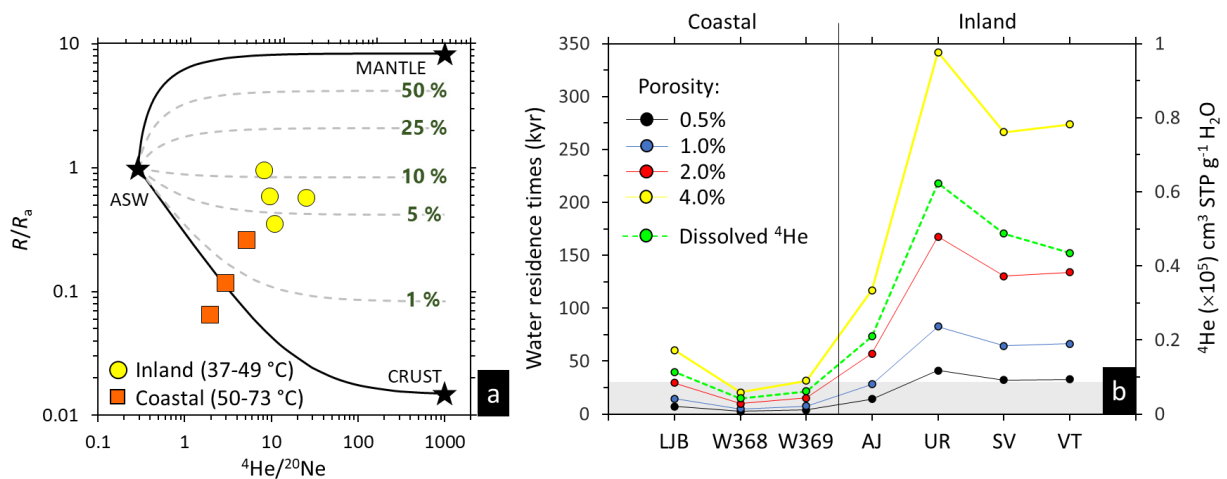


Figure 3.4. Estimation of helium sources and water residence times for inland and coastal thermal waters along the Agua Blanca Fault. (a) Helium-neon isotopic composition (R/R_a vs. $^4\text{He}/^{20}\text{Ne}$) of the thermal waters, with endmembers representing compositions of the mantle (Castillo et al., 2002), crust (Sano & Wakita, 1985), and air (plotted on logarithmic axes). Dashed lines indicate mantle contributions in the samples. (b) Estimated water residence times for several assumed porosity values, with corresponding concentrations of ^4He dissolved in the thermal waters (dashed green line) given on the right-hand y-axis. Note that if the porosity below the LJB site is assumed to be 2% and that that below the inland springs is assumed to be 0.5%, then all waters have approximately the same residence time (indicated by gray band).

3.3.4. Water residence times

Fracture porosity is an important variable in calculating ^4He -based water residence times from Eqs. 3.3 to 3.5. Differences in host rock lithologies along the ABF may have some influence on the distribution and magnitude of fracture porosity within the fault, and hence on permeability, but the variability of lithologies in the Alisitos Formation makes it difficult to predict if it would systematically develop higher or lower fracture porosities than the granite. As no hydraulic test results are available from the ABF to constrain porosity values, we simply assumed a plausible range of fracture porosities from 0.5 and 4.0%. This chosen range is comparable to that derived from worldwide borehole hydraulic tests in crystalline rocks (0.1–2.3%; [Stober & Bucher, 2007](#) and references therein). A fracture porosity of 0.5% yields residence times between 2 and 41 kyr (Figure 3.4b), with noticeably shorter residence times for the coastal springs. Conversely, with a fracture porosity of 4%, the residence times are substantially higher (20 to 342 kyr) and they span a very wide range. Nevertheless, Figure 3.4b demonstrates that the residence times of water in coastal springs consistently remain lower than those of the inland springs, unless the ratio of their fracture porosities exceeds a factor of approximately three. While the fracture porosity in the Punta Banda coastal system may be higher due to greater fault extension, the very high discharge temperatures at the coast suggest that the thermal waters there indeed have the shortest residence times of all the springs.

Table 3.2

Chemical and isotopic compositions of gases dissolved in thermal waters (sample type DG, expressed in cm^3 STP g^{-1} H_2O) and of bubbling gases (type BG, expressed in volume %) along the Agua Blanca Fault.

Sample	Type	N_2 ($\cdot 10^{-2}$)	O_2 ($\cdot 10^{-4}$)	CO_2 ($\cdot 10^{-3}$)	^4He ($\cdot 10^{-6}$)	^{20}Ne ($\cdot 10^{-7}$)	$^4\text{He}_{\text{ex}}$ ($\cdot 10^{-6}$)	N_2/Ar	$^4\text{He}/^{20}\text{Ne}$	$R_{\text{raw}}/R_{\text{a}}^{\text{a}}$	$\pm R/R_{\text{a}}^{\text{b}}$ ($\cdot 10^{-3}$)	$R/R_{\text{a}}^{\text{c}}$	F_{m}^{d} (%)	F_{r}^{e} (%)	Age ^f (kyr)
VT ^g	DG	1.50	1.37	0.33	4.35	1.68	4.85	28.4	25.9	0.57	6.1	0.56	6.6	93.4	66
SV ^g	DG	2.30	6.39	0.10	4.88	5.75	4.72	13.9	8.5	0.95	9.6	0.94	11.1	88.9	65
UR ^g	DG	1.79	6.61	0.27	6.23	6.34	6.06	9.8	9.8	0.59	8.4	0.58	6.7	93.3	83
AJ ^g	DG	1.65	1.66	17.0	2.10	1.88	2.07	37.8	11.2	0.36	6.6	0.35	4.0	96.0	28
W369	DG	1.00	25.3	4.37	0.81 ^h	2.67 ^h	0.56	32.1	3.0	0.19	7.1	0.12 ^h	1.2	98.8	8
W368	DG	1.30	6.20	13.8	0.56 ^h	2.76 ^h	0.36	33.8	2.0	0.19	9.1	0.06 ^h	0.6	99.4	5
LJB-c	DG	NM	NM	NM	1.70 ^h	3.22 ^h	1.07		5.2	0.29	4.6	0.26 ^h	2.9	97.1	15
SMF ⁱ	BG	56.1	0.29	1.8	0.08	NM		160		0.54					
ASW ⁱ		1.23	66.0	0.31	0.045	1.63		38.6	0.28						

^a Raw measured $^3\text{He}/^4\text{He}$ ratio (R_{raw}) normalized to the $^3\text{He}/^4\text{He}$ ratio of air (R_{a});

^b Uncertainty in $R_{\text{raw}}/R_{\text{a}}$;

^c $^3\text{He}/^4\text{He}$ ratio (R) corrected for air contamination and normalized to the $^3\text{He}/^4\text{He}$ ratio of air (R_{a});

^d Fraction of mantle He (see text);

^e Fraction of radiogenic He (see text);

^f Water residence times derived from Eqs. (3–5), considering a porosity of 1%.

^g Inland samples. Other samples are coastal (W369, W368, LJB-c) or submarine (SMF).

^h Concentrations and isotopic values corrected for admixed seawater based on fractions in Table S3.3, and air-saturated seawater values (see text);

ⁱ Values of SMF from [Vidal et al. \(1981\)](#) and air-saturated water values from [Capasso & Inguaggiato \(1998\)](#);

NM: not measured.

3.3.5. Brittle–ductile transition zone and geothermal gradient

The analysis of seismic hypocenters along the ABF suggests that the depth of the BDTZ increases systematically from northwest to southeast (Figure 3.5a). In the Punta Banda Zone, the estimated BDTZ depth is at 12 ± 0.88 km. In the Santo Tomas – Agua Blanca – Dolores Zone (central section of ABF) and the Trinidad Zone (southeastern section) it is at 15 ± 0.98 km, and 19 ± 1.20 km, respectively. The rheologic models that reproduce these BDTZ depths require the geothermal gradient to decrease progressively from northwest to southeast, with Punta Banda having an estimated range of $20\text{--}25$ °C km⁻¹, Santo Tomas – Agua Blanca – Dolores exhibiting a lower gradient of $16\text{--}19$ °C km⁻¹, and Trinidad displaying an even lower gradient of $12\text{--}15$ °C km⁻¹ (Figure 3.5b). The range of the geothermal gradient in each zone depends on the different parameters used in the models. In general, the calculated geothermal gradient decreases at lower strain rates, lower coefficients of friction, and higher fault widths, while it increases at higher slip rates (Table S3.2). We estimate that the BDTZ along the ABF occurs at an average temperature of $230\text{--}300 \pm 14\text{--}22$ °C. This interval agrees well with the onset of plastic deformation in quartz (280 °C– 400 °C; [Stipp et al., 2002](#); [Violay et al., 2017](#)).

The geothermal gradient estimated for the Trinidad Zone ($12\text{--}15$ °C km⁻¹) in the east is in good agreement with temperature measurements in a well located 40 km southeast of the ABF in the San Pedro Mártir range, which indicates a geothermal gradient of 14.9 °C km⁻¹ ([Smith et al., 1979](#)). Moreover, the range of geothermal gradients estimated along the entire ABF ($12\text{--}25$ °C km⁻¹) is consistent with other amagmatic regions, with the absence of volcanism since the Miocene, and with the fact that all local intrusive rocks are older than 90 Ma ([Storey et al., 1989](#); [Ortega-Rivera, 2003](#)). The reported low heat flow values for Southern California (< 60 mW m⁻²) provide additional evidence supporting our findings. The low heat flow likely represents a residual effect of the outer arc thermal conditions that existed during the subduction of the Farallon plate, which ended ~ 30 Ma ago, resulting in a cooling effect on Southern California and Baja California ([Erkan & Blackwell, 2009](#)).

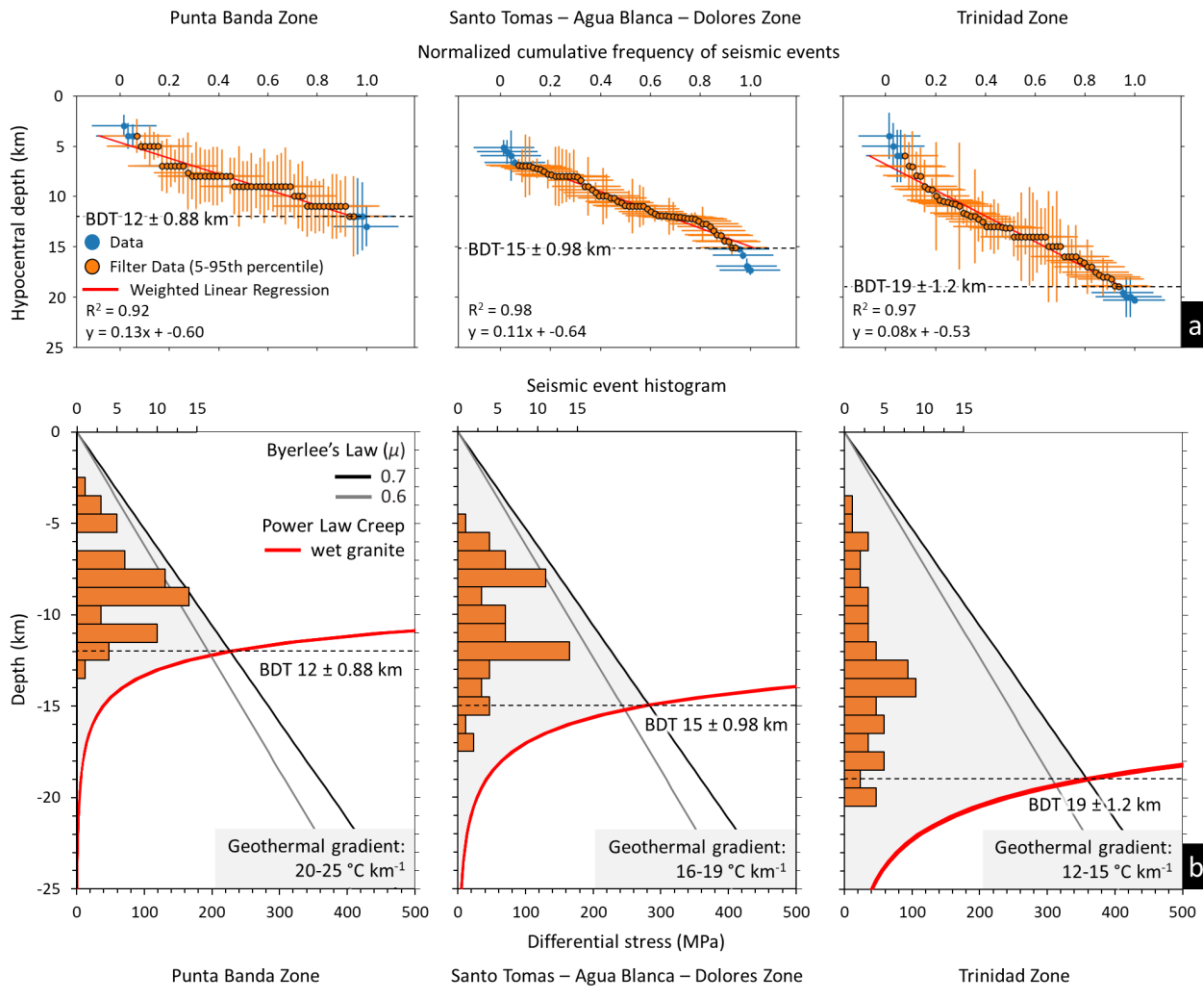
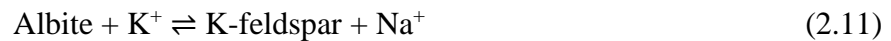


Figure 3.5. Analysis of seismic hypocenters and rheological models along the Agua Blanca Fault (see locations of geographic zones in Figure 3.1b). a) Identification of depth levels of the brittle–ductile transition zone (BDTZ) in each zone based on filtered seismic data. The 5th to 95th percentiles of the normalized cumulative frequency are shown as orange dots, along with their errors (orange lines). Discarded data are represented by blue dots and blue lines. b) Estimation of the range of geothermal gradients in each geographic zone by fitting the intersection of Byerlee's Law (black and gray lines) and Power-Law Creep (red curve) for wet granite to the estimated BDTZ in Figure 3.5a. Orange bars represent the histogram of seismic hypocenters.

3.3.6. Minimum temperature and depth of water–rock equilibration

The Peninsular Ranges Batholith of Baja California is dominantly tonalite and granodiorite, hence it contains abundant feldspar and quartz. This permits the assumption that the aqueous concentrations of Na, K, and SiO₂ are buffered by reactions with these minerals at high temperatures along the deep water flowpaths. Thus, classical solute geothermometers can provide constraints on the temperatures attained by the thermal waters during their circulation within the ABF system. For the equilibrium



the temperature dependency of the molar Na/K concentration ratio is taken from [Giggenbach \(1988\)](#):

$$T_{\text{Na/K}} (\text{°C}) = (1390 / \log (\text{Na/K} + 1.75)) - 273.15 \quad (2.12)$$

Similarly, for the quartz equilibrium



[Fournier & Potter \(1982\)](#) determined the temperature dependency at low to moderate pH values as follows:

$$T_{\text{quartz}} (\text{°C}) = -42.198 + 0.28831[\text{SiO}_2] - 3.36686 \times 10^{-4} [\text{SiO}_2]^2 + 3.1665 \times 10^{-7} [\text{SiO}_2]^3 + 77.034 \times \log [\text{SiO}_2] \quad (2.14)$$

[Fournier \(1977\)](#) determined that at lower temperatures (<110 °C), other silica phases, such as chalcedony, may control the dissolved silica concentration:

$$T_{\text{chalcedony}} (\text{°C}) = 1032 / 4.69 - \log [\text{SiO}_2] \quad (2.15)$$

In equations (14) and (15), [SiO₂] refers to the silica concentration in mg L⁻¹.

Water–mineral reactions typically slow down during the ascent and cooling of thermal water, causing it to deviate from the equilibrium state. This implies that the metastable solute concentrations measured in surface springs (Table 3.1) represent their values when the water was last in equilibrium with the buffering minerals ([Fournier et al., 1973](#)). Given that reaction kinetics change only gradually and that rock temperatures increase progressively with depth, the reconstructed equilibration temperatures are considered to be minimum estimates.

The minimum equilibration temperatures obtained from the Na/K, quartz, and chalcedony geothermometers are shown in Figure 3.6. The quartz and chalcedony geothermometers should not be applied to the inland samples (dashed red and green lines in Figure 3.6) because their pH is up to 9.8, causing an increase in silica solubility that is not captured by the geothermometer calibrations in Eq. 3.14 and 3.15. On the other hand, in the coastal–submarine thermal waters, the molar Na/K ratios of 13–28 dominantly reflect admixture of seawater (molar $\text{Na/K}_{\text{seawater}} = 33$) rather than buffering by albite and K-feldspar, thereby precluding the application of the Na/K geothermometer (dashed black in Figure 3.6). To solve the latter issue, we used the quartz and chalcedony geothermometers (Eq. 3.14, 3.15) to estimate the equilibration temperature of the coastal–submarine thermal waters. To account for mixing with seawater, we used a binary mixing model with the derived seawater fractions and the seawater SiO_2 concentration of 2.3 mg L^{-1} to estimate the SiO_2 concentration in the thermal endmember water via Eqs. 3.14 and 3.15 (Table S3.3).

The minimum equilibrium temperatures for inland geothermal systems are between 103 and 121 °C (Na/K geothermometer), increasing from southeast to northwest along the ABF (Figure 3.6). In contrast, the minimum equilibrium temperatures for the coastal–submarine systems are 84 to 209 °C (chalcedony geothermometer). The hottest values are in the coastal geothermal anomaly at La Jolla beach and the fumarolic submarine field (133 and 209 °C, respectively, chalcedony geothermometer).

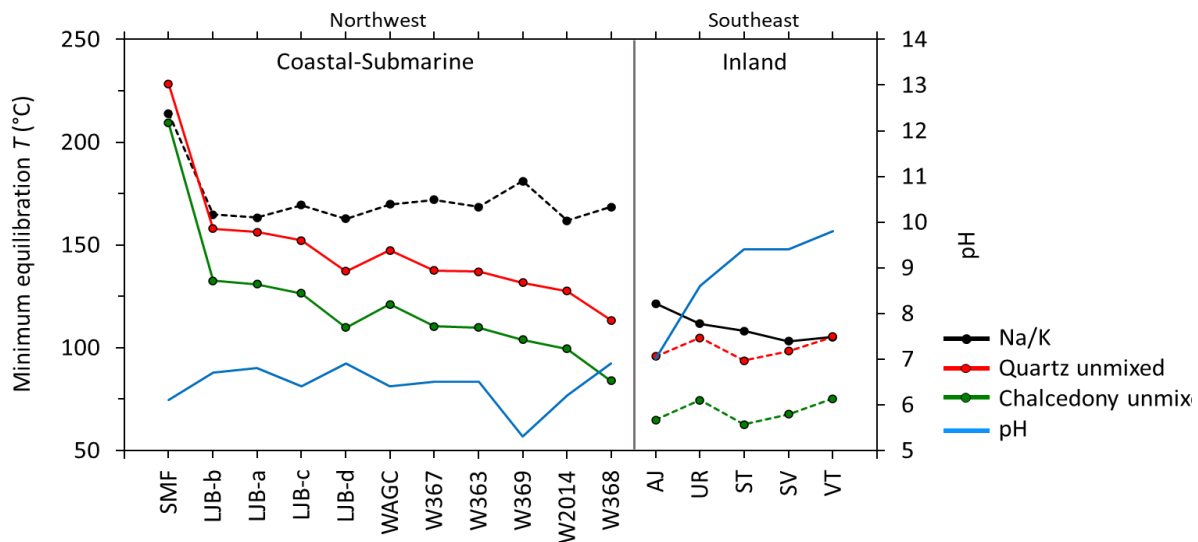


Figure 3.6. Minimum temperatures of the thermal waters at depth along the Agua Blanca Fault, from NW to SE, estimated using Na/K and SiO_{2(aq)} geothermometry (see text for interpretation). The pH values measured at the spring discharge temperatures are indicated on the right-hand y axis. Dotted lines link geothermometric temperatures that should be disregarded for the corresponding samples (see text for explanation).

To estimate the minimum depth at which the thermal waters equilibrated with their wall rocks ($z_{eq,min}$), we used the Na/K temperature for the inland samples and the unmixed quartz temperatures for the coastal–submarine samples (T_{Geot} , Table 3.1 and Table S3.4) in combination with Eq. (3.16):

$$z_{eq,min} = (T_{geot} - T_{amb}) / (\Delta T / \Delta z) \quad (3.16)$$

where T_{amb} refers to the average ambient temperature of 17 °C, and $\Delta T / \Delta z$ is the local geothermal gradient (between 12 and 25 °C km⁻¹, according to the site of the spring; Figure 3.5). The resulting minimum water–rock equilibration depths taking into account the geothermal gradient error (± 0.88 – 0.98 °C km⁻¹) are 4.5–8.6 to 5.5–10.6 km (Table S3.4). Figure 3.7 demonstrates that the coastal–submarine samples in the northwest (with discharge temperatures > 60 °C) have the highest minimum equilibration depths (5.8–8.6 to 7.1–10.6 km), whereas the cooler inland samples in the southeast (with discharge temperatures < 50 °C) have the lowest minimum equilibration depths (4.5–5.4 to 5.5–6.7 km).

It should be noted that choosing the quartz temperature to estimate the equilibration depth of the coastal–submarine samples is arbitrary. Studies of scaling in relatively fast-flowing geothermal wells have shown that owing to kinetic limitations, quartz only forms at temperatures >180 °C while chalcedony may form down to a temperature of about 110 °C (Amorsson, 1975). However, when the water upflow rate and the reactive fracture surface area are low, such as in long-lived active geothermal systems, quartz can also form at <100 °C (White et al., 1956; Rimstidt & Barnes, 1980). Due to the lack of deep samples, we do not know which silica phase controls the SiO₂ concentrations measured in the sampled thermal waters. Consequently, the equilibration depth listed for the coastal–submarine samples (Table S3.4) could be up to 1 km less (the equilibration temperature of chalcedony is about 25 °C less for the same SiO₂ concentration).

3.4. Discussion

A conceptual model of the amagmatic orogenic geothermal systems along the ABF, consistent with all geological, geochemical, and geophysical data presented above, is illustrated in Figure 3.7. The infiltration of meteoric water from high topographic elevations into the deep brittle crust via the ABF is driven by the potential energy inherent in the rugged, regional topography and facilitated by a fracture network that is sufficiently permeable for advective fluid flow. Variations in permeability and hydraulic head gradients lead to variable water penetration depths, water equilibration temperatures, residence times, and water upflow velocities. Consequently, there is a large range in temperatures (37–102 °C) of discharges in topographic lows where the local hydraulic head gradients are highest. Additionally, the chemical composition of meteoric water changes along its flow path due to long water residence times and mixing with ancient seawater-like porewater, as well as mineral precipitation and dissolution. In the coastal systems, mixing with fresh seawater also occurs. Further details on all these processes are discussed in the following sections.

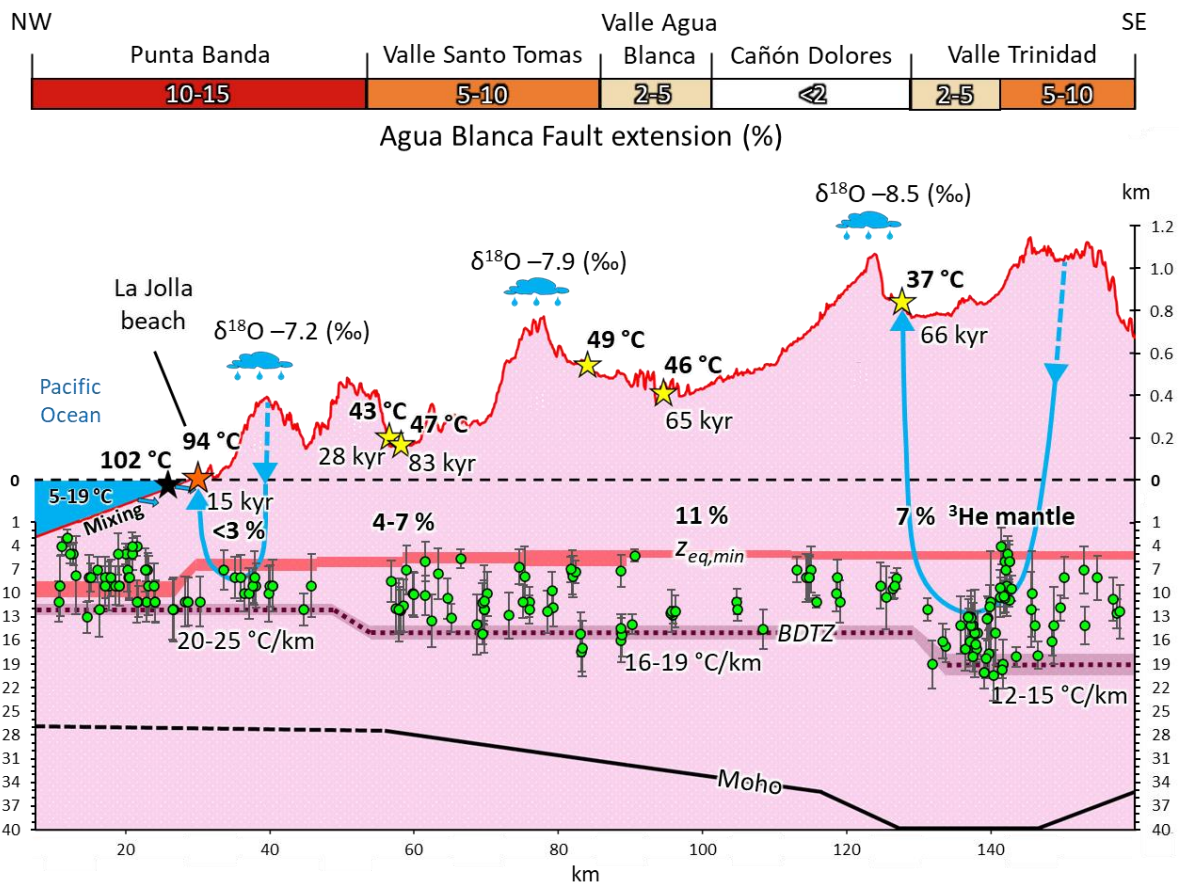


Figure 3.7. Conceptual model illustrating amagmatic geothermal systems hosted by the Agua Blanca Fault (stars) projected into a NW–SE long section along the main fault trace (red line). Note differences between the horizontal scale and the two-part vertical scale. Colored bands at the top indicate extension as a fraction of total displacement (%) along five geographic segments of the fault system (Wetmore et al., 2019). Discharge temperatures (°C), residence times (kyr), and $^3\text{He}/\text{He}_{\text{total}}$ ratios (%) correlate with degree of fault extension and with hydraulic head gradient (see text). Green circles denote locations of recent seismic events (Frez et al., 2004; RESNOM, 2017). Red band ($z_{eq,min}$) represents the depth and temperature at which ascending water departs from chemical equilibrium with its wall rocks. Purple dotted line shows depth of brittle–ductile transition zone (BDTZ), labelled with corresponding geothermal gradients. Black line represents depth of Moho (Reyes et al., 2001). Long blue arrows illustrate schematic paths of meteoric water recharging from outside the fault (dashed, projected), descending through the brittle fault plane (deeper in the SE than in the NW; see text) and then rising to the springs.

3.4.1. Evolution of chemical composition along the meteoric water flow path

The chlorine concentration in the infiltrated meteoric water along the ABF has increased from its typical original value of $<2 \text{ mg L}^{-1}$ (Junge & Werby, 1958) to $100\text{--}360 \text{ mg L}^{-1}$ in the inland thermal springs and to $4700\text{--}11000 \text{ mg L}^{-1}$ in the coastal–submarine springs. Water–rock interaction along flow paths is known to increase the concentrations of solutes in infiltrating meteoric water (López & Smith, 1995). Additionally, sea spray may elevate chloride concentrations in meteoric water in the coastal zone and up to 20 km inland (Tsunogai, 1975).

Possible sources of Cl can be constrained by examining the Cl/Br concentration ratios in the spring waters. Along the ABF the Cl/Br mass ratios are 273–338, close to that of seawater in the study area (280). The inland recharge areas are too far from the coast to be affected by sea spray, but pore spaces in the deep host rocks of the ABF likely contain fossil seawater. Thus, during the migration of meteoric water along fracture networks in the fault system, Cl and Br, and likely also some Na, Mg, SO_4 , and Li, are assumed to have been acquired by diffusive or advective mixing with seawater-like porewater (e.g., Waber & Smellie, 2008; Waber et al., 2017). Hence, the Cl concentration in the thermal waters depends on their effective cumulative water/rock ratios, which in turn are a function of residence time, path length, porewater chlorinity, volume of

accessible pore spaces, and surface area of fractures that allow exchange between the circulating meteoric water and the rock matrix. During upflow of the heated meteoric water in the coastal area, shallow mixing with modern seawater occurs. Assuming that the chlorinity of the deep waters in the coastal zone was originally similar to that of the inland thermal waters ($\sim 300 \text{ mg L}^{-1}$, Table 3.1), binary mixing calculations yield approximately 25–57% modern seawater in the coastal springs.

Other chemical processes that increase the concentration of solutes are mineral dissolution and precipitation reactions along the water flow path, which increase the concentrations of SiO_2 , B, F, and Ca. For example, the SiO_2 concentration is typically controlled by the solubility of either quartz or chalcedony (Fournier & Potter, 1982; Olguín-Martínez et al., 2022). On the other hand, B and F enrichments are caused by the dissolution of silicate minerals such as biotite, muscovite, and tourmaline (Seelig & Bucher, 2010), and Ca concentrations are controlled by plagioclase weathering and dissolution or by precipitation of secondary calcite (Seyfried & Bischoff, 1979). Finally, the admixture of Mg by seawater in the coastal–submarine thermal waters leads to the precipitation of Mg-bearing sheet silicates (Stober & Bucher, 1999), causing the observed depletion of Mg in the fluid (Figure 3.3c).

3.4.2. Infiltration of meteoric water and hydraulic head gradients

Stable isotopes of water are fractionated during condensation from cloud vapor. As a result, $\delta^{18}\text{O}$ and $\delta^2\text{H}$ values in rainfall vary in response to effects such as latitude, elevation, distance from the coast, precipitation rate, condensation temperature, and relative humidity (Dansgaard, 1964). In the study area, there is a notably higher precipitation rate in the mountainous areas (385–1050 mm yr^{-1}) than in the valleys or in the coastal zone (275 mm yr^{-1} ; CICESE, 2019), and average temperatures fall from 17 °C at the coast to approximately 10 °C at 1000 m a.s.l. Thus, $\delta^{18}\text{O}$ values in local surface-water decrease by -0.25‰ per 100 m elevation increase (blue line in Figure 3.8a; Kretzschmar & Frommen, 2013).

The analyzed inland and unmixed coastal–submarine thermal waters show no systematic shift in $\delta^{18}\text{O}$ from the GMWL and have the same stable isotopic signature as current rainfall (Figure 3.3f). Therefore, the thermal waters must have originally infiltrated as meteoric water at similar climatic conditions in the geological past. This suggests that the variation of $\delta^{18}\text{O}$ and $\delta^2\text{H}$

values of the thermal waters mainly reflects differences in recharge elevation. A first approximation of their mean water recharge elevations can be deduced directly from their $\delta^{18}\text{O}$ values (Figure 3.8a). Thus, all the thermal waters are seen to have infiltrated at mean elevations of 760–1300 m a.s.l, which are significantly higher than their discharge sites (-30 to 734 m a.s.l). The corresponding mean hydraulic-head differences (Δh) induced by the topographic relief vary within only a small range of ~570 m to 790 m.

Topographic contours corresponding to the mean meteoric recharge elevations in Figure 3.8a are shown as colored dots in Figure 3.8b, thereby identifying the recharge catchment for each thermal spring. This shows that meteoric water in the geothermal systems primarily derives from the mountainous landscape to the north of the ABF. Rainwater that has fallen over the catchment areas and infiltrated into the subsurface presumably flows through deep-reaching fracture networks towards the south, where it is captured by the permeable ABF. For the various color-coded geothermal systems, the mean distance (Δx) between the mean meteoric water recharge elevations and the thermal water discharge sites varies from 9 to 23 km (Table S3.5; Supplementary Material: Recharge_discharge_distances.xlsx). Taking into account the hydraulic-head differences (Δh) between mean recharge and discharge sites, these distances result in mean hydraulic head gradients ($\Delta h/\Delta x$) of 0.025–0.078. Note that the light green dots in the NW catchment of Figure 3.8b were omitted in these calculations owing to the great distance from the LJB and SMF springs. Recharge for those springs likely derives from the high topography (≤ 1000 m a.s.l.) on the immediately adjacent Punta Banda Peninsula (yellow dots).

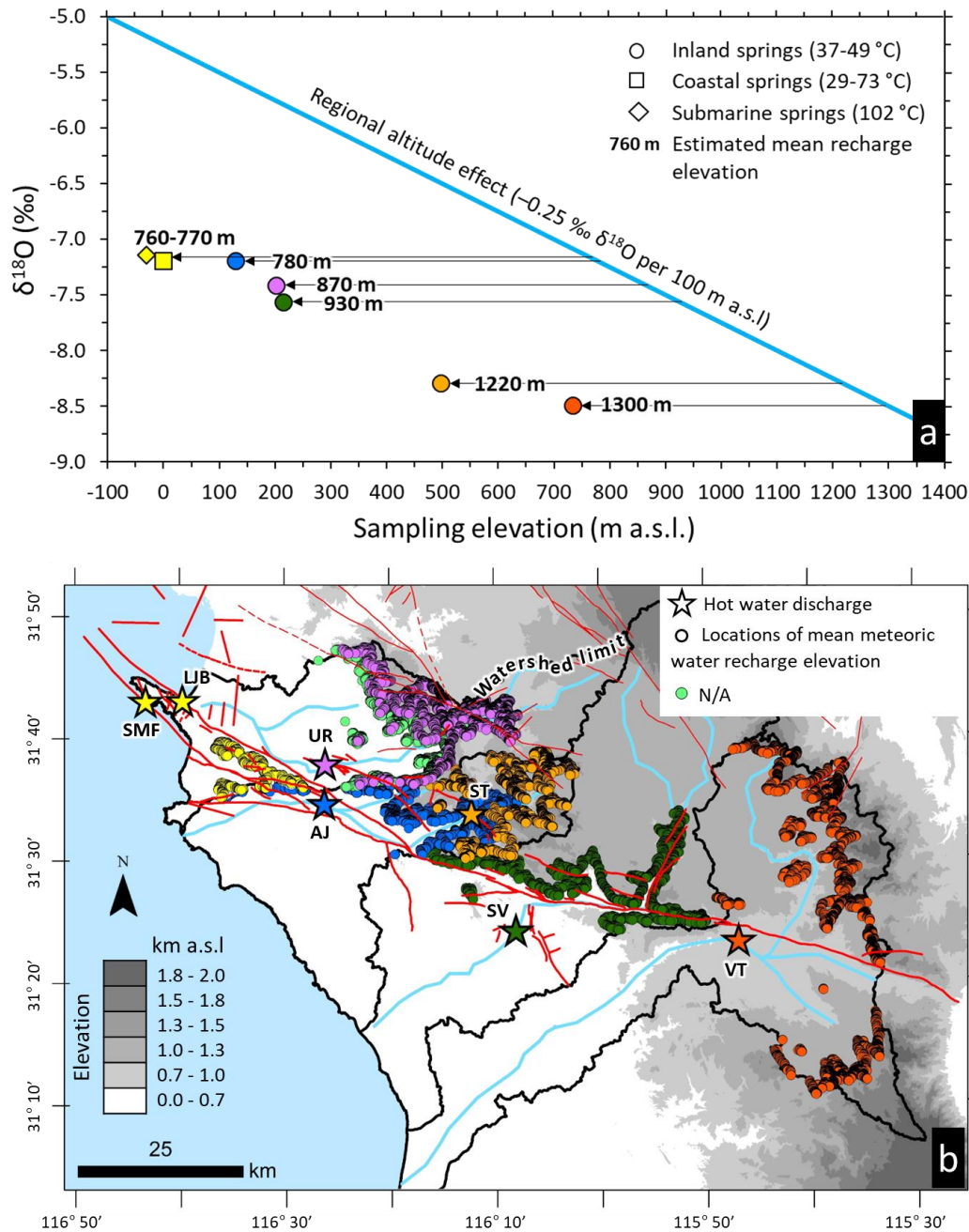


Figure 3.8. Mean elevation and catchments of meteoric water recharge of geothermal systems along the ABF. (a) Negative correlation between $\delta^{18}\text{O}$ values of thermal waters and their sampling elevation compared to that of $\delta^{18}\text{O}$ in modern surface meteoric water in northern Baja California (blue line; Kretzschmar & Frommen, 2013). The inferred recharge elevation of each thermal water sample is indicated by a labelled arrow. (b) Topographic map of the study area (after INEGI, 2022) displaying thermal water discharge locations (stars) and elevation contours

corresponding to mean meteoric water recharge elevations in the watershed of each spring (color-coded dots). Perimeters of watersheds (black lines) and rivers (blue lines) dissected by the ABF are also shown. Light green dots (N/A) mark mean water recharge elevations that were excluded from the hydraulic head gradient calculations for springs LJB and SMF (see text).

3.4.3. Controls on the hydraulic and thermal behavior of amagmatic geothermal systems

Our study reveals that the hydraulic and thermal behavior of amagmatic orogenic geothermal systems along the ABF is primarily controlled by two main parameters: the permeability of the hydraulically active fault zone and the hydraulic head gradient generated by the rugged topography to the north of the fault. Assuming that the rate of meteoric precipitation does not limit deep fluid circulation, which is a prerequisite for deep, single-pass fluid circulation ([Alt-Epping et al., 2021](#)), then these two parameters determine all key features of the flow system. This includes the locations and temperatures of hot springs at the surface, the rate of water upflow, the depth of meteoric water penetration, the temperature and depth of water–rock equilibration, the subsurface water residence times, and probably also the $^3\text{He}/\text{He}_{\text{total}}$ fractions.

The importance of permeability in controlling the flow systems is manifested by the observation that all thermal waters discharge within the highly fractured and hence permeable ABF system (Figure 3.2a). Discharge sites are located at low elevations, such as valley floors or along the coast, highlighting the role of the hydraulic head gradient in controlling the location of the discharge sites. However, plotting the estimated hydraulic head gradients against the unmixed discharge temperatures does not yield a clear correlation (Figure 3.9a), indicating that hydraulic head gradient does not directly control the upflow rates and discharge temperatures in the studied geothermal systems.

In contrast, there appears to be a strong correlation between permeability and discharge temperatures (Figure 3.9b). The degree of extension along the ABF, determined from geodetic data and normalized such that the lateral and heave components sum to a total of 100% of the horizontal slip vector ([Wetmore et al., 2019](#)), is used as a proxy for permeability. Higher extension of a fault creates higher fracture porosity, which can increase the permeability of the system. Figure 3.9b shows that an increase in fault extension is associated with an increase in water discharge

temperature. For instance, the Punta Banda segment located at the coast and characterized by the highest degree of extension (10–15%, Figure 3.9b) shows extremely high discharge temperatures (T_{unmixed} : 144–212 °C), suggesting the presence of highly permeable upflow zones. Together with the lack of correlation between hydraulic head gradients and discharge temperatures (Figure 3.9a), this implies that the permeability constitutes the first-order control on upflow rates and discharge temperatures and thus on the magnitudes of the resulting thermal anomalies in the surrounding rocks.

Application of general hydrogeologic principles (Zijl, 1999) to hydraulically connected fault segments predicts that meteoric water penetrates to greater depths with increasing horizontal length (Δx) between recharge and discharge sites. For instance, numerical simulations of a fault-hosted orogenic geothermal system in the Swiss Alps have shown that the length/depth ratio required for single-pass flow through a fault with isotropic permeability is about 1.1 considering realistic permeabilities and the counteractive buoyancy induced by a 25 °C km⁻¹ geothermal gradient (Alt-Epping et al., 2021). Along the ABF, mean Δx is estimated to vary between 9 and 23 km (Section 3.4.2), opening the possibility for very deep penetration. Assuming that the BDTZ serves as the ultimate depth limit for significant advective flow of meteoric water into the crust, the scope for deep penetration is greatest in the southeastern inland segment of the fault, where the BDTZ lies 15–19 km deep, compared to the northwestern coastal segment where the BDT is only 12 km deep (Figure 3.7). Accordingly, the low hydraulic head gradients ($\Delta h/\Delta x$) in the inland systems of the ABF may induce deeper penetration of meteoric water, such that it is heated to higher temperatures than in the coastal systems. However, due to the lower inferred fault permeability and geothermal gradient in the eastern segment, Darcy's Law predicts that the rate of water upflow must be slower too. As water–rock reaction rates depend on flow rate, the depth at which the ascending water departs from chemical equilibrium with the surrounding rocks is shallower in the southeast than in the coastal zones (Figure 3.9d). This explains the shallower minimum depths of penetration inferred from the equilibrium geothermometric results for the southeastern springs. Thus, while the hydraulic head gradient may not strongly impact upflow rates and discharge temperatures, it exerts significant control over the water infiltration depth and the depth of water–rock equilibration.

Previous work has proposed that the helium isotope signatures of the thermal springs can be attributed to the migration of fluids derived from the mantle through permeable faults, combined with modification of the mantle $^3\text{He}/^4\text{He}$ ratio by mixing with radiogenic helium (Polyak et al., 1991; Barry et al., 2020). The inverse correlation between the hydraulic head gradient and the $^3\text{He}/\text{He}_{\text{total}}$ ratio observed in the present study (Figure 3.9c) suggests that longer and deeper water flow paths enable greater acquisition of ^3He . Moreover, the deeper and more extensive water infiltration along the eastern ABF is consistent with the longer estimated water residence times (Figure 3.9e). Analyzing the variation of recharge elevation and the lack of correlation between residence time and geographic location along the inland portion of the ABF, it becomes evident that there are multiple isolated flow compartments. This suggests the presence of low permeability zones along the ABF, which hinder connection between adjacent flow compartments. The existence of these low permeability zones further confirms the strong influence of local permeability on flow rates.

The observed inverse relationship between discharge temperature and inferred minimum infiltration depth (Figure 3.9f) demonstrates that ultradeep advective infiltration ($\gg 10$ km), such as is feasible in the inland systems, is not a prerequisite for magmatic systems to achieve temperatures above 120 °C in the shallow subsurface. The only requirements are that the local geothermal gradient permits the water to exceed this temperature threshold at depth and that the upflow rates are high (e.g., Wanner et al., 2019). In the coastal zone, these conditions are met, with meteoric water reaching a temperature of at least 160 °C at a depth of 6 km (Figure 3.9f). Temperatures in the plume of hot water ascending to the coastal springs are probably above 120 °C at <2 km depth.

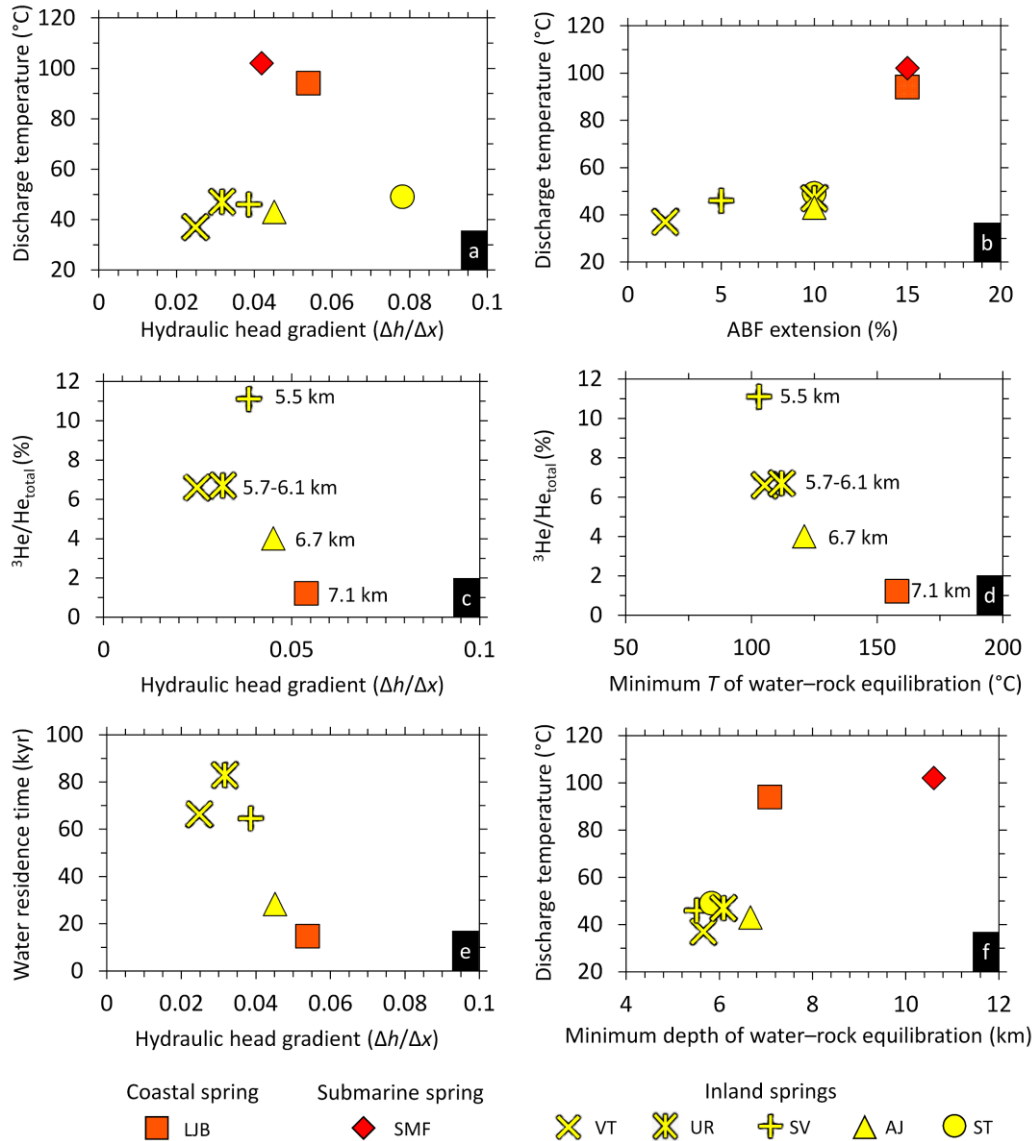


Figure 3.9. Correlations between key parameters characterizing the flow systems of the amagmatic geothermal systems along the Agua Blanca Fault. a) Discharge temperature vs. hydraulic head gradient, revealing no significant correlation. The plotted discharge temperatures have been adjusted to account for the cooling influence of recent seawater admixture (Table S3.3). b) Discharge temperature vs. ABF extension (proxy of permeability), demonstrating a strong positive correlation between these variables. c) $^3\text{He}/\text{He}_{\text{total}}$ vs. hydraulic head gradient, with km labels indicating minimum water penetration depths based on geothermometry. d) $^3\text{He}/\text{He}_{\text{total}}$ vs minimum temperature of water–rock equilibration, with km labels indicating the corresponding minimum depths of equilibration. Plots c and d show that thermal waters with

shallower depths of water–rock equilibration and lower discharge temperatures (corresponding to lower upflow rates) exhibit higher ^3He fractions. e) Water residence time vs. hydraulic head gradient, illustrating strong control of hydraulic head gradient on residence time. The plotted water residence times are estimated assuming a porosity of 1%. (f) Discharge temperature vs. minimum depth of water–rock equilibration, showing a negative correlation.

3.5. Summary and conclusions

We have investigated the behavior of amagmatic orogenic geothermal systems along the ABF in Baja California using a multidisciplinary approach encompassing geochemical, geophysical, and geological data. Our findings, consistent with similar orogenic faults worldwide, demonstrate that these systems arise from gravity-driven infiltration of meteoric water that is precipitating on the rugged hinterland of the fault. During its penetration deep into the brittle fault plane, the meteoric water increases its temperature along the local geothermal gradient while acquiring salinity and helium due to interactions with the wall rocks and with saline porewater along its flow path. Our data provide strong evidence that the flow characteristics of these systems, including water upflow rates, discharge temperatures, temperature and depth of water-rock equilibration, water residence times, and $^3\text{He}/\text{He}_{\text{total}}$ fractions, are primarily controlled by the variability of the hydraulic head gradient and the permeability of the ABF. The hottest spring waters (up to 102 °C), which have the fastest flow rates, discharge on the Pacific coast where fault extension is highest (10–15%) and hence permeability is highest. The hydraulic head gradient plays a key role in determining water flow pathways, including the depth of infiltration, water residence times, and $^3\text{He}/\text{He}_{\text{total}}$ fractions.

Our results demonstrate that, under favorable conditions characterized by high fault permeability and high hydraulic head gradients, the temperature threshold for electricity production (~120 °C) in amagmatic geothermal systems can be reached at relatively shallow depths (< 4 km), thus establishing their potential for petrothermal power production. Based on our findings, future exploration for orogenic geothermal systems should prioritize valley floors intersected by active regional faults, as these locations tend to exhibit maximum values of hydraulic head gradients and upflow rates. By focusing on these areas, we can enhance our understanding of these complex systems and unlock their potential for sustainable energy production. Overall, our study sheds light on the dynamics and controls of amagmatic orogenic

geothermal systems, providing insights for both scientific research and practical applications in the field of geothermal energy exploration and development.

Acknowledgments

This work was supported by a CONACYT project PN-2016-01-1998 to Loïc Peiffer, by a Swiss Government Excellence Scholarship (ESKAS) to Daniel Carbajal-Martínez, and by funds from the University of Bern, Switzerland. We are grateful to Luis Delgado (CICESE) for helping with rock sampling. We are also grateful to the Istituto Nazionale di Geofisica e Vulcanologia—Palermo (INGV-PA) for the analytical support and to Thomas Pettke (Univ. Bern) for help with LA-ICP-MS analysis.

Supplementary data

All the geological, geochemical and geophysical data on which this research is based are publicly available at the Zenodo repository (<https://doi.org/10.5281/zenodo.8160873>).

4. La Jolla Beach amagmatic geothermal system, Baja California, Mexico: controls on the thermal anomaly from 3D thermal–hydraulic simulations

Daniel Carbajal-Martínez¹, Christoph Wanner¹, Larryn W. Diamond¹, Loïc Peiffer^{2,3}

¹ Rock–Water Interaction Group, Institute of Geological Sciences, University of Bern, Switzerland

² Departamento de Geología, CICESE, Ensenada, Baja California, Mexico

³ Unidad La Paz, CICESE, La Paz, Baja California Sur, Mexico

Extended Abstract submitted to *World Geothermal Congress 2023*.

Abstract

Amagmatic geothermal systems that discharge in coastal areas are promising renewable energy resources for seawater desalination and electricity production. These systems arise from the deep circulation of meteoric water and seawater along regional fault zones in uplifted orogenic belts. They are characterized by diffuse hot water discharge (<100 °C) in the intertidal zone at low tide. In order to assess their energy potential, more fundamental insights are needed to understand the coupled thermal–hydraulic–chemical–mechanical processes controlling their behavior. In this contribution, we present large-scale 3D thermal–hydraulic numerical simulations of the amagmatic geothermal system at La Jolla Beach (Pacific coast), which is linked to the steeply dipping dextral Agua Blanca Fault (ABF) that traverses northern Baja California, Mexico. With a temperature of up to 94 °C, the discharge of hot water at La Jolla Beach represents the inland hottest manifestation of amagmatic geothermal systems worldwide. Simulations were run for a large 3D domain of 20 × 10 × 14 km using the software TOUGHREACT. The aims were to (i) assess the role of surface topography and nearshore seafloor bathymetry in controlling regional water circulation through the ABF and (ii) obtain a fundamental understanding of the processes causing the very high discharge temperatures at La Jolla Beach. All simulations were run by specifying hydrostatic pressure and conductive temperature distributions as initial and boundary conditions. The simulations were constrained by field observations such as discharge temperatures

(up to 94 °C), the extent of the La Jolla Beach thermal anomaly ($\sim 300 \times 100$ m), water residence times (15 ka), and seawater mixing fraction (20%). Different fault widths and permeability configurations were tested. Modeling results indicate that fluid flow within the ABF is controlled by the surface topography and, more importantly, by the hydrostatic pressure defined by the Pacific Ocean and its salinity. These boundary conditions lead to fluid upflow beneath La Jolla Beach, which occurs independently of the permeability and width of the ABF. However, assuming a homogeneous permeability along the ABF (100 m wide zone with $k = 1.5 \times 10^{-14} \text{ m}^2$) produces an extreme and unrealistically shallow geothermal anomaly of ~ 0.35 km width \times 3.3 km length with temperatures below 100 °C. However, the field observations can be reproduced by inserting a vertical 100×100 m zone with high permeability ($k = 10^{-13} \text{ m}^2$) into the model below La Jolla Beach along the ABF ($k = 8.0 \times 10^{-15} \text{ m}^2$). This preferential upflow zone controls the shape and magnitude of the resulting shallow thermal anomaly. Our observations suggest that the highest fluxes and temperatures in amagmatic, orogenic geothermal systems occur where strong hydraulic head gradients, such as the coastline or below major valley floors, coincide with highly permeable pathways along regional faults. Therefore, geothermal exploration for amagmatic geothermal systems should focus on permeable faults that cross areas with high hydraulic head gradients.

4.1. Introduction

La Jolla Beach is a coastal amagmatic geothermal system hosted by the Agua Blanca Fault (ABF) located northwest of the Punta Banda Peninsula in Baja California, Mexico (Figure 4.1). Evidence of this system is the thermal water that emanates diffusely from the intertidal zone and is visible only at low tide. Using Thermal InfraRed images acquired by drone, [Carbajal-Martínez et al. \(2020\)](#) showed that the surface temperature at La Jolla Beach is up to 52 °C, while at 20 cm below the surface, the temperature is up to 94 °C. In addition, they estimated that the footprint of the thermal anomaly is $\sim 300 \times 100$ m. Owing to its location and high temperature, this hydrothermal system is considered a valuable geothermal resource that could supply the energy demand of a multi-effect distillation plant (MED) to desalinate seawater and cover the shortage of fresh water in the region. The desalination costs of a MED are comparable to those of a reverse osmosis plant powered by fossil fuels. (0.8 US\$ m^{-3} ; [Wendt, 2017](#)).

To take full advantage of this geothermal resource, it is necessary to understand the fundamental processes controlling its behavior. In this contribution, we present large-scale 3D thermal–hydraulic numerical simulations of the amagmatic geothermal system at La Jolla Beach to (i) assess the role of surface topography and nearshore seafloor bathymetry in controlling regional water circulation through the ABF, and (ii) obtain a fundamental understanding of the processes causing the very high discharge temperatures. Our simulations are constrained by field observations such as surface location and temperature, size of the thermal anomaly, and seawater mixing fractions.

4.1.1. Structural and geothermal features of the study area

Punta Banda Peninsula has an optimal structural setting for the formation of amagmatic geothermal systems due to the lack of magmatic activity since the Miocene and to the high degree of extension of normal faults in the center of the Peninsula (orientation \sim N37°W and dips from 45° to 70°SW; [Gutiérrez-Gutiérrez & Suárez-Vidal, 1988](#)). Owing to the active dextral branches of the ABF on each side of the Punta Banda Peninsula (Figure 4.1), this area shows the greatest extension along the entire length (\sim 150 km) of the ABF trace ([Wetmore et al., 2019](#)). Uplift rates are also high, with 12 marine terraces having been uplifted over the past 1.3 Ma (Figure 4.1B; [Rockwell et al., 1989](#)). These terraces geographically coincide with amagmatic geothermal systems as evidenced by the discharge of thermal waters at three distinct locations across the Punta Banda Peninsula (Figure 4.1B). These locations are El Retiro Beach with a discharge temperature of 35 °C, a fumarolic submarine field on the southeastern side of the Peninsula (102 °C), and La Jolla Beach (94 °C; [Vidal et al., 1981](#); [Carbajal-Martinez, 2019](#); [Carbajal-Martínez et al., 2020](#)).

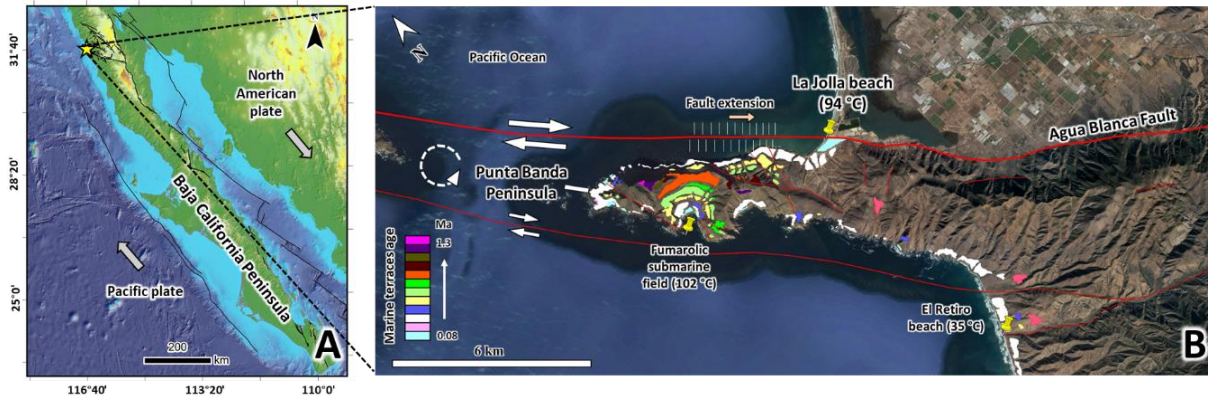


Figure 4.1. A) Location of the study area. B) Structural setting and location of amagmatic geothermal systems of the Punta Banda Peninsula, Baja California, Mexico.

La Jolla Beach is the focus of our study. It is worth mentioning that 500 m around the coastal anomaly, there are shallow domestic wells that record temperatures between 29 and 73 °C (Figure 4.2). Additionally, [Arango-Galván et al. \(2011\)](#) and [Carbajal-Martinez, \(2019\)](#) reported the distribution of rock resistivity in four electrical resistivity tomography sections (up to 80 m depth, Figure 4.2). These sections reveal the presence of a conductive anomaly ($0.8 \Omega \text{ m}$) beneath the coastal thermal anomaly of La Jolla, implying the presence of thermal and saline waters in the subsurface.

The chemical composition of the thermal waters discharging at La Jolla Beach, including their dissolved gas concentrations, is described in detail by [Carbajal-Martínez et al. \(2023\)](#). In short, the thermal waters are characterized by a slightly acidic pH (5 to 7) and a lower salinity (8.5 to 16 g L^{-1}) than local seawater (8.0 and 34.0 g L^{-1} , respectively). The isotopic values of $\delta^{18}\text{O}$ and $\delta^2\text{H}$ reveal that thermal water originates from rainwater recharged in the mountainous zone and mixed with seawater in the coastal zone. In addition, the ^3He fraction within the dissolved He is less than 3%, implying that the contribution of He from the mantle is negligible and confirms the amagmatic nature of the hydrothermal system.

The design of our numerical simulations is based on the following conceptual model of geothermal activity in the study area ([Carbajal-Martínez et al., 2023](#)). Meteoric water recharges in the inland mountains (Figure 4.1B) and is driven by topographically controlled head gradients through the crystalline basement and may reach down to the brittle–ductile transition zone (12 km), the lower limit for advective fluid flow. The temperature of the meteoric water increases

during infiltration according to the average geothermal gradient of $24\text{ }^{\circ}\text{C km}^{-1}$. Beneath La Jolla Beach, the heated water quickly ascends towards the surface through a highly permeable section of the ABF and finally discharges as a thermal spring. Along its flow path, the infiltrated meteoric water mixes with seawater-like ancient porewater, and near the coast, with fresh seawater.

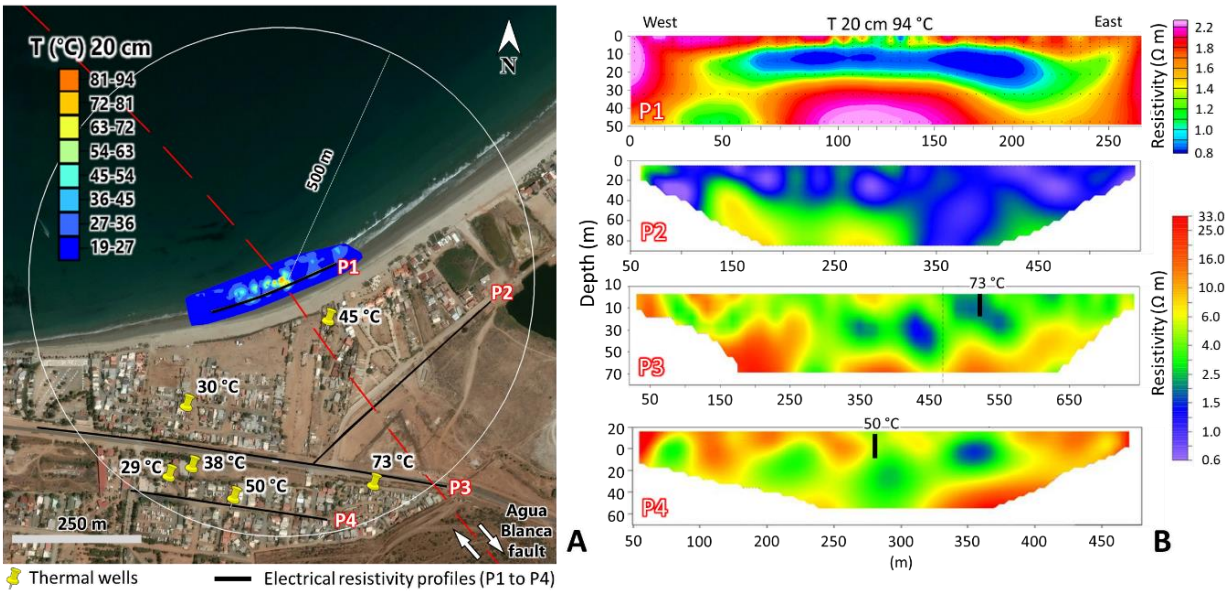


Figure 4.2. A) Temperature and size of the La Jolla Beach thermal anomaly (Carbajal-Martínez et al., 2020) as well the location of six surrounding domestic wells (yellow markers) and four electrical resistivity tomography profiles (black lines P1 to P4). B) Electrical resistivity tomography sections for the four profiles shown in A (Carbajal-Martínez, 2019). The vertical black lines in sections P3 and P4 illustrate the location and depth of domestic wells.

4.2. Numerical simulator

Our forward coupled thermal–hydraulic numerical simulations were performed using the integral finite difference code TOUGHREACT V3 (Xu et al., 2014). All simulations were performed using the equation of state EOS1, allowing the simulation of pure water in its liquid, vapor, and two-phase states (Pruess et al., 1999). The temperature dependence of pure water properties such as viscosity, specific density, and enthalpy are calculated from steam table equations (International Formulation Committee, 1967). EOS1 simulates water and coupled heat flow according to the mass balance equation:

$$\frac{\partial M_{W,H}}{\partial t} = -\nabla F_{W,H} + q_{W,H} \quad (4.1)$$

where $M_{W,H}$ is the accumulation term for water M_W (kg m^{-3}) or heat M_H (J m^{-3}), $F_{W,H}$ is the water flux F_W ($\text{kg m}^{-2} \text{s}^{-1}$) or heat flux F_H ($\text{J m}^{-2} \text{s}^{-1}$), and $q_{W,H}$ are water or heat sinks (-) or sources (+). For fully saturated, single-phase flow problems F_W is equal to the Darcy flux u (m s^{-1})

$$u = -\frac{k}{\mu} (\nabla P - \rho g) \quad (4.2)$$

where k is the intrinsic permeability (m^2) of the rock, μ is the water viscosity (Pa s), ∇P (Pa m^{-1}) is the hydraulic head gradient, ρ is the density of water (kg m^{-3}), and g is the acceleration due to gravity (m s^{-2}). Heat flux F_H ($\text{J m}^{-2} \text{s}^{-1}$) is defined as

$$F_H = C_M \times T \times \rho_M \times u - \lambda \times \nabla T \quad (4.3)$$

where C_M ($\text{J kg}^{-1} \text{K}^{-1}$) and ρ_M (kg m^{-3}) are the specific heat capacity and the density of the porous medium, T (K) is the temperature of the porous medium, λ is the thermal conductivity of the wet rock ($\text{J s}^{-1} \text{m}^{-1} \text{K}^{-1}$), and the gradient in temperature between adjacent grid blocks is ∇T (K m^{-1}).

4.2.1. Model geometry

Our numerical model covers a large 3D domain of $20 \times 10 \times 14$ km. The model is discretized using an initially regular rectangular mesh consisting of ca. 200,000 grid blocks. The size of the grid blocks is variable, whereas the highest resolution is in the La Jolla Beach area ($25 \times 25 \times 10$ m). The variability of block size in the X and Y directions is shown in Figure 4.3.

Our 3D model domain explicitly considers the topography (max. 1 km) and bathymetry (max. 0.5 km) of the study area (Figure 4.3A). In order to incorporate the morphology of the area, a digital elevation model (DEM) was downloaded from the National Oceanic and Atmospheric Administration ([NOAA National Geophysical Data Center, 2006](#)). Subsequently, the DEM was used to numerically shape the surface of the initial regular mesh using the "fit surface" PyTOUGH

method (Croucher, 2015). This resulted in an irregular mesh explicitly considering the topography of the Punta Banda Peninsula and the seafloor bathymetry (Figure 4.3B).

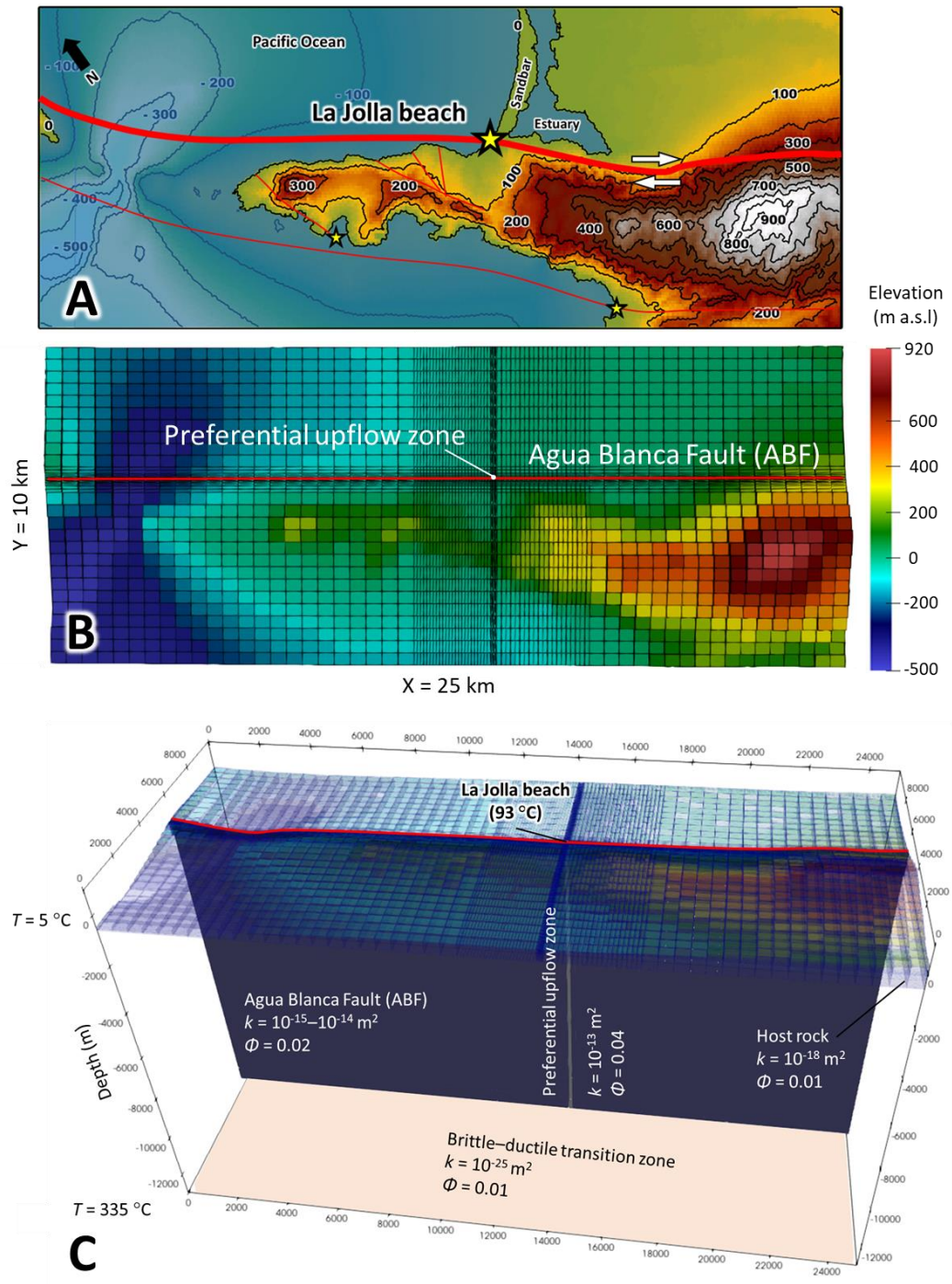


Figure 4.3. A) Topographic and bathymetric map of the model domain. B) Mesh configuration for all simulations along with the topography and bathymetry values. C) Model setup showing four domains in 3D view: Agua Blanca Fault, host rock, a preferential upflow zone beneath La Jolla Beach, and the brittle–ductile transition zone, which defines the base of the model.

4.2.2. Initial and boundary conditions

All simulations were performed by specifying the initial conditions of hydrostatic pressure and conductive temperature distributions. A fixed temperature was set at the upper boundary assuming an ambient temperature of 16 °C at the coast (CICESE, 2019), an adiabatic cooling rate of -5.5 °C km⁻¹ over the continent, and a cooling gradient of -3.1 °C per 100 m depth in the seawater column (h) (Emery & Dewar, 1982).

Over the continent, the atmospheric pressure varies according to the altitude (z ; Cavcar, 2000). Consequently, we used the following equation to define the pressure at the upper model boundary, which was fixed throughout the simulations.

$$P_{continent} = 10^5 \times [1 - (0.0065 \times z / 289.15)]^{5.2561} \quad (4.4)$$

Over the Pacific Ocean, the seafloor was defined as an upper model boundary. The pressure on this boundary was fixed by the seawater column length (h), density ($\rho_{seawater} = 1025 \text{ kg m}^{-3}$), and g , the acceleration due to gravity (m s^{-2})

$$P_{seafloor} = \rho_{seawater} \times g \times h \quad (4.5)$$

Assuming an initial conductive temperature distribution, the temperature increases with depth according to the regional geothermal gradient of 24 °C km⁻¹ (Carbajal-Martínez, 2019). At the lower model boundary (13 km below sea level), the temperature was fixed at 335 °C, according to the geothermal gradient, the mean altitude of the surface topography (0.23 km), and the mean annual temperature at sea level (16 °C). Three lateral and lower model boundaries were open for conductive heat exchange and closed for fluid flow. The upper model boundary and the lateral boundary in the direction of the Pacific Ocean were open for both heat and fluid flow.

4.2.3. Model parameters

In the study area, there are no hydraulic well test measurements that could be used to define the permeability within the model domain. Therefore, we have kept the model as simple as possible. The model was divided into four domains (Figure 4.3C): host rock, fault zone, preferential upflow zone, and brittle–ductile transition. We assume a homogeneous permeability distribution for the host rock (granite) and fault zone, and we ignored any depth dependence of the permeability and porosity. Host rock and fault permeability values were taken from other studies in a similar geologic and tectonic setting (Table 4.1; [Alt-Epping et al., 2021](#); [Wanner et al., 2019](#)).

For the host rock, we use a permeability of 10^{-18} m^2 and a porosity of 1% for all numerical simulations. Fault permeability ranges from 8×10^{-15} to $1.5 \times 10^{-14} \text{ m}^2$ according to different fault widths (25, 50, 75, 100 m), and porosity is 2%. For the brittle–ductile transition (model base), we use a low permeability (10^{-25} m^2) and a porosity of 1%. On the other hand, additional simulations were performed using a 1D preferential upflow zone with a footprint of $100 \times 100 \text{ m}$ beneath La Jolla Beach. Permeability values for the preferential upflow zone are varied from 10^{-14} to 10^{-13} m^2 with a porosity fixed at 4%. We use a homogeneous distribution of the bulk rock density, thermal conductivity, and specific heat capacity in the four domains (Table 4.1).

Table 4.1

Material properties

Parameter	Fault	Preferential upflow zone	Host rock	BDT ^a
Permeability (m^2)	8×10^{-15} – 1.5×10^{-14}	10^{-14} – 10^{-13}	10^{-18}	10^{-25}
Porosity	0.02	0.04	0.01	0.01
Bulk rock density (kg m^{-3})	2660	2660	2660	2660
Thermal conductivity ($\text{W m}^{-1} \text{K}^{-1}$)	3.35	3.35	3.35	3.35
Specific heat capacity ($\text{J kg}^{-1} \text{K}^{-1}$)	920	920	920	920

^a Brittle–ductile transition

4.3. Results and discussion

4.3.1. Location of the upflow zone

The results of the 3D thermal–hydraulic simulations without any preferential upflow zone are shown for a northwest-southeast (NW-SE) profile along the ABF (Figure 4.4A). The temperature

distribution and flow vectors demonstrate that there is a water upflow zone in the coastal area due to the infiltration of meteoric water as well as seawater into the crystalline basement along the ABF (Figure 4.4B). Darcy flux profiles illustrate that the upflow zone is always located in the coastal zone independently of the fault width and fault permeability (Fig 4.4C). The upflow zone spatially correlates with the lowest hydrostatic pressure (highest hydraulic head gradient) along the entire ABF (Figure 4.4D), demonstrating that the regional-scale hydraulic regime causes the thermal anomaly at La Jolla Beach. The precise location of the discharge zone is controlled by the balance of hydrostatic pressures between (i) the seawater column of the Pacific Ocean and (ii) the meteoric water column of the mountainous onshore zone. This is illustrated in detail in Figure 4.4E, showing the result of three simulations with a different implementation of the fixed pressure (Eq. 4.7) at the seawater model boundary: (i) no seawater present (i.e., $P_{fixed} = 1$ bar), (ii) seawater with a density of pure water ($\rho_{seawater}$: 997 kg m^{-3}), (iii) seawater with a correct density of 1025 kg m^{-3} . The thermal anomaly and thus the upflow zone occur below La Jolla Beach only when the correct seawater density is used to specify the seawater model boundary (simulation (iii)). In simulations (i) and (ii), in contrast, the upflow zone occurs 11 and 2 km offshore from the coastline.

The results shown in Figure 4.4C thus demonstrate that the hydrostatic pressure of the Pacific Ocean plays a key role in controlling the location of the thermal anomaly, while the permeability of the fault controls the discharge temperature of thermal waters. It should be noted, however, that the resulting water upflow (Figure 4.4B) generates a rather large coastal geothermal anomaly with a length of ~ 4 km along the ABF when the fault width and permeability are calibrated to 100 m and $k = 1.5 \times 10^{-14} \text{ m}^2$ in order to match the $94 \text{ }^\circ\text{C}$ surface temperature observed at La Jolla Beach. Although we have little information on the extent of the subsurface anomaly, the one obtained from the calibrated simulation appears to be unrealistically large, implying that not all relevant processes are captured by the model.

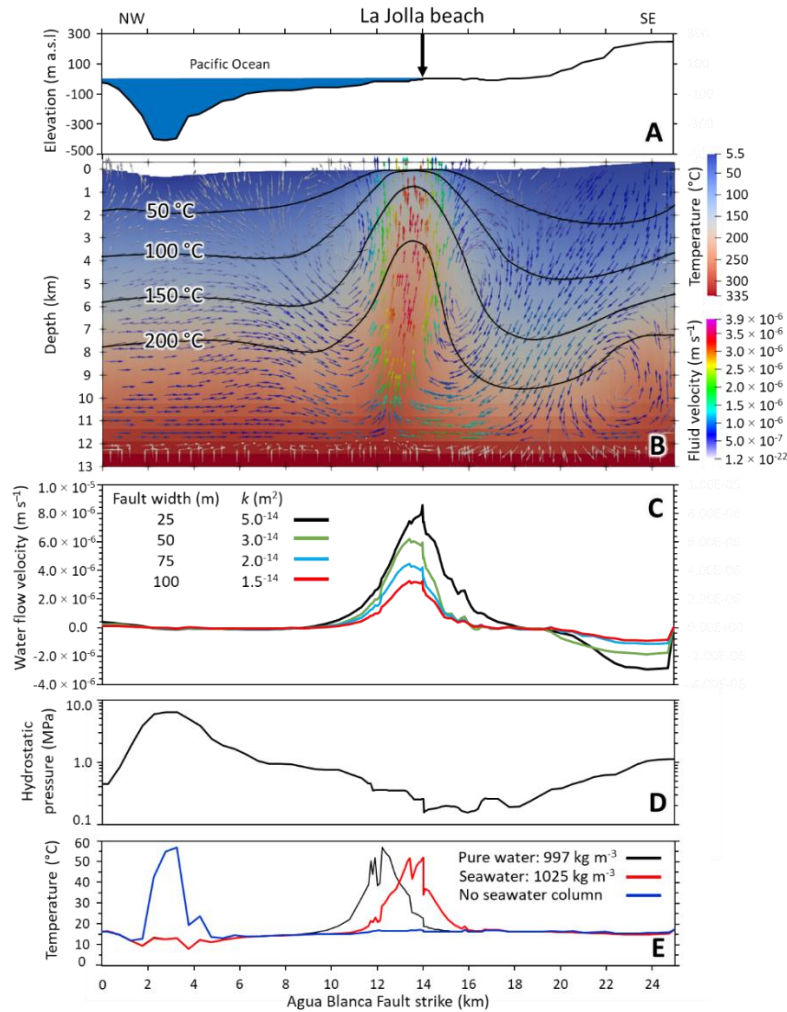


Figure 4.4. Results of numerical thermal–hydraulic simulations using a homogeneous permeability along the ABF, shown in profiles along the NW–SE strike of the fault. Plotted values of Darcy flow, hydrostatic pressure, and temperature correspond to a depth of 15 m below the surface and seafloor. A) Topographic and bathymetric profile. B) Temperature (°C) and flow velocity vectors (m s⁻¹) show that the length of the near-surface thermal anomaly is extreme (~4 km) for a fault width of 100 m and fault permeability of 1.5×10^{-14} m². C) Water flow velocity vector of the z component (m s⁻¹) along the ABF showing that the maximum flux occurs in the coastal zone independently of the chosen fault width and permeability. D) Hydrostatic pressure (MPa) along the ABF shows that the lowest hydrostatic pressure is located in the coastal zone. E) Temperature distribution (°C) of three simulations involving a 100 m wide fault and a permeability of 1.5×10^{-14} m² but with different implementations of the seawater boundary.

4.3.2. Effects of preferential upflow zones

Previous studies agree that along regional faults there are preferential pathways for fluid circulation, in which permeability is enhanced by complex structural features such as dilational jogs, linkage and intersection zones between fault segments, and highly fractured damage zones. (e.g., [Caine et al., 1996](#); [Faulkner et al., 2010](#)). In the study area, the structural setting is complex (see Section 4.1.1), and field evidence (marine terraces and normal fault displacements) indicate that near La Jolla Beach there may be enhanced permeability due to the large extensional component of the ABF. For this reason, and because of the large size of the thermal anomaly that results from simulations assuming a homogeneous fault zone permeability (Figure 4.4B), we decided to perform additional numerical simulations incorporating a vertical 1D pathway representing a preferential upflow with a footprint of 100×100 m. Table 4.1 shows the results of testing different permeability values for this pathway.

Simulations involving a fault zone 100 m wide ($k = 8.0 \times 10^{-15} \text{ m}^2$) and a preferential upflow zone with 4% porosity result in heated water reaching the surface at $30 \text{ }^\circ\text{C}$ as soon as the permeability of the preferential pathway is greater than $6 \times 10^{-14} \text{ m}^2$ (Figure 4.5A). Once the permeability of the preferential pathway is increased to 10^{-13} m^2 , the temperature reaches $\sim 90 \text{ }^\circ\text{C}$ and thus matches the observed temperature at La Jolla Beach. Under steady state conditions, which are reached after about 15 kyr (Figure 4.5B), this simulation yields seawater and rainwater fractions of $\sim 20\%$ and 80% , respectively (Figure 4.5C). These fractions agree well with those reported by [Carbajal-Martínez et al. \(2023\)](#), demonstrating that the geothermal system is dominated by infiltration of rainwater in the mountainous hinterland, driven by the high, topographically induced hydraulic head gradients.

Implementing the permeable upflow zone in our simulations considerably decreases the length of the thermal anomaly at La Jolla Beach for the calibrated models that match the $94 \text{ }^\circ\text{C}$ discharge temperature (Figure 4.6A). When the fault zone is assigned a homogeneous permeability, the anomaly is 3.3 km long (Figure 4.6B). In contrast, when a preferential upflow path is inserted beneath La Jolla Beach, the anomaly is only 475 m long (Figure 4.6C). Assuming that the ~ 500 m length over which domestic wells are distributed near La Jolla Beach approximately captures the true extent of the thermal anomaly (Figure 4.1), the simulation incorporating a 1D permeable upflow path seems quite realistic. By implementing this preferential

pathway, we are thus able to reproduce all manifestations of the thermal anomaly, including its discharge temperature, size, location, and seawater mixing fraction.

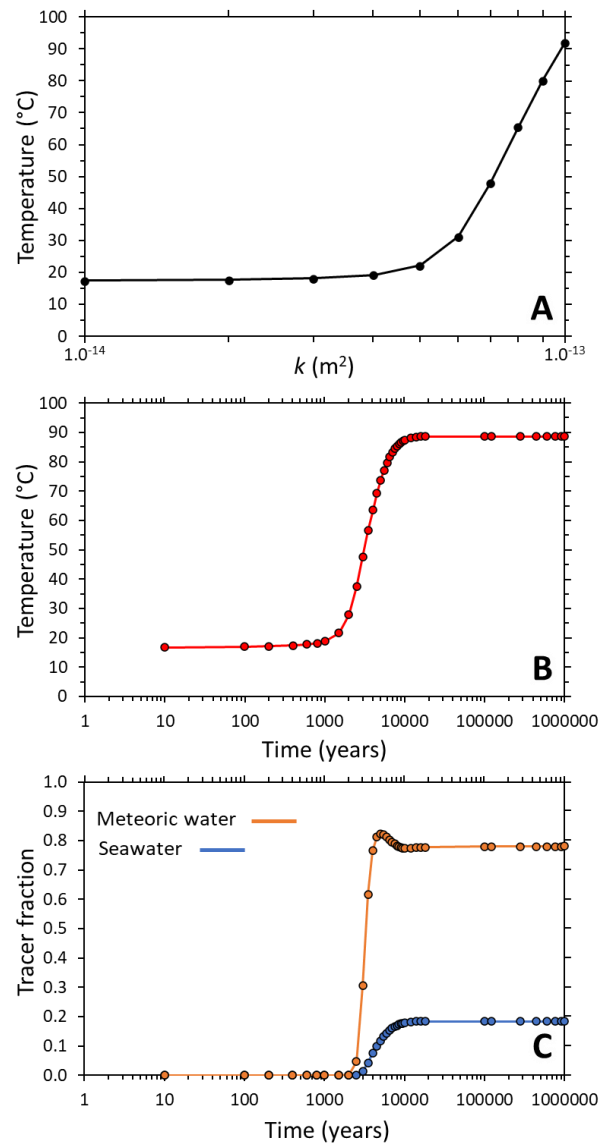


Figure 4.5. Temperature and tracer fraction (meteoric water and seawater) at 15 m below La Jolla Beach obtained by incorporating a preferential upflow zone in the simulation. A) Temperature as a function of assumed permeability (k) of the preferential upflow zone. B) Temperature vs. time, demonstrating that the simulation reaches a steady state after approximately 15 kyr. C) Tracer fraction of seawater and meteoric water as a function of time. Values shown in B and C correspond to a 100 m wide fault with a permeability of $8.0 \times 10^{-15} \text{ m}^2$ and permeability of the preferential upflow zone of 10^{-13} m^2 .

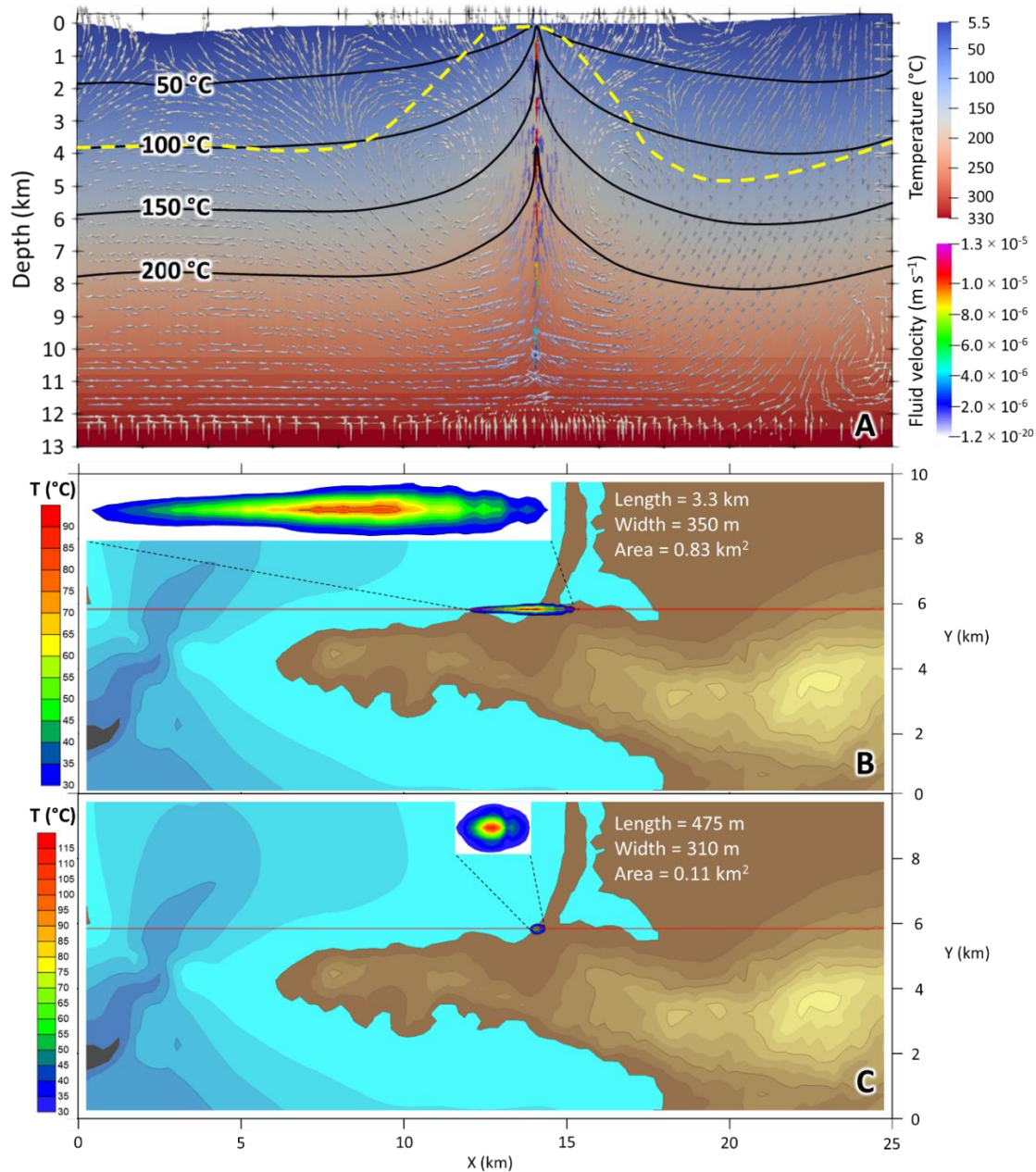


Figure 4.6. A) Depth section along the ABF showing temperature ($^{\circ}\text{C}$) and fluid velocity vectors (m s^{-1}) resulting from a simulation that includes a preferential upflow path beneath La Jolla Beach. Yellow dashed line shows the much longer thermal anomaly (100 $^{\circ}\text{C}$ isotherm) that results if the preferential upflow path is omitted from the model. B) Plan view of the thermal anomaly at 30 m depth ($T \geq 30^{\circ}\text{C}$) resulting from simulations in which the ABF has a homogeneous permeability. C) Same as panel B but with the inclusion of a preferential upflow path within the fault plane.

4.4. Conclusion

Thermal–hydraulic simulations carried out for the La Jolla Beach system in Baja California, Mexico, demonstrate that the location and temperature of amagmatic coastal geothermal systems are controlled by the balance of hydrostatic pressure forces from the Ocean and adjacent onshore areas, as well as the permeability of major fault zones where advective subsurface fluid flow occurs. Upflow zones of thermal waters are always located in the coastal zone because this is where the hydraulic pressure is minimized and where the upflow of heated water is facilitated. For the investigated case study at La Jolla Beach, however, the additional definition of a highly permeable pathway beneath the discharge location was required to accurately match all manifestations of the thermal anomaly at the surface (discharge temperature, size, and location of the thermal anomaly, and seawater mixing fraction). Our study thus suggests that the most effective amagmatic orogenic geothermal systems occur where strong hydraulic head gradients below major valley floors or at the coastline coincide with highly permeable preferentially pathways along regional faults.

4.5. Acknowledgments

Carbajal-Martínez thanks the Swiss Government Excellence Scholarship (FCS) for funding his PhD in Earth Sciences at the University of Bern.

Supplementary data

All simulation input files on which this research is based are publicly available at the Zenodo repository (<https://doi.org/10.5281/zenodo.8379019>).

5. Behavior of coastal amagmatic geothermal systems: modeling insights from La Jolla Beach, Baja California, Mexico

Daniel Carbajal-Martínez^{1,*}, Christoph Wanner¹, Larryn W. Diamond¹, Loïc Peiffer^{2,3}

¹ Rock–Water Interaction Group, Institute of Geological Sciences, University of Bern, Switzerland

² Departamento de Geología, Centro de Investigación Científica y de Educación Superior de Ensenada (CICESE), Ensenada, Baja California, México.

³ Unidad La Paz (ULP), Centro de Investigación Científica y Educación Superior de Ensenada (CICESE), La Paz, Baja California Sur, México.

In preparation for submission to a peer-reviewed journal

Abstract

In this study, we explore the thermal–hydraulic behavior of fault-hosted orogenic amagmatic geothermal systems, aiming to understand the key factors influencing their development. Our investigation delves into the impact of geological elements including topography, bathymetry, basement topography, and sediments, on the regional water circulation within the upper crust and, specifically, the Agua Blanca Fault (ABF) system. Results of 3D thermal–hydraulic simulations using TOUGHREACT reveal the functioning of the amagmatic geothermal system at La Jolla Beach, Baja California, Mexico. Our analysis highlights the crucial role of seawater as a hydraulic barrier, determining the location of coastal geothermal systems and limiting the seaward circulation of meteoric water through the fault. The higher the fault permeability, the hotter the water discharge, and the greater the infiltration of seawater through the ABF. Additionally, we find that a significant proportion of water infiltrates through the fault zone compared to the host rock, with meteoric water comprising a larger portion than seawater in the system. Furthermore, we observe variations in the behavior of the thermal anomaly at La Jolla Beach, particularly concerning its position and width. These differences are intricately linked to the topography of the crystalline basement and the distribution of sediments within the study area. The thickness of sediments plays a crucial role in governing the infiltration of seawater through the fault zone,

thereby influencing the flow of upflow thermal water towards the coastline. Coupled with the minimum pressure conditions at the coast, these factors collectively regulate the length of the shallow thermal anomaly. Our simulations successfully reproduce field observations of the thermal anomaly, including its location, extent, temperature, and salinity. In conclusion, our study provides insights into the behavior of amagmatic geothermal systems, highlighting the importance of considering topography, bathymetry, basement topography, and sediment characteristics. Understanding the influence of these key factors should aid exploration for and sustainable exploitation of such geothermal resources.

Plain Language Summary

In this research, we studied the behavior of underground geothermal systems located in fault zones without volcanic activity, aiming to understand what factors influence their formation. We focused on the geothermal system at La Jolla Beach, Baja California, Mexico. Using advanced computer simulations, we analyzed how the landscape and geological features, such as rocks and sediments, affect the movement of water and heat underground. We discovered that seawater plays a critical role in determining where these geothermal systems occur along the coast and limits the movement of fresh rainwater inland. The wider and more permeable the fault, the hotter the water that flows through it. Interestingly, most of the water that infiltrates into the system comes through the fault zone instead of the surrounding rocks. Moreover, we found that the thickness of sediments also influences the behavior of the geothermal system. Sediments act like a barrier, directing the flow of hot water towards the coast. This, along with the low-pressure conditions at the coast, controls the size of the thermal area near the beach. Our study helps us better understand these geothermal systems, which are valuable for sustainable energy production. By considering the landscape and geological factors, we can improve our exploration and use of this clean energy source.

5.1. Introduction

Amagmatic orogenic geothermal systems originate in areas that lack recent magmatic activity. In these systems, the deep infiltration of meteoric water into the continental crust is driven by the rugged topography of mountain belts, creating hydraulic heads that promote fluid flow along fracture networks. As the water infiltrates deeper into the subsurface, it transports heat from the

surrounding wall rocks. Subsequently, it ascends towards the surface and discharges into valley floors or coastal zones along regional fault zones. (López & Smith, 1995; Coussens et al., 2018; Diamond et al., 2018; Alt-Epping et al., 2022). These systems are characterized by an average geothermal gradient of less than $30\text{ }^{\circ}\text{C km}^{-1}$, reservoir temperatures reaching up to $250\text{ }^{\circ}\text{C}$, and spring temperatures of from 25 to $99\text{ }^{\circ}\text{C}$ depending on the variability of the hydraulic head gradient and the permeability of faults (Carbajal-Martínez et al., 2023).

When the host fault for geothermal circulation intersects a coastline, the discharge of thermal water from these geothermal systems becomes visible in the coastal intertidal zone during low tide. Notably, this results in the presence of prominent thermal anomalies directly at the coastline, characterized by high temperatures. The thermal water diffusively releases onto sandy beaches and rocks, creating observable thermal signatures in the immediate coastal area. These thermal anomalies can extend up to several hundred meters along the beach (Lynn, 1978). Interestingly, the salinity and pH are lower than seawater, and discharge temperatures typically vary from 30 to $100\text{ }^{\circ}\text{C}$ (Carbajal-Martínez et al., 2020). Notable examples include Hot Water Beach in New Zealand (Lyon & Giggenbach, 1992), Akropotamos coastal zone in Greece (Papachristou et al., 2021), and Gölbası coastal spring in Turkey (Gökgöz & Akdağoğlu, 2016). Along the Baja California Peninsula in Mexico, at least 12 coastal geothermal systems have been documented (Figure 5.1a; López-Sánchez et al., 2006; Camprubí et al., 2008; Hernández-Morales & Wurl, 2017; Batista Cruz et al., 2019; Carbajal-Martínez et al., 2020; Hernández-Morales et al., 2021).

Detailed insights into the thermal–hydraulic behavior of coastal geothermal systems have been obtained through two-dimensional numerical simulations conducted for the systems in Seferihisar, Turkey, and the Dead Sea in Israel (Shalev & Yechieli, 2007; Magri et al., 2012). Based on these simulations, these systems occur at intersections of fault zones, with water traveling several kilometers along the basement interface before ascending back to the shore as thermal water. However, despite these advancements, intriguing knowledge gaps regarding coastal amagmatic orogenic geothermal systems still remain. Specifically, understanding the key factors that control their locations, extent, magnitude, and salinity remains a challenge. Addressing these uncertainties is vital for enhancing exploration efforts and devising effective strategies for heat

extraction from these geothermal resources, with potential applications in areas such as seawater desalination (Karytsas et al., 2002).

In this study, we conducted large-scale 3D thermal–hydraulic numerical simulations of the amagmatic geothermal system at La Jolla Beach in Ensenada, Baja California, Mexico. La Jolla Beach was chosen as our study area due to its recognition as the hottest coastal amagmatic geothermal system known to date and its comprehensive geophysical and geochemical dataset, which allowed for the development of a well-established geothermal conceptual model (Carbajal-Martínez et al., 2020, 2023). Our simulations aimed to assess the influence of topography, bathymetry, fault zones, and sediments on the location and magnitude of coastal geothermal systems. Simulations revealed that the infiltration of meteoric water and seawater predominantly occurred through the fault zone, leading to the upflow of thermal water directly at the coastline, reproducing the field observations of La Jolla Beach. The presence of the ocean acted as a hydraulic barrier, restricting the circulation of meteoric water beyond the coast. These findings have significant implications, not only for enhancing our understanding of coastal geothermal systems on a global scale but also for the management and utilization.

5.1.1. Site description

La Jolla Beach is the hottest coastal geothermal system located in the northwest of the Baja California Peninsula (Figure 5.1a). The geothermal system is hosted by the western segment of the Agua Blanca Fault (ABF), a subvertical west–northwest-trending (276–302°) dextral–normal structure that was first active between 3.3 and 1.5 Ma (Wetmore et al., 2019). In its western portion, the ABF splits into two dextral branches that enclose the Punta Banda Peninsula (Figure 5.1b). Movements along the faults have led to the formation of 12 marine terraces in the past 1.3 Ma (Rockwell et al., 1989) and an extensional sedimentary basin, partly offshore in Bahía Todos Santos and partly onshore at Maneadero (Figure 5.1b) (Pérez-Flores et al., 2004). At La Jolla Beach the ABF exhibits its highest degree of tectonic extension along its 150 km length (Wetmore et al., 2019), which is taken to coincide with a maximum in permeability along the fault system (Carbajal Martínez et al., 2023). In addition, fault activity has resulted in the development of two other geothermal systems along the southern branch of the ABF, at El Retiro Beach (35 °C) and in a submarine fumarolic field (102 °C, Vidal et al., 1978).

The thermal water discharged at La Jolla Beach is a mixture of seawater and meteoric water and it has a neutral pH (~ 7) and a lower salinity ($8.5\text{--}16\text{ g L}^{-1}$) than local seawater (34 g L^{-1}). The thermal anomaly at La Jolla becomes visible during low tide and extends approximately 300 m in length and 100 m in width. Temperatures within the anomaly vary from 20 to 94 °C (Figure 5.1c) (Carbajal-Martínez et al., 2020). In the vicinity of the anomaly, six shallow thermal wells exhibit temperatures between 29 and 73 °C (Figure 5.1c). Furthermore, four electrical resistivity tomography sections (up to 80 m depth, Figure 5.1d) indicate the presence of a conductive anomaly ($0.8\ \Omega\text{ m}$) beneath the coastal thermal anomaly. This observation suggests the existence of thermal and saline water in the subsurface within a 500 m radius around La Jolla Beach (Arango-Galván et al., 2011; Carbajal-Martínez, 2019).

The main host rocks of the ABF are Cretaceous granitoids (Ortega-Rivera, 2003). However, the heat transported by the La Jolla Beach geothermal system is interpreted to be amagmatic, based on the absence of recent volcanic activity and on the negligible mantle contribution ($< 3\%$) to the total helium content of the thermal springs. Stable H–O isotopes of the thermal water show that it largely originates as meteoric precipitation at an elevation of approximately 800 meters a.s.l. in the orogenic mountain belt to the east of the coastline. The concentration of solutes suggests that the ascending water departs from water–rock equilibrium at a depth of ~ 6 km at a temperature of 160 °C. Along the flow path, there have been mixing processes involving ancient seawater-like porewater, as well as mineral precipitation, dissolution, and mixing with shallow fresh seawater (Carbajal-Martínez et al., 2023).

The high discharge temperatures observed at La Jolla are likely due to the elevated permeability of the ABF in the coastal zone, as deduced from the maximum in tectonic extension associated with this portion of the fault (Wetmore et al., 2018). As discussed by Carbajal-Martínez et al. (2023), the elevated permeability sets the La Jolla Beach geothermal system apart from others further east in the same fault zone. In particular, the enhanced permeability accelerates the circulation of geothermal fluids, resulting in increased upflow velocities and equilibration temperatures, as well as a shorter deep residence time beneath La Jolla compared to the other thermal springs.

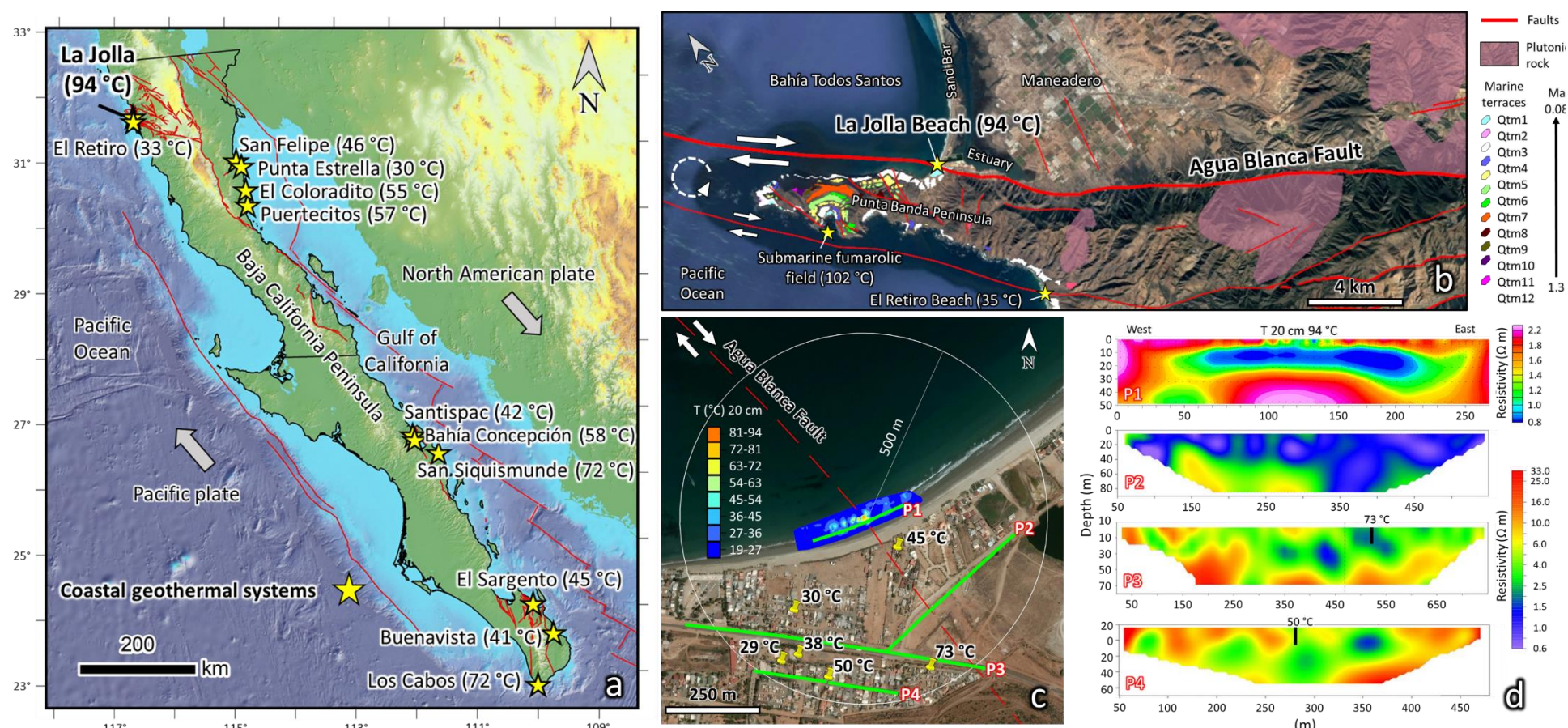


Figure 5.1. Location, structural setting, and geothermal features of the study area. (a) Location of coastal geothermal systems (yellow stars) and major faults (red) along the Baja California Peninsula in Mexico. (b) Structural setting, marine terraces (ages in Ma), and location of amagmatic geothermal systems in Punta Banda Peninsula, Baja California, Mexico. The Peninsula is flanked by two dextral branches of the Agua Blanca Fault. The main northern branch intersects the coastline at La Jolla Beach. (c) Location of the coastal geothermal systems at La Jolla Beach, showing the thermal anomaly at the beach itself (blue zone), the locations of six shallow domestic wells (yellow markers) and four electrical resistivity tomography (ERT) profiles (green lines P1 to P4). The temperatures of the coastal thermal anomaly (coloured scale) represent measurements taken at a depth of 20 cm below the beach surface. (d) Electrical Resistivity Tomography sections for the four profiles P1 to P4 in subfigure c (after Arango-Galván et al., 2011; Carbajal-Martinez, 2019). Vertical black lines in sections P3 and P4 mark the location and depth of two domestic thermal wells.

5.2. Numerical simulations methodology

The forward coupled thermal–hydraulic numerical simulations in this study were performed using the integral finite-difference code TOUGHRECT V. 4.13. This allows for transport and mixing of separate fluid phases through model porous rocks (Pruess et al., 1999), as required for the case of La Jolla Beach, where meteoric water encounters and mixes with seawater within the fault plane. TOUGHREACT incorporates temperature-dependent properties of pure and saline water, including viscosity, density, and enthalpy, utilizing steam table equations (International Formulation Committee., 1967). It uses Newton-Raphson iteration to solve partial differential equations governing mass balance and heat flow:

$$\frac{\partial M^{W,H}}{\partial t} = -\nabla \mathbf{F}^{W,H} + q^{W,H} \quad (5.1)$$

where $M^{W,H}$ is the total mass accumulation of water (W) and heat (H) in the system with respect to time, t . The term $\text{div} \mathbf{F}^{W,H}$ is the gradient of the total mass flux rate of water ($\text{kg m}^{-2} \text{s}^{-1}$) and heat ($\text{J m}^{-2} \text{s}^{-1}$), and $q^{W,H}$ is the sink ($-$) or source ($+$) term for each component. The equation essentially balances the inflows and outflows of water and heat in a given system, taking into account any sources or sinks.

For the present fully saturated, single-phase flow case, the parameter \mathbf{F}^W is equal to the Darcy flux, denoted as u (m s^{-1}):

$$u = -\frac{k}{\mu} (\nabla P - \rho g) \quad (5.2)$$

where k (m^2) is the intrinsic permeability of the rock and μ (Pa s) is the dynamic viscosity of water. The term ∇P (Pa m^{-1}) represents the hydraulic head gradient, while ρ is the density of water (kg m^{-3}), and g is the gravitational acceleration vector (m s^{-2}).

On other hand, the heat flux ($\text{J s}^{-1} \text{m}^{-2}$) includes both conductive and convective heat components in the porous medium:

$$\mathbf{F}^H = C_M T \rho_M u - \lambda \nabla T \quad (5.3)$$

where C_M ($\text{J kg}^{-1} \text{K}^{-1}$) and ρ_M (kg m^{-3}) denote the specific heat capacity and the density of the saturated porous medium, respectively. The variable T (K) is the temperature of the porous medium, and λ corresponds to the thermal conductivity of the wet rock ($\text{J s}^{-1} \text{m}^{-1} \text{K}^{-1}$). The gradient in temperature between adjacent grid blocks is defined as ∇T (K m^{-1}). The

porous medium parameters C_M and ρ_M are calculated as:

$$C_M = (1 - \emptyset)C_R + \emptyset C_w \quad (5.4)$$

$$\rho_M = (1 - \emptyset)\rho_R + \emptyset\rho_w \quad (5.5)$$

where \emptyset represents the porosity, C_R and C_w stand for the specific heat capacity of rock and water, respectively ($\text{J kg}^{-1} \text{K}^{-1}$), and ρ_w and ρ_R denote the density of rock and water, respectively (kg m^{-3}).

In order to accurately model the mixing of meteoric water and seawater, all simulations in this study utilized the EOS7 equation of state. This represents the aqueous phase as a mixture of pure water and brine (seawater) endmembers. The salinity of the mixture is represented by the mass fraction of brine (X_b). The density of the mixture (ρ_m) can then be expressed in terms of water density (ρ_w) and seawater density (ρ_b) as follows:

$$1/(\rho_m) = (1 - X_b)/(\rho_w) + (X_b/\rho_b) \quad (5.6)$$

Values of ρ_m are calculated as a function of P and T via EOS7.

Effects of salinity on the viscosity of the aqueous phase are modeled with a polynomial correction to the viscosity of pure water (μ_w). Thus, the viscosity of the mixture (μ_m) is represented as follows:

$$\mu_m(P, T, X_b) = \mu_w(P, T) f(X_b) \quad (5.7)$$

where

$$f(X_b) = 1 + 0.066X_b \quad (5.8)$$

The accuracy and reliability of the TOUGH code in modeling seawater–freshwater mixing have been demonstrated by [Na et al. \(2019\)](#) through a comparison of laboratory experiments and numerical simulations.

5.2.1. Model geometry

Our model is designed to enable the overall flow dynamics of the La Jolla Beach system as inferred by [Carbajal-Martinez et al. \(2023\)](#) from geochemical and hydrogeological constraints. The model onshore segment of the ABF should provide a permeable subsurface flow path that links high-elevation recharge areas on the land topography with the La Jolla Beach discharge site at sealevel. Similarly, the offshore extension of the fault should provide a permeable, seawater-saturated flow path that links the seafloor with La Jolla Beach.

Accordingly, our numerical model encompasses a large 3D domain measuring $34 \times 12 \times 11.5$ km (Figure 5.2). To accurately represent the study area, we initially discretized the domain using a regular rectangular mesh consisting of approximately 400,000 grid blocks. The grid block sizes vary according to the desired spatial resolution, with the smallest blocks ($15 \times 15 \times 20$ m) in the La Jolla Beach area at the center of the model (yellow star in Figure 5.2). The model includes an area of the Pacific Ocean (0–12 km from the western boundary of the domain) and a larger area of the mountainous hinterland to the east.

To define the onshore topography (up to 1 km a.s.l.) and seafloor topography (up to 0.4 km b.s.l.) of the study area (Figure 5.2), we incorporated a digital elevation model (DEM; (NOAA National Geophysical Data Center, 2006) and used the "fit surface" method in the PyTOUGH software to create an irregular mesh of the DEM (Croucher, 2015). Note that the seafloor constitutes the upper boundary of the model in the area of the Pacific Ocean. Thus, the ocean itself was not explicitly defined in our model. However, appropriate fluid pressure and temperature conditions were assigned to the seafloor boundary as described below.

5.2.2. Initial and boundary conditions

The model domain was assigned initial fixed boundary conditions to define hydrostatic pressure and conductive temperature distributions. Using an initial temperature of 16 °C at the coastal beaches (CICESE, 2019), the temperature of the land surface was set according to its elevation using an adiabatic cooling rate of -5.5 °C km⁻¹, and the temperature of the seafloor was set using a cooling gradient of -3.1 °C per 100 m depth below sealevel (Emery & Dewar, 1982).

In all the simulations, the land surface was set to be saturated with meteoric water, providing unlimited infiltration. Thus, surface runoff and temporal and spatial variations in rainfall over the real land surface are ignored. To define the fluid pressure of rainwater at the land surface ($P_{f,land\ surface}$; Pa), we utilized Equation 5.9 (Cavcar, 2000), which gives the atmospheric pressure as a function of elevation above sea level (z):

$$P_{f,land\ surface} = 10^5 [1 - (0.0065z / 289.15)]^{5.2561} \quad (5.9)$$

In contrast, the fluid pressure at the seafloor ($P_{f,seafloor}$; Pa) was calculated from the height of the overlying seawater column (h), the seawater density at 20 °C and 10^5 Pa ($\rho_b = 1025$ kg

m^{-3}), and the acceleration due to gravity (g ; m s^{-2}):

$$P_{f,seafloor} = \rho_b g h \quad (5.10)$$

To specify a conductive temperature distribution as the initial boundary condition, we used the regional geothermal gradient of $25 \text{ }^\circ\text{C km}^{-1}$ (Carbajal-Martinez, 2023), the mean elevation of the surface topography (0.295 km), and the mean annual temperature at sea level ($16 \text{ }^\circ\text{C}$). This resulted in a temperature of $300 \text{ }^\circ\text{C}$ at the lower boundary of the model (10.5 km b.s.l.). The depth of the model corresponds to the calculated depth of the BDTZ (Carbajal-Martinez, 2023). During the simulations, the lower and the four lateral and boundaries were open for conductive heat exchange and closed for fluid flow. The upper boundary, on the other hand, was open for both heat and fluid flow. The large dimensions of the model domain ensure that the simulation results for the La Jolla Beach geothermal system in the center of the model domain (Figure 5.2) are not affected by the definition of the boundary conditions. Moreover, the boundary conditions employed ensure that the temperature and pressure remain realistic throughout the entire model domain.

5.2.3. Model zones

The model was divided into two distinct hydraulic zones: the low-permeability host rock, and the permeable Agua Blanca Fault Zone. In the absence of relevant hydraulic well test measurements for the study area, we adopted porosity and permeability values for the host rock from studies conducted in similar granitic host rocks and orogenic tectonic settings (Stober & Bucher, 2007; Wanner et al., 2019; Alt-Epping et al., 2021). The host rock was assigned a porosity of 0.02 at the surface, gradually decreasing linearly to 0.01 with increasing depth. The permeability was fixed at 10^{-16} m^2 within the upper 2.5 km of the crust. Below that depth, the permeability distribution was set as a function of depth (z) using Equation 5.11, which is based on hydraulic well measurements in deep wells worldwide (Stober & Bucher, 2007):

$$\log k(\text{m}^2) = -1.38 \log z (\text{m}) - 15.4 \quad (5.11)$$

Unfortunately, the width, porosity and permeability of the fault zone are all unknown. Values of these parameters were therefore fitted by sensitivity studies, constrained as described further below and without any dependence on depth. Thus, three different fault

widths were simulated (15 m, 45 m, and 105 m) and porosity was assumed to be constant at 0.02. For each fault width, multiple simulations were conducted with varying permeability values to assess the sensitivity of the model results. In contrast to permeability and porosity, the model was assigned a homogeneous distribution of bulk rock density, thermal conductivity, and specific heat capacity, as specified in Table 5.1.

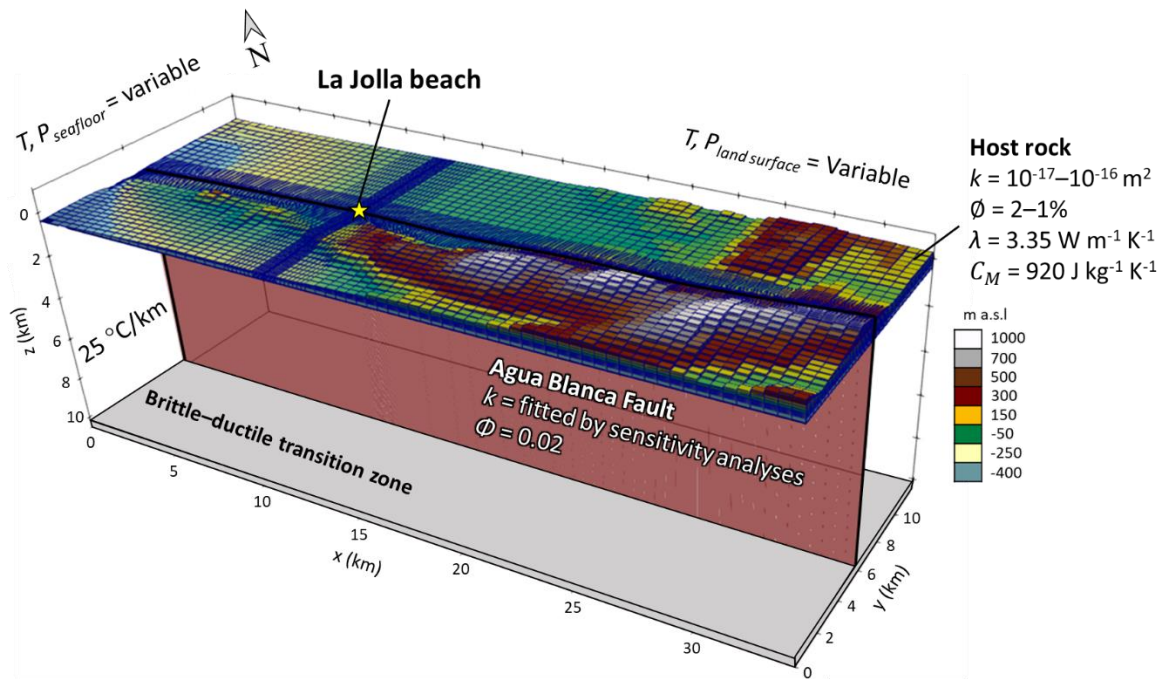


Figure 5.2. Large-scale model ($34 \times 12 \times 11.5$ km) of La Jolla Beach in Punta Banda, Baja California, Mexico, looking NNE. The figure depicts the numerical mesh (dark blue bands on the upper model surface are areas with very fine meshing), the onshore and seafloor topography of the study area, and the location of the two model domains: the Agua Blanca Fault Zone (red plane), and its surrounding host rock. Detailed information on the hydraulic and thermal properties and the boundary conditions of the model domain are provided in the text and in Table 5.1.

5.2.4. Numerical simulation Cases 1 and 2

In order to explore the factors influencing the formation and location of coastal amagmatic geothermal systems, we numerically simulated two distinct scenarios, Case 1 and Case 2, as

detailed in Table 5.1 and illustrated in Figure 5.3. While the general parameters described in subsection 5.2.3 were utilized for both cases, several modifications were introduced specifically for Case 2.

In Case 1, we assumed a homogeneous permeability and porosity within the fault plane, neglecting the presence of any sediment layers in the simulation (Figure 5.3a). However, in Case 2, we considered the detailed configurations of the offshore Bahia Todos Santos basin and the onshore Maneadero basin (Figure 5.1b). This involved integrating not only the depth of the crystalline basement but also the lateral and depth distribution of the cover sediments. To accurately establish the depth of the crystalline basement, we relied on results from joint inversion modeling of gravity and magnetic data (Figure 5.3b; [Pérez-Flores et al., 2004](#)). Above the basement, we included sediment data on seafloor samples collected in the Pacific Ocean, including sand and silt (Figure 5.3b; [Emery et al., 1957](#)), as well as the lithological information derived from shallow wells and geophysical measurements in the Maneadero basin ([Cruz-Falcón & Vázquez-González, 1989](#); [Daesslé et al., 2009](#)).

Porosity and permeability values for the sediments in Case 2 were based on values reported for the general sediment types ([Luijendijk & Gleeson, 2017](#); Table 5.1). The porosity of sediments was fixed to 20%. To account for the tectonic activity along the ABF, we assumed that the permeability of the sediments within the fault zone was at least one order of magnitude higher than that in the surrounding sediments (Table 5.1). Regarding the thermal properties of the sediments, we used constant values for both the thermal conductivity ($1.50 \text{ W m}^{-1} \text{ K}^{-1}$) and the specific heat capacity ($800 \text{ J kg}^{-1} \text{ K}^{-1}$) ([Midttømme et al., 1998](#)).

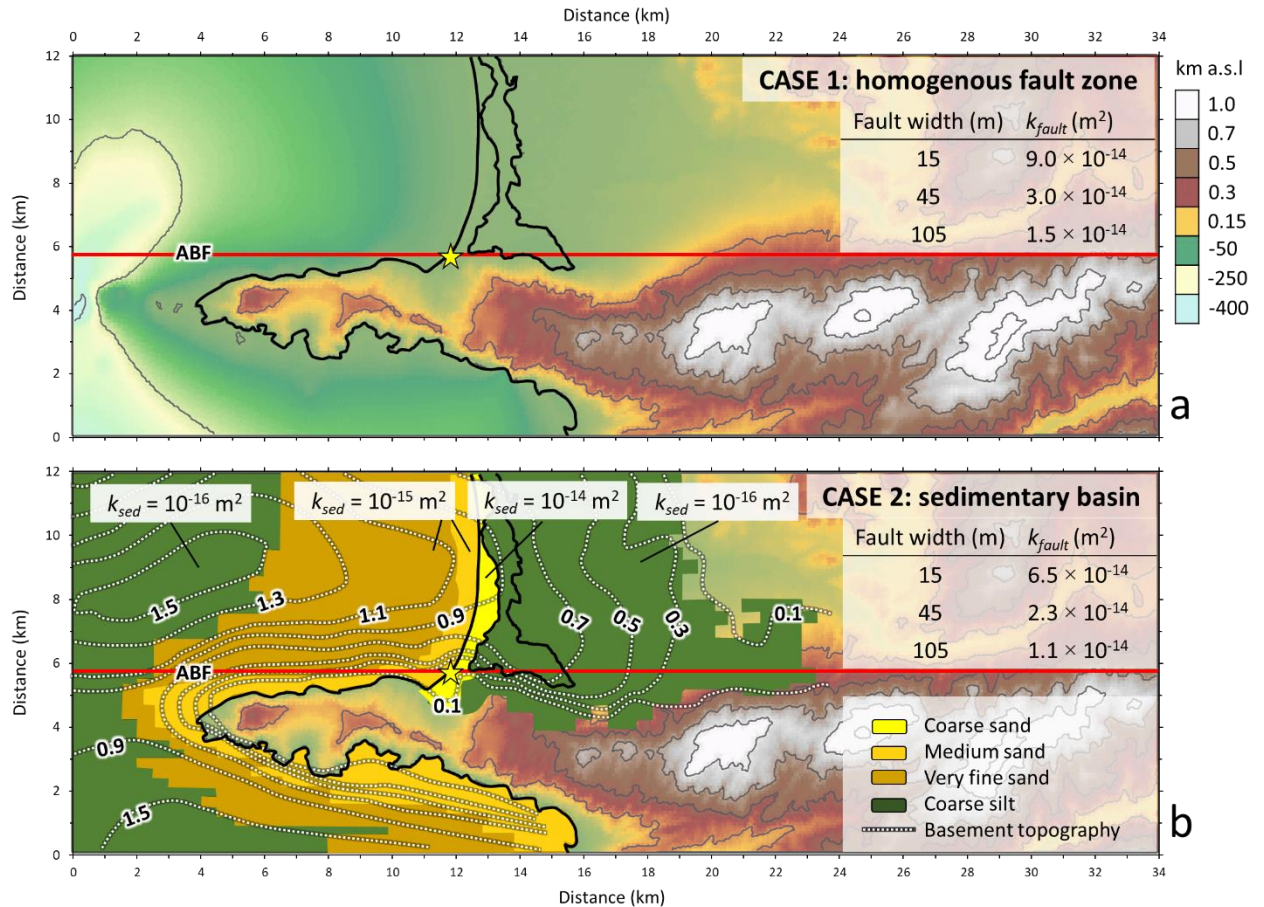


Figure 5.3. Maps of fault and sediment configuration considered for the various numerical simulations, also showing the corresponding permeability distribution and the Agua Blanca Fault (ABF, red line). (a) Case 1: Homogeneous fault and host rock permeability without any sediments above the basement. (b) Case 2: Case 1 plus additional definition of the full sedimentary cover (see text). For each case, the indicated permeabilities of the fault zone (k_{fault}) are those required to match the ~ 100 °C discharge temperature at La Jolla Beach in our simulations. The permeabilities specified for the surrounding cover sediments (k_{sed}) are based on literature values.

Table 5.1.

Values and sources of parameters used in the numerical models (Cases 1 and 2) simulating La Jolla Beach geothermal system, Baja California, Mexico. These parameters reproduce the observed discharge temperature of ca. 100 °C at La Jolla Beach.

Parameters and description	Model and host rock	Fault width			Data source
		15 (m)	45 (m)	105 (m)	
<i>Dimension of model</i>					
N-W and S-E extent	34 × 12 km				(NOAA National Geophysical Data Center, 2006)
Base of model	–11.5 km				
Upper boundary	Onshore and offshore topography				
<i>Boundary conditions</i>					
Rainwater pressure on land surface	Equation 5.9				(Cavcar, 2000)
Fluid pressure on seafloor	Equation 5.10				(Emery & Dewar, 1982)
Seawater density at 20 °C	1025 kg m ⁻³				
Change in land surface temperature with elevation a.s.l.	–5.5 °C km ⁻¹				
Change in seafloor temperature with every 100 m of depth b.s.l.	–3.1 °C				
Geothermal gradient	25 °C km ⁻¹				(Carbajal-Martinez et al., 2023)
Fixed <i>T</i> at the lower boundary	300 °C				
Permeability at the four lateral and lower boundaries	10 ⁻²⁵ m ²				
<i>Hydraulic properties of granitic host rock</i>					
Vertical permeability	Equation 5.11 First 2.5 km fixed at 10 ⁻¹⁶ m ²				(Stober & Bucher, 2007)
Porosity (linear decrease)	From 0.02 to 0.01				(Wanner et al., 2019)
Host rock density	2680 kg m ⁻³				
<i>Fault hydraulic properties, simulation Case 1</i>					
Permeability (k_{fault})		9.0 ⁻¹⁴ m ²	3.0 ⁻¹⁴ m ²	1.5 ⁻¹⁴ m ²	Sensitivity analysis
Porosity		0.02	0.02	0.02	
<i>Fault and sediment hydraulic properties simulation Case 2</i>					
<i>Basin sediment permeability (k_{sed})</i>					
Coarse sand	10 ⁻¹⁴ m ²				(Emery et al., 1957) (Luijendijk & Gleeson, 2017)
Medium sand	10 ⁻¹⁵ m ²				
Very fine sand	10 ⁻¹⁵ m ²				
Coarse silt	10 ⁻¹⁶ m ²				
<i>Sediment permeability within the fault ($k_{fault-sed}$)</i>					
Coarse sand		10 ⁻¹³ m ²	10 ⁻¹³ m ²	10 ⁻¹³ m ²	Sensitivity analysis
Medium sand		10 ⁻¹⁴ m ²	10 ⁻¹⁴ m ²	10 ⁻¹⁴ m ²	
Very fine sand		10 ⁻¹⁴ m ²	10 ⁻¹⁴ m ²	10 ⁻¹⁴ m ²	
Coarse silt		10 ⁻¹⁵ m ²	3 × 10 ⁻¹⁶ m ²	3 × 10 ⁻¹⁶ m ²	
Fault (k_{fault})		6.5 × 10 ⁻¹⁴ m ²	2.0 × 10 ⁻¹⁴ m ²	1.1 × 10 ⁻¹⁴ m ²	
Sediment porosity	0.2	0.2	0.2	0.2	(Luijendijk & Gleeson, 2017)
Host-rock density	2680 kg m ⁻³	2680 kg m ⁻³	2680 kg m ⁻³	2680 kg m ⁻³	
Sediment thickness	< 1.5 km	< 1.5 km	< 1.5 km	< 1.5 km	
<i>Thermal properties</i>					
Thermal conductivity of host rock	3.34 W m ⁻¹ K ⁻¹				(Wanner et al., 2019)
Specific heat capacity of host rock	920 J kg ⁻¹ K ⁻¹				
Thermal conductivity of sediments	1.50 W m ⁻¹ K ⁻¹	1.50 W m ⁻¹ K ⁻¹	1.50 W m ⁻¹ K ⁻¹	1.50 W m ⁻¹ K ⁻¹	(Midtømme et al., 1998)
Specific heat capacity of sediments	800 J kg ⁻¹ K ⁻¹	800 J kg ⁻¹ K ⁻¹	800 J kg ⁻¹ K ⁻¹	800 J kg ⁻¹ K ⁻¹	

5.3. Results

In all the simulations, the hydraulic head gradient induced by the land topography drives an inexhaustible amount of meteoric water from high elevations deep into the ABF, where it is heated by the granitic basement rocks. The heated water rises to discharge at or near La Jolla Beach, and along its upflow path it mixes with an inexhaustible amount of seawater that has infiltrated the subseafloor extension of the fault.

5.3.1. Simulation Case 1

In this section, we present the findings from Simulation Case 1, which focused on exploring the sensitivity of the La Jolla geothermal system to fault permeability and fault width. Comparison of steady state simulations allows us to investigate the impact of these parameters on crucial aspects of the system, including its coastal location, temperature, and salinity.

5.3.1.1. Sensitivity analysis: fault permeability and discharge temperature

Simulation results for Case 1 involve varying fault-zone widths and permeabilities ranging from 15 to 105 m and 2 to $9 \times 10^{-14} \text{ m}^2$, respectively (Figure 5.4). The surface temperature in the simulations shows high sensitivity to both fault width and fault permeability. For instance, at a fault width of 15 m, thermal anomalies above 30 °C develop at the land surface if permeabilities are assumed to be greater than $5 \times 10^{-14} \text{ m}^2$ (upflow rates $> 126 \text{ m yr}^{-1}$). At a permeability of $9 \times 10^{-14} \text{ m}^2$, the surface temperature reaches 100 °C, close to the observed discharge temperature at La Jolla Beach (Figure 5.4b). However, when the fault width is increased to 45 or 105 m, the surface temperature remains essentially the same if the permeabilities calibrated to lower values of 3 and $1.5 \times 10^{-14} \text{ m}^2$ (Figure 5.4e).

This behavior occurs because the discharge temperature is predominantly determined by the system-wide upflow rate, which is controlled by the product of permeability and the 3D extent of the upflow zone, in our case represented by the fault width (Wanner et al., 2019). Consequently, the permeability in the simulations, which matches the 100 °C discharge temperature, decreases as the fault width increases (9×10^{-14} , 3×10^{-14} and $1.5 \times 10^{-14} \text{ m}^2$ at widths of 15, 45 and 115 m, respectively). Consequently, this also affects the corresponding

porewater velocities (946, 315, and 183 m yr⁻¹). In contrast, the strong sensitivity of the simulated surface temperature to permeability at a constant fault width (Figure 5.4b) is attributed to the positive feedback on the flow rate via the temperature dependency of fluid density and viscosity (Eq. (5.7)).

5.3.1.2. Seawater infiltration into the continental crust through the fault zone

The permeability of the fault zone plays a crucial role not only in determining the surface temperature but also influencing the extent of seawater infiltration into the continental crust. As fault permeability increases, a larger fraction of seawater infiltrates, as depicted in Figure 5.5, which aligns with findings of previous modeling studies (Karasaki et al. 2011; Magri et al. 2012). Consequently, the fractions of seawater within the center of the simulated thermal anomaly vary from 10 to 70% (Figure 5.4c).

Furthermore, the fault permeability has a significant impact on the pattern of seawater intrusion landward within the fault plane. In cases where the permeability is low, the contact between seawater and heated meteoric water exhibits a gentle slope of less than 45°, enabling seawater to penetrate horizontally up to 4 km inland through the ABF (Figure 5.5). This behavior arises due to the formation of a semi-horizontal density-driven stratification caused by low-permeable fault values (Figure 5.5). However, when fault permeability increases, seawater infiltration and water flux accelerate, leading to the intrusion occurring along a semi-vertical plane (~80–90°).

5.3.1.3. Inland location of the thermal anomaly

Although calibrating the permeability allows us to approximate the discharge temperature (~100 °C) at La Jolla Beach, it is important to note that the thermal anomaly is consistently situated 3–5 km inland from the coastline (Figure 5.4b, d). Additionally, the fault width does not influence the position of the discharge site (Figure 5.4e). As a result, these simulations do not fully capture the location of the observed thermal anomaly right at the coast. The main reason for this discrepancy lies in the high permeability of the entire fault zone, which enables the unrestricted infiltration of seawater until it reaches the coastline (Figure 5.4d).

Consequently, under these conditions, the density contrast between seawater and meteoric water inhibits the upflow of meteoric water directly beneath the coast (Figure 5.4f). To accurately replicate the location of the thermal anomaly at the coastal zone, it is necessary to reduce the amount of seawater infiltrating into the ABF. Details on addressing this issue will be discussed further in the following chapter.

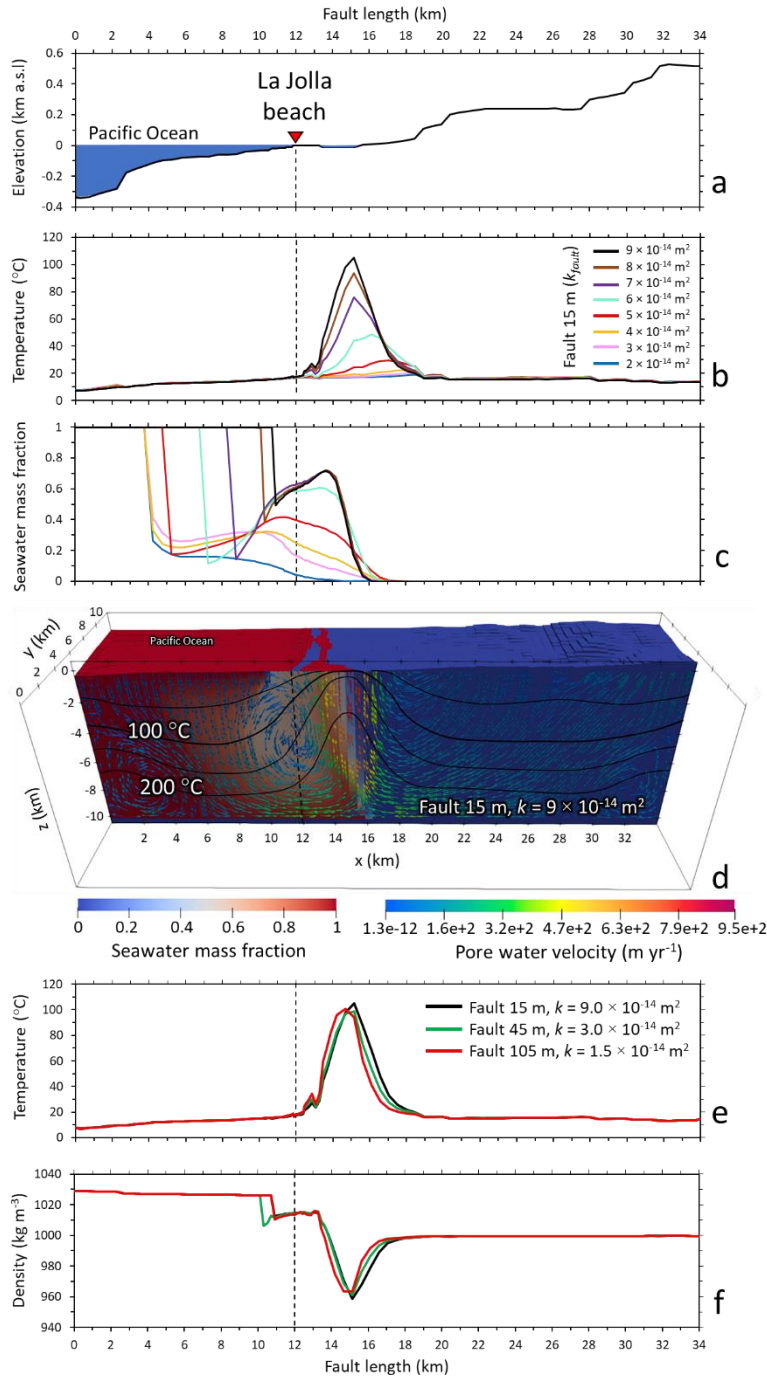


Figure 5.4. Steady state simulation results for Case 1 shown in a vertical section within the plane of the Agua Blanca Fault. In all subfigures, the location of La Jolla Beach at ~12 km along the fault is shown as a dotted vertical line. (a) Topographic surface along the fault. (b) Temperature profiles along the topographic surface for a 15 m wide fault zone and variable fault permeabilities. (c) Profiles of seawater mass fractions at the topographic surface for the same fault width and permeabilities as shown in b. Fractions of meteoric water (not indicated) are equal to 1 minus the seawater fractions. (d) Distribution of seawater mass fractions (colored areas), isotherms (black contours), and flow vectors (colored arrows) for a fault width of 15 m and permeability of $9 \times 10^{-14} \text{ m}^2$. (e) Temperature profiles at the topographic surface for various combinations of fault width and permeability, which all match the discharge temperature of around 100 °C at La Jolla Beach. (f) Profiles of water densities at the topographic surface for the same fault width and permeabilities as shown in e.

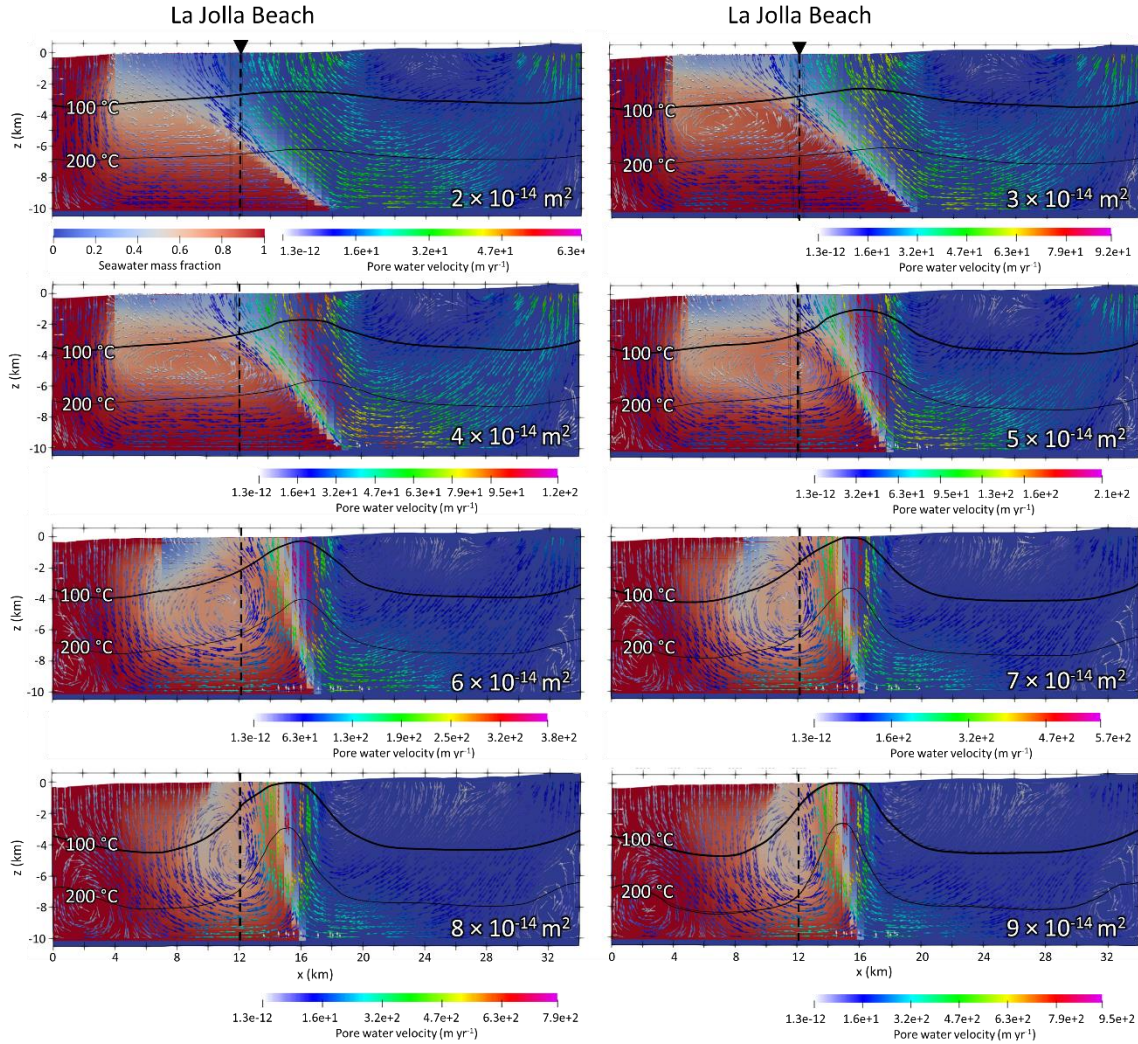


Figure 5.5. Steady state simulation results for Case 1 for a fault width of 15 m and variable fault permeabilities. Colored areas show distribution of seawater mass fractions (scale below top-left panel applies to entire Figure). Black contours show isotherms. Flow vectors (arrows) have color scales that vary between subfigures. The simulation with the highest fault permeability (lower-right panel) closely reproduces the discharge temperature at La Jolla Beach (~100 °C) but not its geographical location.

5.3.2. Simulation Case 2

In this section, we delve into the details of Simulation Case 2, where we aimed to enhance the realism of our simulations by explicitly defining the base of the crystalline basement and incorporating the full distribution of sediments in the basins of Bahia Todos Santos and the

Maneadero valley (see Figs. 5.3b and 5.6a). This approach allowed us to consider a more comprehensive representation of the geological setting of the La Jolla Beach area.

Throughout Case 2, we explore various combinations of fault width, fault permeability, and permeability of the sediments. The objective is to closely approximate the observed discharge temperature of approximately 100 °C, salinity and location of the thermal anomaly at La Jolla Beach (see Figure 5.6). By incorporating the geological complexities of the region, we gain valuable insights into the interplay between these factors and their influence on the formation and behavior of the coastal amagmatic geothermal system.

5.3.2.1. Coastal location and extension of the thermal anomaly

By incorporating the detailed basement topography and the sediments above it (Figure 5.6a) has a notable impact on the extent of seawater infiltration through the Agua Blanca Fault (ABF) and the location of the thermal anomaly. This comprehensive representation of the geological features allows us to observe how the hydrostatic pressure gradient, driven by the mountainous zone and the pressure distribution in the Pacific Ocean, facilitates the infiltration of meteoric water and seawater into the ABF, extending all the way down to the lower model boundary known as the BDTZ. Consequently, a thermal water upflow zone is formed beneath the coastal area (Figure 5.6b). Within this upflow zone, the pore water velocity ranges from 1.3×10^{-12} to 1.3×10^3 m yr⁻¹, with the highest velocities concentrated at the center of the thermal water upflow zone. These upflow rates are consistent with previous studies indicating that shallow thermal anomalies tend to develop when upflow rates exceed 3.0 m yr⁻¹ (López & Smith, 1995; Wanner et al., 2020; Alt-Epping et al., 2021, 2022).

By calibrating the permeability of the ABF based on the fault widths, our simulations consistently reproduce both the observed location and the discharge temperature of approximately 100 °C at La Jolla Beach (Figure 5.6c). The horizontal width of the generated shallow thermal anomaly is only about 1 km (Figure 5.6c) compared with the width of Case 1, which spans around 4 km (Figure 5.4e). This alignment is much more consistent with the thermal anomaly inferred from temperature measurements in shallow domestic boreholes and electrical resistivity measurements in the vicinity of La Jolla Beach (Figure 5.1c).

5.3.2.2. Water properties: Seawater fractions and viscosity

The thermal water upflow zone beneath the coastal area is a result of the mixing of infiltrated seawater and meteoric water. The discharged thermal water, with a temperature of approximately 100 °C, contains a seawater mass fraction ranging from 10% to 35% (Figure 5.6d). The density and viscosity of this thermal water are approximately 957 kg/m³ and 0.3 cP, respectively (Figure 5.6e). The density and viscosity of this thermal water are approximately 957 kg/m³ and 0.3 cP, respectively (Figure 5.6e). For instance, the seawater infiltrating into the ABF initially exhibits a maximum viscosity of around 1.6 cP, which progressively decreases to a minimum of 0.1 cP within the system, a reduction by 16 times. In contrast, the maximum density of seawater is approximately 1030 kg/m³, which decreases to a minimum of 820 kg/m³ within the system, a reduction by 1.3 times. Consequently, in the context of coastal geothermal systems, the density of seawater plays a more significant role than viscosity since it is less sensitive to temperature and serves as an additional force, alongside hydrostatic pressure, to inhibit the landward intrusion of meteoric water beyond the coastline.

Moreover, our simulations reveal the presence of a convection cell beneath the Pacific Ocean along the ABF plane, characterized by a seawater fraction ranging from 50% to 80% (Figure 5.6b). This convection cell arises from the density contrast between seawater and meteoric water, as well as the lateral infiltration of meteoric water from the Punta Banda Peninsula. (Figure 5.7).

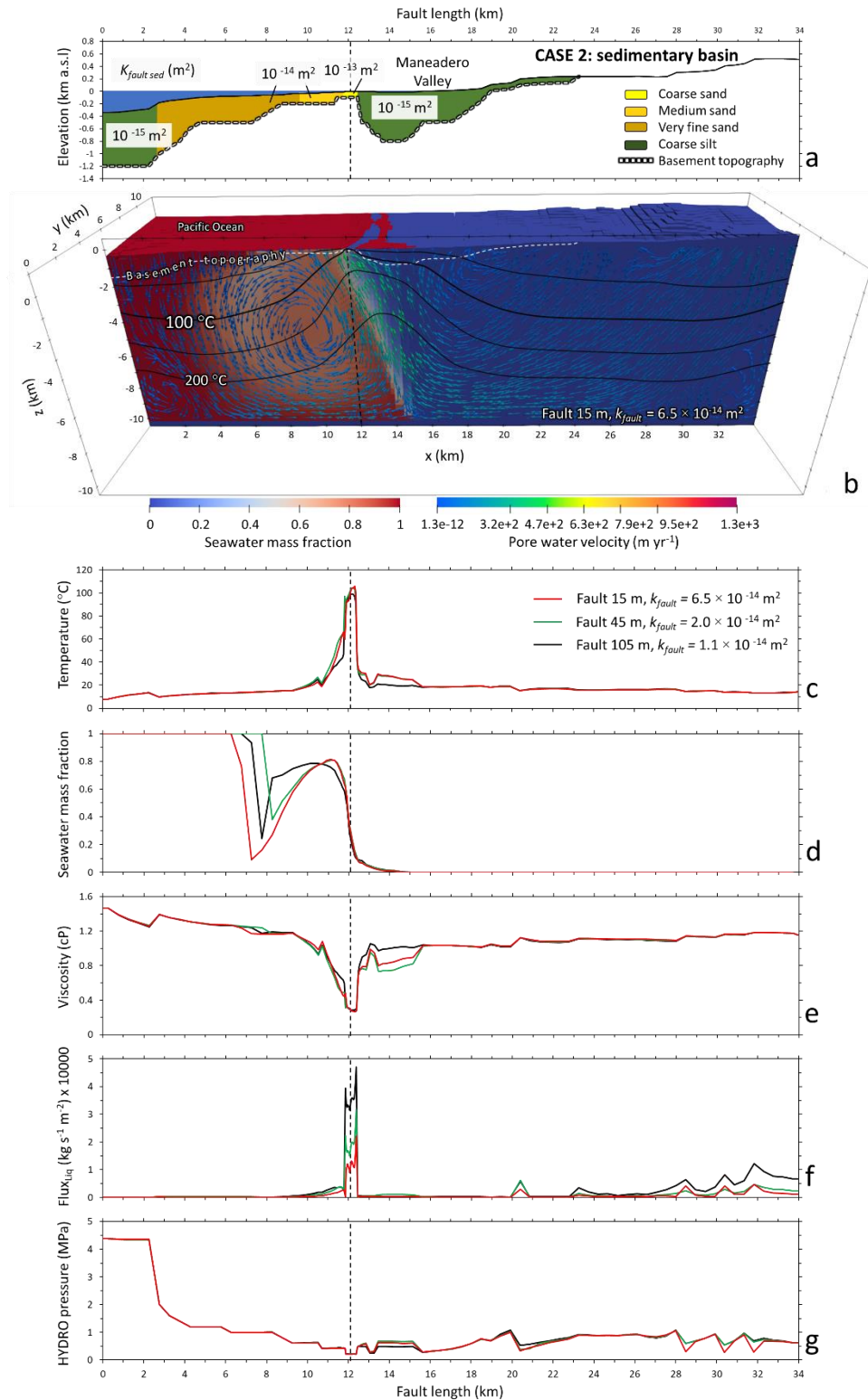


Figure 5.6. Steady state simulation results for Case 2 shown for the vertical section along the Agua Blanca Fault. (a) Topography and bathymetry along the fault, also showing the

topography of the top of the crystalline basement and the distribution of seafloor sediments. (b) Distribution of seawater fractions (colored areas), isotherms (black contours), and flow vectors (colored arrows) for a fault width and permeability of 15 m and $6.5 \times 10^{-14} \text{ m}^2$, respectively. (c–g) Results for Case 3 using various combinations of fault width fault permeability, all matching the discharge temperature of $94 \text{ }^\circ\text{C}$ at La Jolla Beach. (c) Surface temperature profiles. (d) Profiles of seawater fractions at the surface. (e) Profiles of water densities at the surface. (f) Profiles of water viscosity at the surface. (g) Profiles of water pressure at the surface, showing that the lowest pressure occurred at the coastal zone. In all subfigures, the location of La Jolla Beach at $\sim 12 \text{ km}$ along the fault is shown as dotted vertical line.

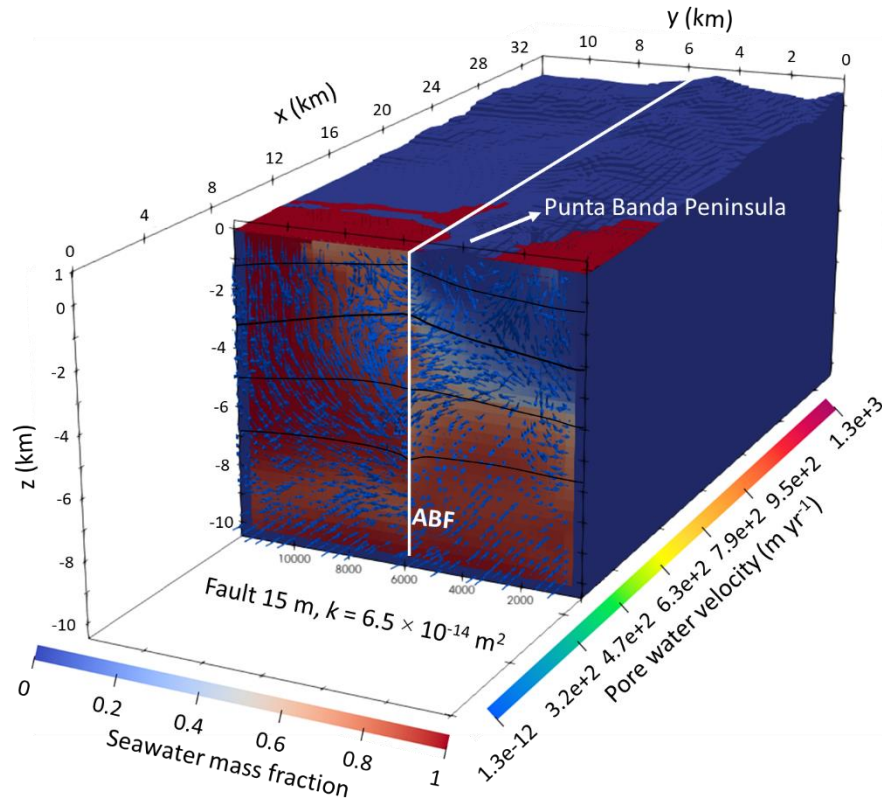


Figure 5.7. 3D clip of Simulation Case 2, showing a hydraulic-thermal simulation perpendicular to the Agua Blanca Fault with a fault width of 15 m. The clip demonstrates the important role of the Punta Banda Peninsula in water flow, as there is a decrease in the seawater fraction along the fault plane.

5.4. Discussion

5.4.1. Seawater as a hydraulic barrier: the role of density and viscosity

In this section, we explore the crucial role of seawater as a hydraulic barrier, which plays a fundamental role in determining the location of coastal geothermal systems and inhibits the seaward circulation of meteoric water beyond the coast through the ABF.

During the simulations, we ran the models for up to 1,000,000 years to achieve a steady state. The evolution of the properties of the thermal anomaly, including temperature, seawater fraction, density, and viscosity, was tracked on the surface for a 15-meter-wide fault at 12 different time points in both Case 1 and Case 2 (Figure 5.8).

In Case 1, we observed the generation of a thermal anomaly of approximately 100 °C inland, with its center located at km 13 after 10,000 years. Over time, as the simulations progressed, the anomaly gradually shifted towards the inland area, reaching km 15 and maintaining a steady temperature of around 100 °C after 500,000 years (Figure 5.8a). In contrast, in Case 2, we observed the emergence of a thermal anomaly of approximately 40 °C beneath the Pacific Ocean, positioned between km 8 and 10, after 10,000 years (Figure 5.8e). As time elapsed and the simulations approached 500,000 years, the anomaly reached a steady state, with its temperature stabilizing at around 100 °C at the coastal zone (km 12).

These findings suggest that the age of the coastal amagmatic geothermal system at La Jolla Beach could be as old as 250,000 years or more, with steady-state conditions at around 1.0 million years ago, assuming that the fault permeability and sediment conditions have remained similar to the present day. This age aligns well with the estimated tectonic activation of the ABF approximately 1.3 million years ago ([Rockwell et al., 1989](#); [Wetmore et al., 2019](#)).

The differences between Case 1 and Case 2 lie in the evolution of the position of the thermal anomaly over time and its temperature. Unlike Case 1, Case 2 replicates field observations, where the thermal anomaly is located in the coastal zone at a temperature of approximately 100 °C with a seawater fraction ranging from 10 to 35%. It is crucial to highlight that seawater acts as a hydraulic barrier, determining the position of the thermal anomaly. This process is evident in both cases, as the curves representing the seawater fraction (Figures 5.8b, f) are positioned ahead of the thermal water temperature curves

(Figure 5.8a, e). Additionally, density (Figure 5.8c, g) and viscosity (Figure 5.8d, h) evolve over time and with the position of the thermal anomaly. Both water properties decrease their values at the center of the thermal anomaly as the simulations achieve a steady state.

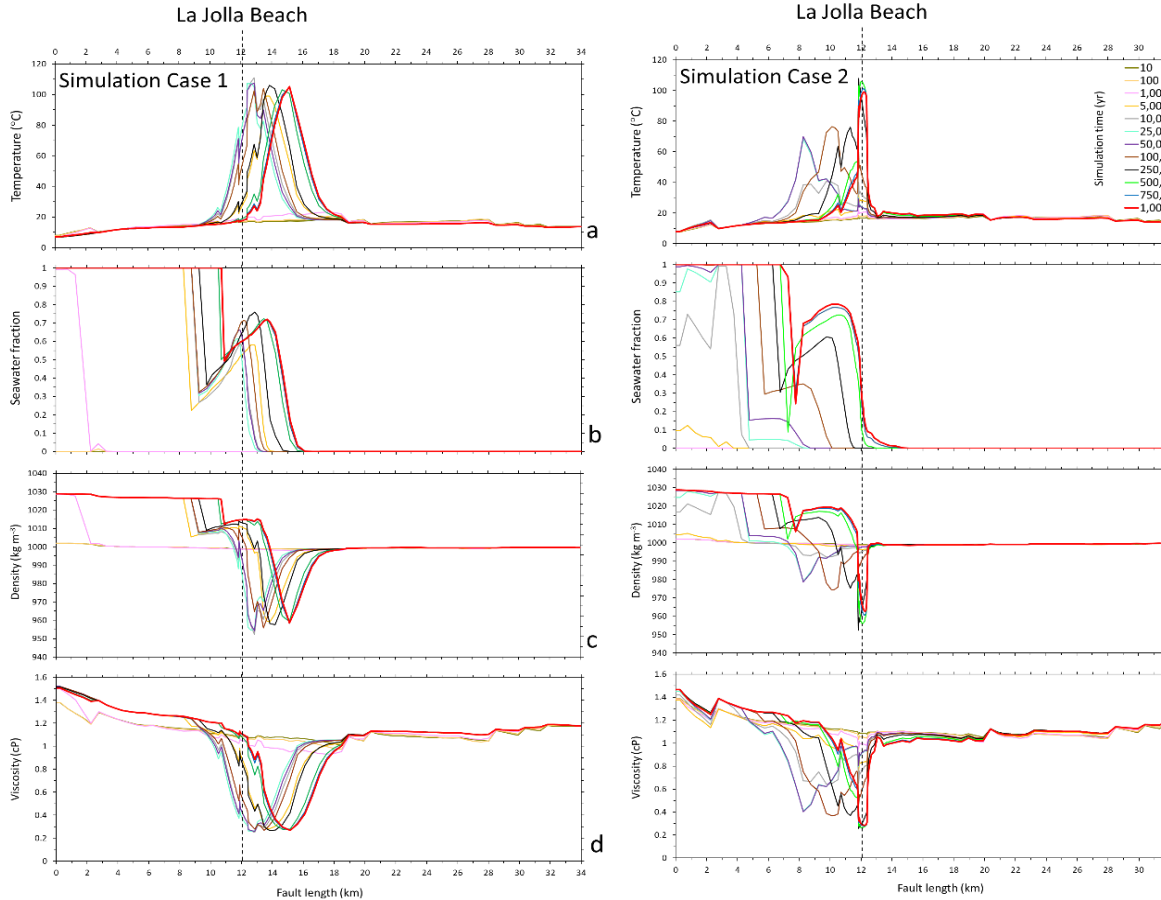


Figure 5.8. Temporal evolution of various fluid properties of simulation Case 1 (Figure a-d) and Case 2 (Figure e-h) at a fault width of 15 m and fault permeability of $9.0 \times 10^{-14} \text{ m}^2$ and $6.5 \times 10^{-14} \text{ m}^2$, respectively. The plots illustrate the progression towards steady state conditions, which are achieved after approximately 250,000 years.

5.4.2. Water infiltration, recharge limitation due to arid climate

The study area experiences a subtropical arid climate with an average annual precipitation of 275 mm. In our simulations, we utilize a fixed pressure upper boundary, which restricts our ability to control the rate of water recharge infiltrating into the simulated system. Interestingly, the quantification of meteoric water infiltration on the upper boundary of the

3D hydraulic–thermal simulations reveals a relatively low value, ranging from 4.2–12.4 mm yr⁻¹. This suggests that only 1.5–4.5% of the annual precipitation infiltrates into the system in both simulation cases (Table 5.2). However, to gain a comprehensive understanding of the infiltration dynamics, it is crucial to quantify the infiltrated water through the different domains within the fault zone and bulk rock, as well as differentiate between seawater and meteoric water contributions.

5.4.2.1. Water infiltration: Fault zone vs. host rock

In both Simulation Case 1 and Case 2, meteoric water comprises a larger proportion (54–85%) of the infiltrated water compared to seawater (15–46%). Furthermore, a significant percentage of water infiltrates through the fault zone (77–98%), which is considerably higher than that through the host rock (2–23%). This discrepancy can be attributed to the high permeability of the fault zone (Table 5.2). Despite being smaller in magnitude than the infiltration along the fault plane (77–85%), the water infiltrating through the host rock (15–23%) plays a crucial role in determining the flow direction and providing the potential energy to drive fluids in the upper crust. Simulation Case 2 further emphasizes the importance of the host rock infiltration, confirming that the ABF effectively serves as a collector for meteoric water that has infiltrated through the host rock (Carbajal-Martinez et al., 2023).

5.4.3. Pressure minima and fluid upflow at the coastal zone

The water circulation driven by hydraulic heads from the mountainous zone and the Pacific Ocean occurs at significant depths, transporting heat towards the coastal zone, as illustrated in Figure 5.9b (e.g., at approximately 6 km depth). This flow pattern results in the formation of two cold thermal anomalies beneath areas with higher head gradients (Figure 5.9b). Conversely, heat transport from these regions generates a thermal anomaly with elevated temperatures beneath zones characterized by a low hydraulic gradient and pressure, such as the coastal zone. It is important to note that the deep thermal anomaly is more extensive, both in length and width, compared to the shallow subsurface anomaly shown in Figures 5.9a.

Table 5.2

Comparison of rates and fractions of meteoric water infiltration versus seawater infiltration through the model topographic surface for the two simulation cases, as a function of model fault width. The table also shows the relative contributions of seawater and meteoric water, as well as the infiltration laterally along the fault zone versus the host rock. Additionally, cumulative discharge rates of waters exfiltrating through the model topographic surface at temperatures above 50 °C at La Jolla Beach are provided.

Fault width (m)	15	45	105
CASE 1			
<i>Seawater vs. host rock:</i>			
Seawater (mm yr ⁻¹)	6.3	5.3	7.1
Meteoric water (mm yr ⁻¹)	7.3	8.2	12.4
Seawater infiltration (mass %)	46	39	36
Meteoric water (mass %)	54	61	64
<i>Fault zone vs. host rock:</i>			
Infiltrated via fault (mass %)	97	97	98
Infiltrated via host rock (mass %)	3	3	2
Discharge ≥50°C (L s ⁻¹)	0.2	0.2	0.3
CASE 2			
<i>Seawater vs. host rock:</i>			
Seawater (mm yr ⁻¹)	0.9	1.2	1.4
Meteoric water (mm yr ⁻¹)	4.2	4.6	8.0
Seawater infiltration (mass %)	18	21	15
Meteoric water (mass %)	82	79	85
<i>Fault zone vs. host rock:</i>			
Infiltrated via fault (mass %)	77	84	85
Infiltrated via host rock (mass %)	23	16	15
Discharge ≥50°C (L s ⁻¹)	0.7	0.9	1.1

Furthermore, the fluid pressure along the thermal water upflow pathway exhibits the lowest values along the ABF, as depicted in Figures 5.6f and 5.9c. Specifically, at a depth of 6 km beneath La Jolla Beach, the simulated fluid pressure is 58 MPa, while in the Pacific Ocean and the mountainous zone, the pressure reaches up to 61 MPa (Figure 5.9c). This effect is attributed to the fact that the coastal zone experiences minimal pressure conditions,

which consequently drives fluid upflow in this region. As a result, thermal water ascends through the permeable fault at significantly higher temperatures and velocities compared to the surrounding host rock. The pressure gradient created by the minimal pressure at the coastal zone acts as a driving force, propelling the thermal water towards the surface with substantial energy, leading to the formation and sustenance of the coastal geothermal system at La Jolla Beach.

5.4.4. Water exfiltration: Shallow thermal anomaly size

Previous studies using thermal–hydraulic simulations to study fault-hosted orogenic amagmatic geothermal systems have successfully reproduced the temperature and spatial distribution of thermal anomalies at the surface (Taillefer et al., 2018; Wanner et al., 2019; Alt-Epping et al., 2022). With fault permeabilities and thicknesses in the range of 10^{-15} – 10^{-14} m² and 100–300 m, respectively, these studies used similar values than those calibrated for our La Jolla Beach simulations. However, some of the previously published simulations have resulted in thermal anomalies with unusually large sizes at the surface, raising questions about the influence of upper boundary conditions. For example, for the Têt fault system in the Pyrénées, simulated thermal anomalies on valley floors reached lengths of up to ~8 km (Taillefer et al., 2018). Such a large extension may be attributed to the thermal boundary condition applied at the surface of the corresponding model. Taillefer et al. (2018) employs a condition that involves higher heat transfer coefficients at the specific shallow locations of hot springs, which leads to increased heat flow in those specific areas. As a consequence, when the hot deep fluid reaches the surface, it can cause significant expansions of the thermal anomaly.

In contrast, simulations for the Grimsel Pass system in Switzerland have depicted a small thermal anomaly of approximately 0.5 km in length by introducing a vertical conduit (100 × 100 m) of high permeability (10^{-13} m²) along the fault plane (Wanner et al., 2019; Alt-Epping et al., 2022). which compares well with temperature measurements along a tunnel wall. From the comparison of the Têt Fault and the Grimsel Pass systems, it follows that the extent of shallow thermal anomalies caused by amagmatic orogenic geothermal system is poorly constrained.

In this context, the large difference in the width of the thermal anomalies obtained in for Simulation Case 1 and Case 2 (4 vs. 1 km) are useful for providing better insights regarding the position and 3D extent of shallow thermal anomalies. In this study, the differences in length of the thermal anomalies are intricately linked to the topography of the crystalline basement and the distribution of sediments within the study area that are incorporated in simulation Case 2 (Figure 5.9a). Compared to Case 1, the thickness of the seafloor sediments reduces the infiltration of seawater through the fault zone (Table 5.2). Moreover, the specific arrangement of sediments in the Maneadero Valley basin and Bahia Todos Santos direct the upflow of thermal water towards the coastline, with a thermal water discharge ranging from 0.7 to 1.1 L s⁻¹ over an area of 0.112 km², and thereby significantly affecting the 100°C isotherm (Figure 5.6b, 5.9a).

The large difference of the extent of the thermal anomaly obtained for Simulation Case 1 and 2 thus suggests that the specific geological setting within a natural hydraulic upflow zone such as the coastline collectively regulates the length of the shallow thermal anomaly. Consequently, in other magmatic geothermal systems lacking similar sediment or structural features to guide the direction of water flow, larger thermal anomalies may be observed at the surface. This emphasizes the significance of the topographical and sedimentary characteristics in controlling the extent and behavior of shallow thermal anomalies within these geothermal systems.

It is important to highlight the significant role that fault permeability plays in the formation of thermal anomalies at the surface. Based on the insights gained from the numerical simulations presented in Chapter 4 of this thesis and the current Chapter 5, we can infer that the size and magnitude of the La Jolla Beach anomaly may control by a local permeability anomaly beneath La Jolla Beach (1D vertical tube) or by the ABF intersecting the topography of the contact surface between unconsolidated sediments and the crystalline basement. It is possible that a combination of these factors contributes to the observed phenomena. In simpler terms, the relatively shallow depth of the crystalline basement beneath La Jolla could be linked to a permeable structure that acts as a preferential pathway for water flow. This aligns with the observation that the ABF exhibits a high degree of tectonic extension, indicative of elevated permeability in proximity to the coastal area.

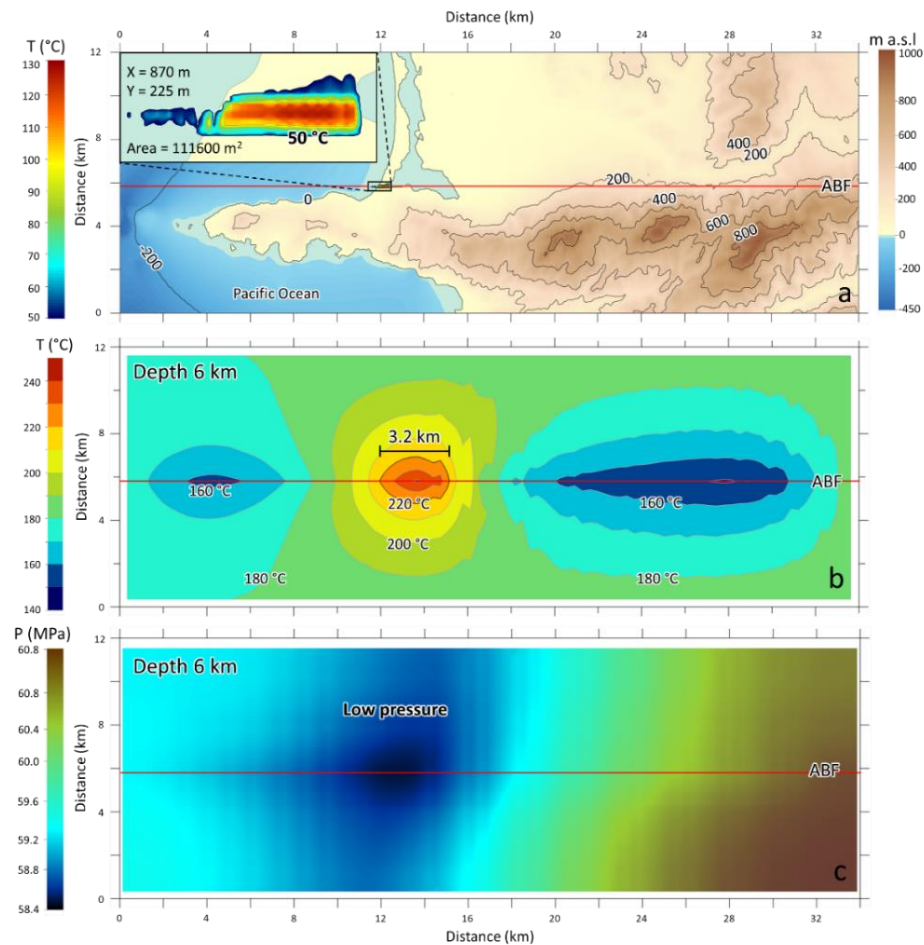


Figure 5.9. Steady state temperature and pressure distributions simulated for Case 2 for various horizontal sections a) Temperature distribution at a depth of 30 m below sea level, illustrating the size of the shallow thermal anomaly forming at La Jolla Beach. b) Temperature distribution at a depth of 6 km, showing that the extent of the anomaly is much larger at depth. c) Pressure distribution at a depth of 6 km, revealing a pressure minimum along the ABF developed directly beneath La Jolla Beach.

5.5. Conclusion

This study has focused on investigating the formation and behavior of amagmatic orogenic geothermal systems, with a specific emphasis on La Jolla Beach. Our simulations examined the role of topography, bathymetry, fault zones, and sediments on the location and magnitude of these geothermal systems. Through our sensitivity analysis, we identified that seawater plays a crucial role as a hydraulic barrier, restricting the circulation of meteoric water beyond

the coastline. Additionally, fault permeability emerged as a key control factor determining the magnitude of the geothermal system. Higher fault permeability resulted in hotter water discharge and greater infiltration of seawater through the ABF. Furthermore, the topography and bathymetry significantly influenced the three-dimensional flow of meteoric water and seawater, with fluids infiltrating through the host rock being effectively collected by the ABF. Remarkably, the infiltration of meteoric water was found to be higher than that of seawater, and most of the infiltration occurred through the fault zone, rather than the host rock. In our simulation results for Case 1 considering a homogenous host rock, we obtained an upflow zone situated 5 km inland from the coastline and resulting in discharge temperatures of 100 °C consistent with field observations. In contrast, Case 2, which incorporated basement topography and sediments of the study area, successfully replicated all field observations. Notably, the simulation accurately reproduced the location of the thermal anomaly at the coastal zone, with an extension of approximately 500 m, surface temperatures around 100 °C, and a seawater fraction ranging from 10–35%. Intriguingly, we found that the thickness of sediments plays a crucial role in governing the amount of seawater infiltration through the fault zone and influencing the flow of upflow thermal water towards the coastline. Together with the minimum pressure conditions at the coast, these factors collectively regulated the length of the shallow thermal anomaly. In conclusion, our study provides valuable insights into the behavior of amagmatic orogenic geothermal systems, highlighting the importance of considering topography, bathymetry, fault zones, and sediment characteristics. Understanding these key factors is essential for sustainable geothermal exploration and utilization.

Acknowledgments

This work was supported by a Swiss Government Excellence Scholarship granted to Daniel Carbajal-Martínez.

Supplementary data

All simulation input files on which this research is based are publicly available at the Zenodo repository (<https://doi.org/10.5281/zenodo.8379168>).

6. Hot springs on ocean beaches: a global phenomenon

Daniel Carbajal-Martínez^{1,*}, Christoph Wanner¹, Larryn W. Diamond¹, Loïc Peiffer²

¹ Rock–Water Interaction Group, Institute of Geological Sciences, University of Bern, Switzerland

² Departamento de Geología, Centro de Investigación Científica y de Educación Superior de Ensenada (CICESE), Ensenada, Baja California, México.

In preparation for submission to a peer-reviewed journal

Abstract

Coastal geothermal systems, characterized by discharge of thermal waters where permeable faults intersect coastlines, are remarkably common worldwide. Their spring temperatures reach up to ~100 °C and they thus have potential to supply sustainable energy for applications such as power production, seawater desalination, greenhouse operations, and space heating. Despite their prevalence, the mechanisms governing their behavior and specific location at the coastline remain unclear. Here we present generic, three-dimensional thermal–hydraulic numerical simulations to explain these phenomena. Our results show that coastal geothermal anomalies form by deep circulation of meteoric water through permeable fault networks, driven by the hydraulic head gradients from the high-elevation hinterland. Flow of the heated groundwater beyond the coastline is blocked within the fault plane by infiltrating, higher density seawater. An upflow zone spontaneously forms below the coastline, where the convection cells of the two water types impinge and mix, leading to discharge of hot, variably saline water at the surface. The discharge sites, salinities and temperatures of natural systems are precisely reproduced by the simulations when account is taken of seafloor sediments that slow down recharge of seawater into the fault plane. As well as explaining the visible features of the hot springs, the simulations reveal that large plume-like bodies of rock become heated around the deep upflow zone of the thermal water. Temperatures within these plumes commonly exceed the critical threshold for petrothermal electricity production at depths of 2 km or less below the surface.

6.1. Introduction

Coastal geothermal systems, characterized by thermal water discharge and elevated temperatures in the coastal zone, represent a global phenomenon. These intriguing systems are most frequently located along transform and divergent tectonic plate boundaries (Figure 6.1a). They are visible during low tide and frequently used for recreational purposes (Carbajal-Martínez et al., 2020), like sand excavation to create natural thermal water pools (Figure 6.1).

In general, flow of cold groundwater is driven by elevation gradients, with water flowing from topographic highs to low points, including the coastal zone (Hubbert, 1940). However, the exfiltration of thermal water requires a more complex mechanism involving deep circulation of water through permeable fracture and fault networks in crystalline basements (Alt-Epping et al., 2022). The depth of water penetration places limits on the maximum temperature of the resulting thermal anomalies including the discharge temperature of thermal springs at the surface (Diamond et al., 2018). Previous studies indicate that in coastal geothermal systems, seawater mixes with thermal water upflowing within fault zones (Lynn, 1978; Magri et al., 2012).

Coastal geothermal systems reach average temperatures of ~50 °C on the beach surface, a neutral pH, and on average a salinity only a third of that seawater (Carbajal-Martínez et al., 2020). Examples include La Jolla Beach (Mexico), Hot Water Beach (New Zealand), Ibusuki Beach (Japan), Rocky Point Hot Springs (United States), and Doğanbey Burnu (Turkey) (see Supplementary information for details). These systems share common characteristics, including high topographic relief (>500 m), the presence of regional strike-slip and/or normal faults running perpendicular to the coastline and likely extending offshore (Figure 6.3).

One of the most extensively studied coastal geothermal systems is La Jolla Beach (Vidal et al., 1981; Arango-Galván et al., 2011; Carbajal-Martínez et al., 2020, 2023). This system lacks any magmatic heat source, yet temperatures as high as 94 °C have been recorded just 20 cm below the sand surface. The geothermal anomaly extends approximately 250 m in length parallel to the coastline and spans 100 m in width. However, at a depth of ~60 m, the anomaly expands to over 500 m from the coastline. Seawater contributes significantly to the

hot water discharge, accounting for 15% to 50% of the total discharge. The estimated quartz equilibration temperature of the thermal fluid is 160 °C suggesting an infiltration depth of meteoric water of at least 6 km.

The conceptual model for this system suggests that meteoric water from the adjacent mountainous region dominates the thermal water. Meteoric water infiltrates through fractures and circulates at significant depths along the Agua Blanca Fault. Simultaneously, seawater infiltrates along the fault zone giving rise to a transition zone beneath the coastal area where heated meteoric water and seawater ascend (Carbajal-Martínez et al., 2020, 2023).

While several important processes have been identified at specific coastal geothermal springs, such as the infiltration of meteoric water and seawater along fault zones, their subsequent mixing, and the heating caused by the geothermal gradient, followed by their rising at coastal zones (Lynn, 1978; Shalev et al., 2007; Magri et al., 2012; Carbajal-Martínez et al., 2020, 2023), the global distribution of these systems and the key factors governing their formation and behavior have not been explained. The present study employs 3D thermal–hydraulic simulations to investigate these factors, based on a generic geological model of a coastal area crosscut by a deep-reaching, permeable fault.

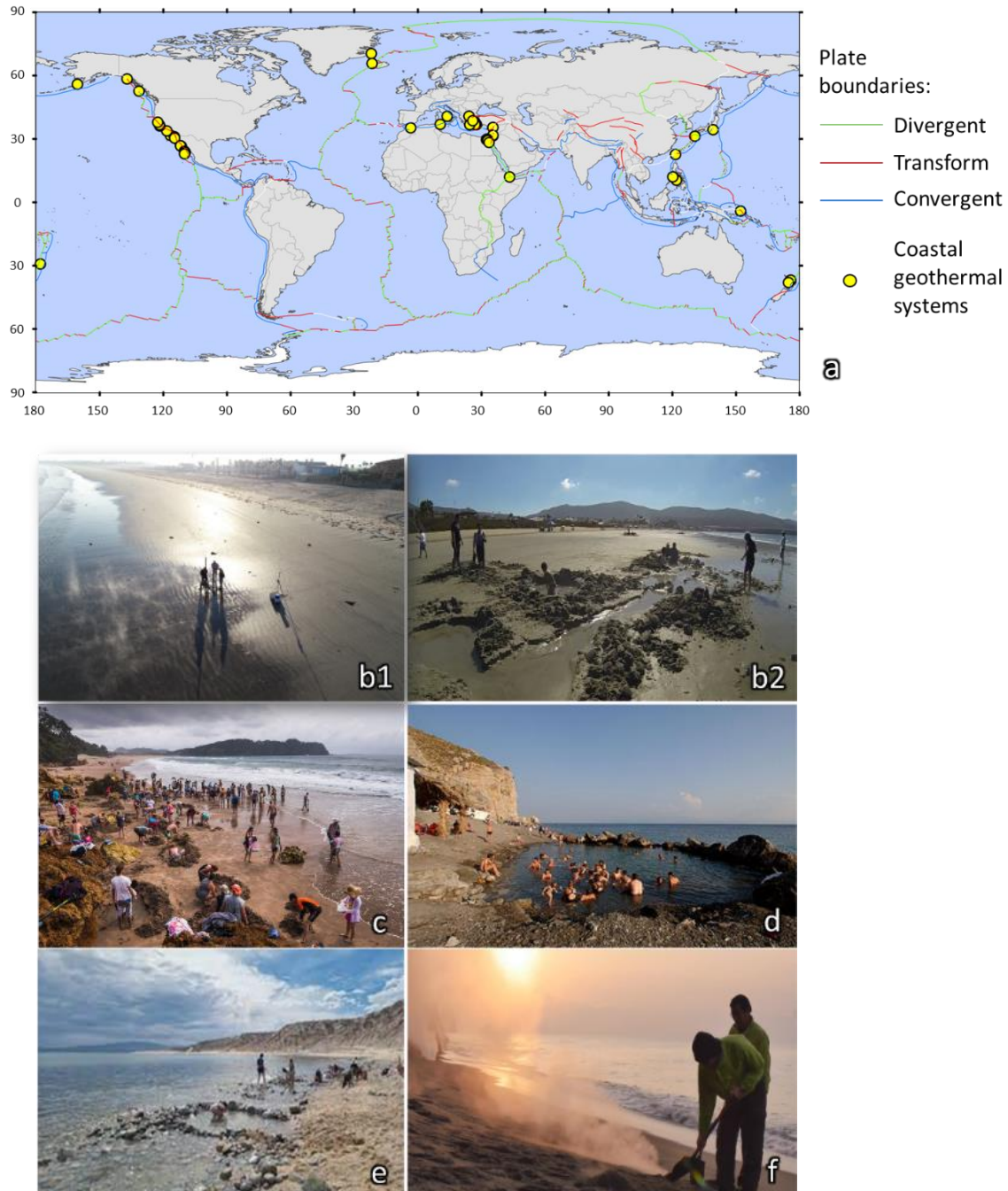


Figure 6.1. Coastal geothermal systems worldwide. (a) Map showing the multiple occurrences of coastal geothermal systems worldwide. Plates boundaries taken from [Bird \(2003\)](#). (b)-(f) Pictures of coastal thermal manifestations used for recreational purposes. (b₁-b₂) La Jolla Beach, Mexico; (c) Hot water Beach, New Zealand; (d) Therma Beach, Greece; (e) El Sargento Beach, Mexico; (f) Ibusuki Beach, Japan.

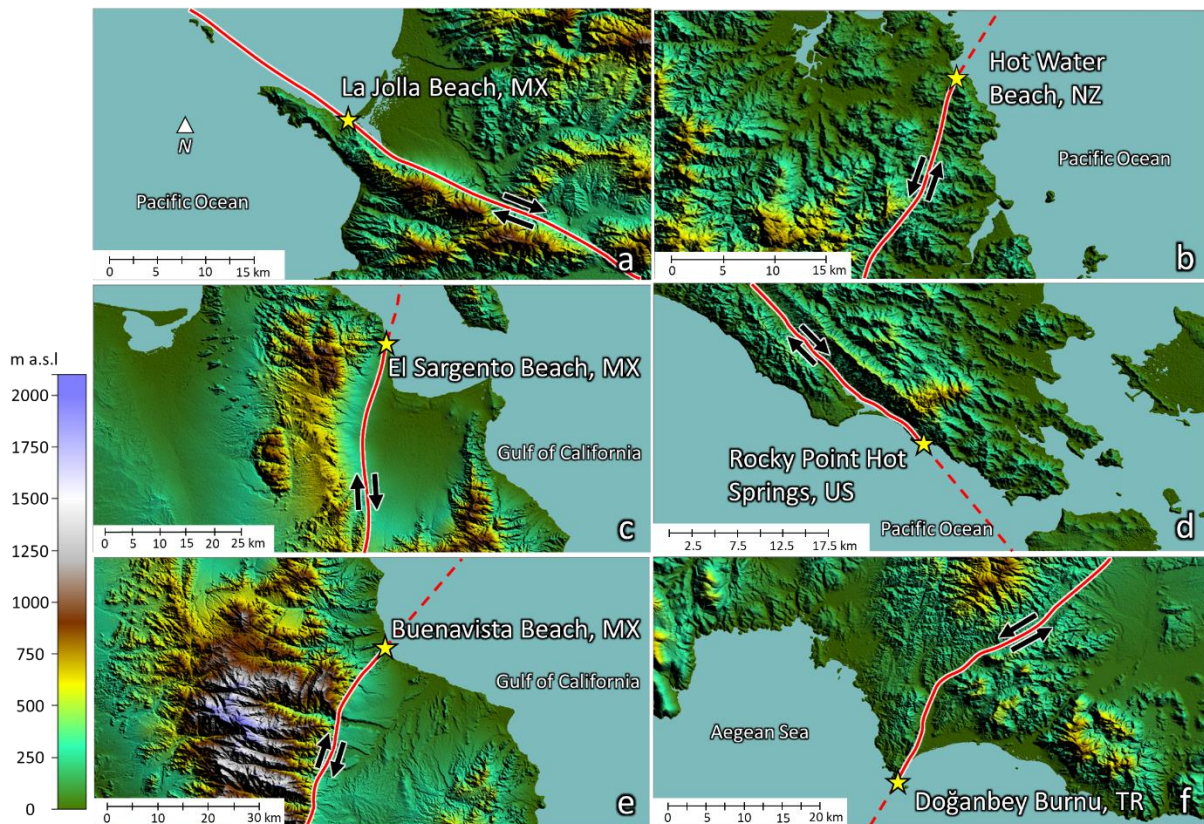


Figure 6.2. Topography and fault zones at coastal geothermal systems (yellow stars).

6.2. Model setup

To replicate the manifestations of coastal geothermal systems, including their location, temperature (~ 50 °C) and seawater fraction (15–50%), we built a large-scale 3D model (Figure 3a; see methods for more detail) with a simplified geometry (Figure 6.2a). We assume a vertical fault zone of 50 m width that divides the subaerial topography into two regions: a first one with elevations up to 1 km and a second one with lower elevations up to ~ 330 m. The seafloor deepens away from the coast, reaching 1 km below sea level. Below these surfaces the model is composed of homogeneous bedrock, with or without a wedge of capping sediments. The thermal–hydraulic properties of these model rocks are given in Table 6.1. The recharge rate of meteoric water into the mountainous hinterland is held constant, so that the fault plane below the land surface is saturated with water.

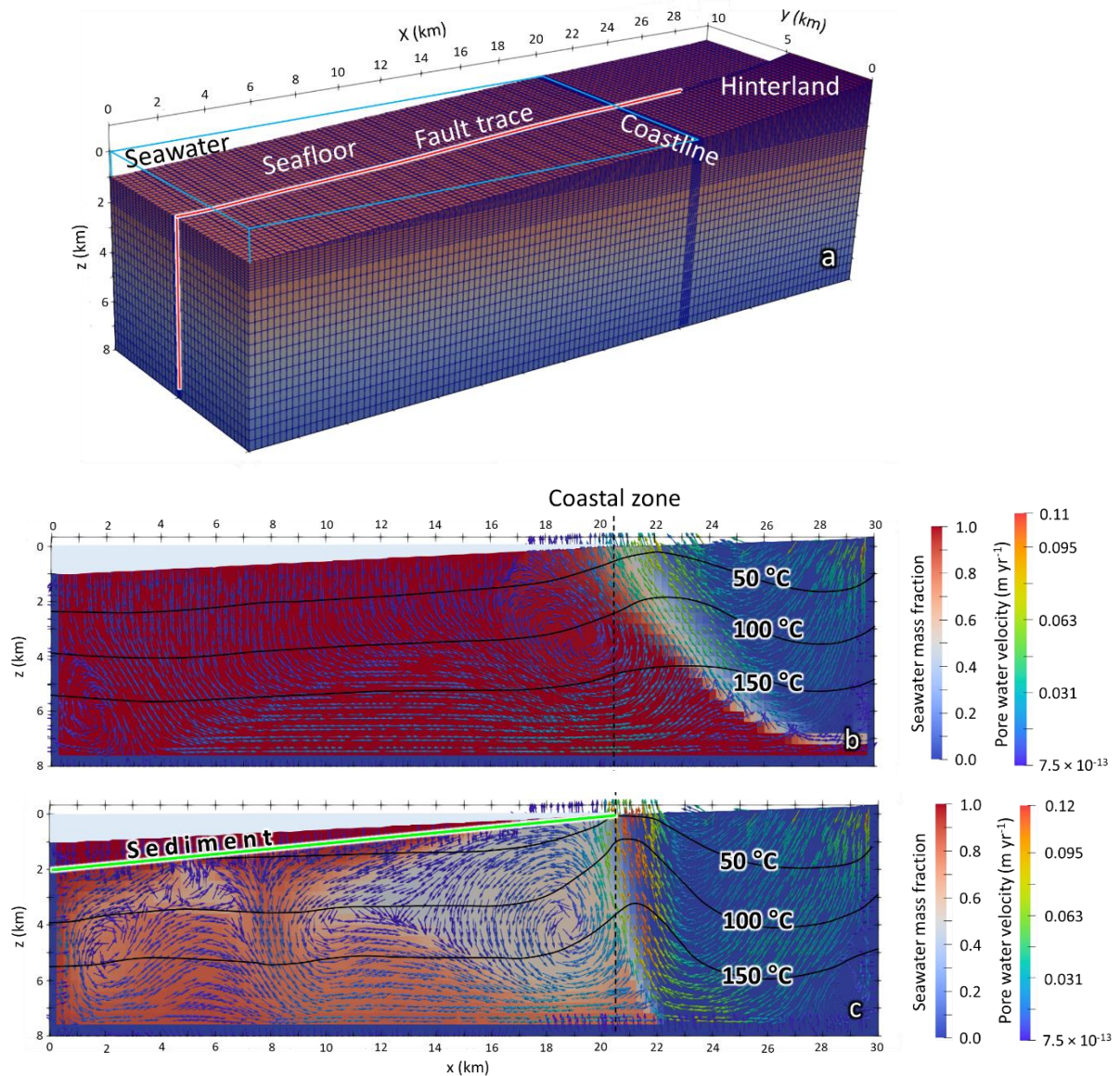


Figure 6.3. Results of 3D thermal–hydraulic simulations of coastal geothermal systems showing zones of seawater–meteoric water mixing below the coastline. (a) 3D model setup of a bedrock block (30 × 10 × 9 km) cut by a vertical fault (red trace) perpendicular to the coastline; (b) Vertical view of simulated fluid mixing within the fault plane showing steady-state temperature (black isotherms), fraction of seawater (blue to red areas), and fluid flow velocity (coloured arrows) for a scenario without a sediment layer ($k_{Fault} = 4 \times 10^{-14} \text{ m}^2$); (c) Simulated distribution of the same parameters as in panel b for a scenario including a wedge of submarine sediments reaching 1 km in thickness (green line marks sediment–bedrock contact; $k_{Sed.} = 1 \times 10^{-16} \text{ m}^2$, $k_{fault sed.} = 3 \times 10^{-16} \text{ m}^2$, $k_{fault} = 4 \times 10^{-14} \text{ m}^2$).

Table 6.1

Rock properties for replicating geothermal systems at ~50 °C in the coastal zone.

Properties	Fault	Bed-rock	Seafloor sediments	Sediments along the fault zone
Permeability (m ²)	4×10^{-14}	10^{-17}	10^{-16}	3×10^{-16}
Porosity	0.02	0.01	0.25	0.25
Thermal conductivity (W K ⁻¹ m ⁻¹)	3.34	3.34	1.5	1.5
Heat capacity (J K ⁻¹ kg ⁻¹)	920	920	800	800

Steady-state flow conditions along the model fault plane are displayed in Figure 6b. In order to match the observed characteristics of the coastal geothermal systems, we performed a sensitivity analysis by varying the fault permeability (k_{fault}) within the range of 1×10^{-14} to 8×10^{-14} m². This analysis demonstrates that increasing the permeability of the fault increases both the spring temperatures (Figure 6.4a) and the landward incursion of seawater beyond the coastline (Figure 6.4b). To achieve surface temperatures ranging from 35–55 °C, as found in natural systems, it is necessary to set k_{fault} within a narrow range of 4×10^{-14} to 5×10^{-14} m².

6.3. Seawater as a hydraulic barrier

Figure 6.3b shows that both seawater and meteoric water convect to significant depths within the fault plane (>4 km), allowing the waters to acquire heat from their wall rocks. An upflow zone develops where the two convection cells impinge and mix, bringing hot water of intermediate salinity to the surface. The location of the upflow zone approximately beneath the coastline is due to the strong contrast in density and viscosity, and hence pressure, between the two waters. Essentially, the seawater acts as a hydraulic barrier, stalling the deep seaward flow of meteoric-derived groundwater that is driven by the high elevation of its recharge zone in the hinterland. In this scenario the hottest waters in the upflow zone discharge around 2 km inland (Figure 6.4a). Thus, while this simulation reproduces the temperature observed in coastal geothermal springs, it does not replicate their location precisely. The landward incursion of seawater arises from the balance of infiltration rates of

the two waters: the resulting pressure of the convecting seawater outweighs that imposed on the meteoric water by the mountainous terrain.

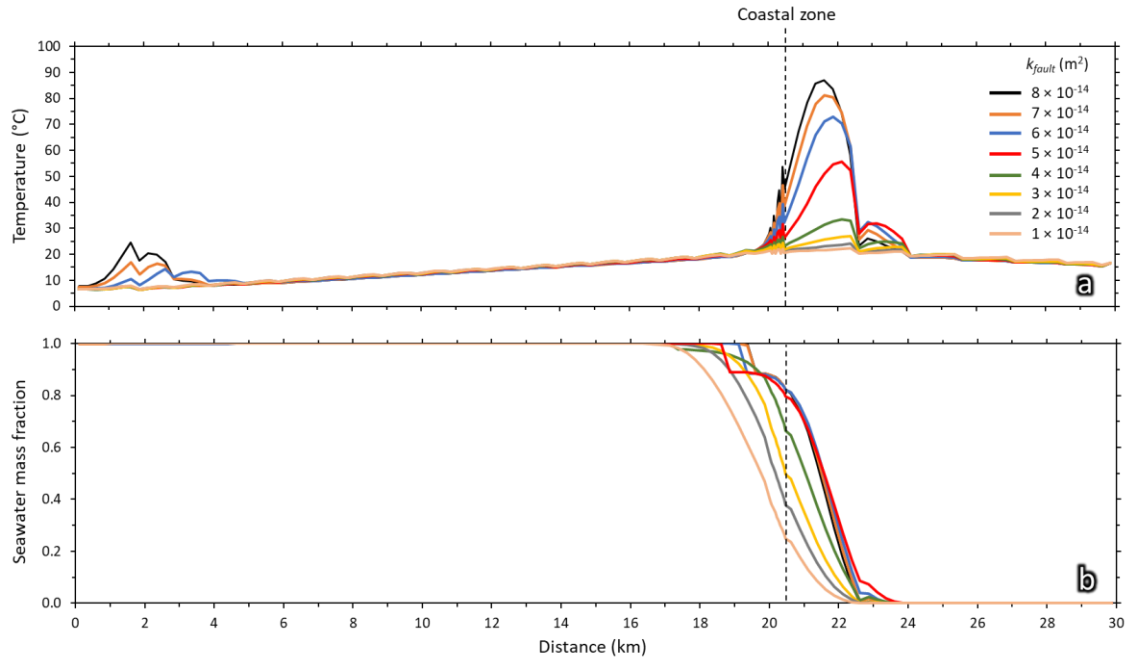


Figure 6.4. Sensitivity analysis of the fault permeability for the scenario without seafloor sediments. (a) Surface temperature profiles along the fault plane, showing that the thermal anomaly is always situated at the same location, a few kilometers inland from the coastline. (b) Profiles of seawater fractions in the thermal springs.

6.4. Influence of seafloor sediments

As alluded to above, the balance of water infiltration rates into the fault plane, and hence the precise position of the thermal upflow zone, can be shifted towards the coastline by preferentially slowing down recharge of seawater. Some faults that cross-cut a coastline may have lower permeabilities in their offshore segments than in their onshore segments. This is unlikely to be a global rule, however, if consolidated bedrock is considered to be the only wall rock of the faults. In fact, clastic sediments typically blanket the offshore segments of faults, and these are known to retard infiltration of seawater into the subsurface. The permeability of clastic sediments decreases as their particle size gets smaller and as they are compacted by increasing ocean depth (Dutkiewicz; et al., 2016). For instance, the permeability of well sorted marine sands fall within the range of $10^{-16} m^2$ to $10^{-11} m^2$, whereas

silt and clay-rich muds vary from about 10^{-17} m^2 to 10^{-15} m^2 (Snelgrove & Forster, 1996; Dutkiewicz; et al., 2016; Luijendijk & Gleeson, 2017). Sand–clay mixtures are typically found close to eroding landmasses at relatively shallow water depths, generally less than 0.5 km (Diesing, 2020).

To examine the thermal–hydraulic influence of a sediment layer above the offshore fault trace, we incorporated into our model a wedge of isotropic, clay–sand sediment with a permeability of 10^{-16} m^2 (Figure 6.3c). This wedge thickens seaward from the coastline, reaching 1 km thickness at a depth of 1 km below sea level. Our numerical sensitivity analyses have shown that seawater can still penetrate beneath the seafloor at this low permeability value. However, if their permeabilities are lower than $4 \times 10^{-17} \text{ m}^2$, the sediments act as effective hydraulic seals, preventing deep subseafloor circulation (Snelgrove & Forster, 1996).

With the above isotropic sediment wedge in the model, our simulations reproduce the observed location of the thermal springs precisely at the coastline (Figure 6.5a). However, they fail to reproduce the observed seawater fraction of 15–50% in the discharging water (Figure 6.5b). To address this issue, we conducted sensitivity simulations by varying the permeability of the sediments capping the fault (Figure 6.5; $k_{\text{fault sed.}} = 1 \times 10^{-16} - 4 \times 10^{-14} \text{ m}^2$), while maintaining the original sediment permeability elsewhere on the seafloor. This scenario reflects the possibility that the sediment cap is broken by fault scarps, thereby rendering the fault trace more permeable. The sensitivity analysis reveals that the sediments intersected by the fault plane must exhibit a permeability three times higher ($\geq 3 \times 10^{-16} \text{ m}^2$) than those elsewhere in order to replicate the observed seawater fractions of 15–50% in coastal geothermal springs. However, the position of the surface thermal anomaly begins to shift inland when the permeability exceeds $4 \times 10^{-16} \text{ m}^2$ (Figure 6.5).

Comparison of Figures 6.3b and 6.3c shows that the presence of seafloor sediments decreases the flux of seawater into the fault plane. This reduced infiltration leads to a drop in hydraulic pressure compared to simulations lacking sediment layers (Figure 6.3b). This shift in pressure dynamics relocates the upflow zone of thermal water seaward. For the simulation shown in Figure 6.3c, the surface discharge zone is now precisely located at the coastline.

Except for the location of the upflow zone, the thermal–hydraulic features of Figure

6.3c, including the impinging convection cells of seawater and meteoric-derived groundwater, are similar to those in the sediment-free scenario (Figure 6.3b). Thus, the most realistic generic simulation involves seafloor permeabilities along the fault trace of $\geq 3 \times 10^{-16} \text{ m}^2$, leading to springs in the littoral zone with temperatures of $\sim 50 \text{ }^\circ\text{C}$ and seawater fractions of 15–50% (Figure 6.5).

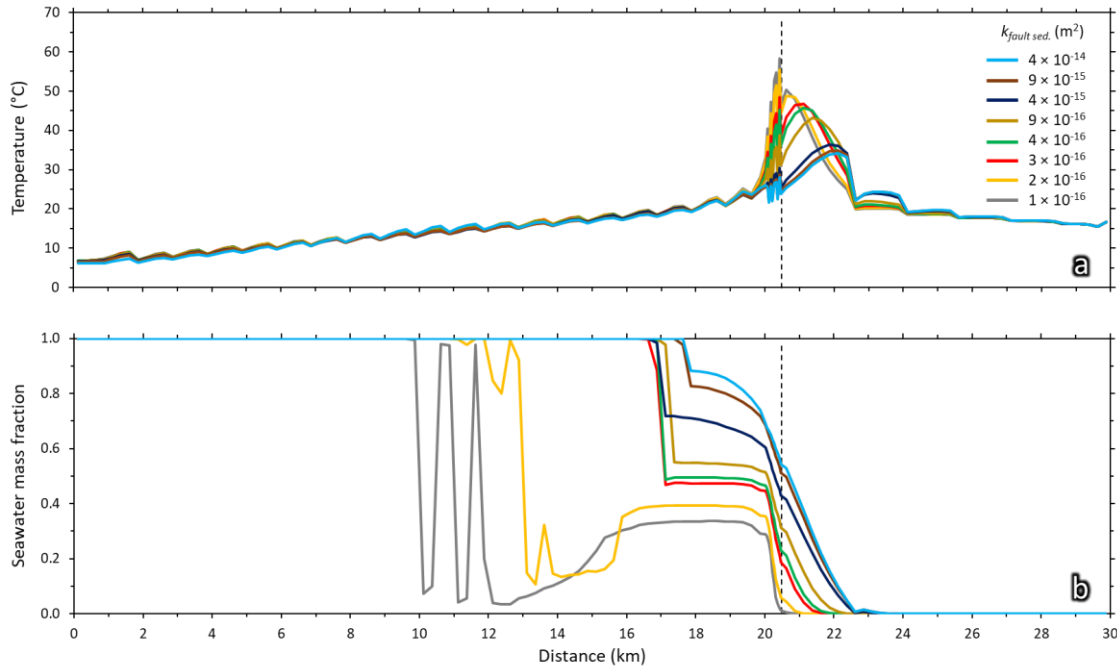


Figure 6.5. Sensitivity analysis of the permeability of the sediments capping the fault. (a) Surface temperature profile along the fault trace, showing that the thermal anomaly is always located at the coastline (dotted line); (b) Profiles of seawater fractions, demonstrating that the observed seawater fraction (15–50%) is attained when the sediment permeability is $\geq 3 \times 10^{-16} \text{ m}^2$. The permeability within the fault plane below the sediments is $4 \times 10^{-14} \text{ m}^2$.

6.5. Conclusion

The occurrence and behavior of multiple thermal water discharges along coastal zones are controlled by the infiltration of seawater and meteoric water, driven by both the topography and seawater column. This process results in three-dimensional water flow systems, which

are focused within regional and permeable fault zones. Such settings facilitate the deep infiltration of water into the subsurface. During infiltration, water is heated by the geothermal gradient, leading to the formation of an upflow zone that eventually discharges as thermal springs at the coastline. The globally systematic location of the upflow zones precisely below ocean beaches is due to the interplay of three main factors: (i) the permeability of the fault plane; (ii) the density and viscosity of ocean water, which acts as a hydraulic barrier to seaward flow of meteoric groundwater; and (iii) the presence of low-permeability marine sediments (fine-grained clay-sand mixtures) that overlie the offshore fault trace, decreasing the rate of seawater infiltration into the fault plane.

Understanding these processes is essential to improve the exploration and utilization of coastal geothermal systems, where upwelling thermal water carries substantial geothermal energy. In addition to the thermal water discharges themselves, another source of energy sits in the wider plumes of hot rock that surround the upflow zones. Our simulations show that, for high upflow rates, the temperature threshold for power production (~ 120 °C) can be attained in these plumes at less than 2 km depth (Figure 6.3c). However, the exploitation of these petrothermal heat reservoirs would require hydraulic stimulation, which at present is still technically challenging.

Overall, in view of their global occurrences, hot springs on ocean beaches should become targets for future exploration for sustainable geothermal energy production.

Acknowledgements

Carbajal-Martínez thanks the Swiss Government Excellence Scholarship (FCS) for funding his PhD in Earth Sciences at the University of Bern.

Supplementary data

All simulation input files and supplementary information on which this research is based are publicly available at the Zenodo repository (<https://doi.org/10.5281/zenodo.8380163>).

6.6. Methods

In this section, we outline the methodology employed for our forward-coupled thermal–hydraulic numerical simulations using TOUGHRECT V. 4.13. This software incorporates temperature-dependent properties of water, including viscosity, density, and enthalpy, utilizing steam table equations provided by the [International Formulation Committee \(1967\)](#). The code employs Newton–Raphson iterations to solve partial differential equations governing mass balance and heat flow ([Pruess et al., 1999](#)):

$$\frac{\partial M^{W,H}}{\partial t} = -\text{div}\mathbf{F}^{W,H} + q^{W,H} \quad (6.1)$$

where $M^{W,H}$ is the total mass accumulation term of water (W) and heat (H) within the system. $F^{W,H}$ is the total mass flux rate for water ($\text{kg m}^{-2} \text{s}^{-1}$) and heat ($\text{J m}^{-2} \text{s}^{-1}$). The equation balances the inflow and outflow of water and heat, accounting for any sources or sinks ($q^{W,H}$).

For the present fully saturated, single-phase flow case, the parameter \mathbf{F}^W is equal to the Darcy flux, denoted as u (m s^{-1}):

$$u = -\frac{k}{\mu}(\nabla P - \rho g) \quad (6.2)$$

where k (m^2) is the intrinsic permeability of the rock and μ (Pa s) is the dynamic viscosity of water. The term ∇P (Pa m^{-1}) represents the hydraulic head gradient, while ρ is the density of water (kg m^{-3}), and g is the gravitational acceleration vector (m s^{-2}).

On other hand, the heat flux ($\text{J s}^{-1} \text{m}^{-2}$) includes both conductive and convective heat components in the porous medium:

$$\mathbf{F}^H = C_M T \rho_M u - \lambda \nabla T \quad (6.3)$$

where C_M ($\text{J kg}^{-1} \text{K}^{-1}$) and ρ_M (kg m^{-3}) denote the specific heat capacity and the density of the saturated porous medium, respectively. The variable T (K) is the temperature of the porous medium, and λ corresponds to the thermal conductivity of the wet rock ($\text{J s}^{-1} \text{m}^{-1} \text{K}^{-1}$). The gradient in temperature between adjacent grid blocks is defined as ∇T (K m^{-1}). The porous medium parameters C_M and ρ_M are calculated as:

$$C_M = (1 - \phi)C_R + \phi C_w \quad (6.4)$$

$$\rho_M = (1 - \phi)\rho_R + \phi\rho_w \quad (6.5)$$

where \emptyset represents the porosity, C_R and C_w stand for the specific heat capacity of rock and water, respectively ($\text{J kg}^{-1} \text{K}^{-1}$), and ρ_w and ρ_R denote the density of rock and water, respectively (kg m^{-3}).

In order to accurately model the mixing of meteoric water and seawater, all simulations in this study utilized the EOS7 equation of state. This represents the aqueous phase as a mixture of pure water and brine (seawater) endmembers. The salinity of the mixture is represented by the mass fraction of brine (X_b). The density of the mixture (ρ_m) can then be expressed in terms of water density (ρ_w) and seawater density (ρ_b) as follows:

$$1/(\rho_m) = (1 - X_b)/(\rho_w) + (X_b/\rho_b) \quad (6.6)$$

Values of ρ_m are calculated as a function of P and T via EOS7.

Effects of salinity on the viscosity of the aqueous phase are modeled with a polynomial correction to the viscosity of pure water (μ_w). Thus, the viscosity of the mixture (μ_m) is represented as follows:

$$\mu_m(P, T, X_b) = \mu_w(P, T) f(X_b) \quad (6.7)$$

where

$$f(X_b) = 1 + 0.066X_b \quad (6.8)$$

6.6.1. Model description and initial and boundary conditions

Our numerical model is a large 3D domain measuring $30 \times 10 \times 9$ km (Figure 6.3a). The model was initially discretized a regular rectangular mesh consisting of approximately 400,000 grid blocks. The grid block sizes vary throughout the domain, with the highest resolution ($50 \times 50 \times 50$ m) in the center of the model domain in the coastal zone. The model includes the seafloor on the left side (0–20.5 km) and the mountainous zone on the right side, with the coastline at 20.5 km. To represent topography (up to 1 km) and bathymetry (up to 1 km), we used the elevation as a basis for shaping the surface of the initial regular mesh, creating a 3D irregular mesh using the "fit surface" method available in the PyTOUGH software (Croucher, 2015).

The model domain was assigned initial fixed boundary conditions for pressure and temperature to define hydrostatic pressure and conductive temperature distributions as initial condition within the model domain. At the upper boundary, a fixed temperature was assigned

based on an ambient temperature of 16 °C at the coast. Over the continent, the temperature according to its elevation using an adiabatic cooling rate of $-5.5 \text{ }^\circ\text{C km}^{-1}$, and the temperature of the seafloor was set using a cooling gradient of $-3.1 \text{ }^\circ\text{C per 100 m depth below sea level}$ (Emery & Dewar, 1982).

In all the simulations, the land surface was set to be saturated with meteoric water, providing unlimited infiltration. To define the fluid pressure of rainwater at the land surface ($P_{f,land\ surface}$; Pa), we utilized Equation 6.9 (Cavcar, 2000) which gives the atmospheric pressure as a function of elevation above sea level (z):

$$P_{f,land\ surface} = 10^5 [1 - (0.0065z / 289.15)]^{5.2561} \quad (6.9)$$

On other hand, the fluid pressure at the seafloor ($P_{f,seafloor}$; Pa) was determined based on the height of the seawater column (h), the seawater density ($\rho_b = 1025 \text{ kg m}^{-3}$), and the acceleration due to gravity (g ; m s^{-2}):

$$P_{f,seafloor} = \rho_b g h \quad (6.10)$$

To specify a conductive temperature distribution as initial condition, we used regional geothermal gradient of $25 \text{ }^\circ\text{C km}^{-1}$. At the lower model boundary this resulted in temperature of $225 \text{ }^\circ\text{C}$. During the simulations, the four lateral and lower boundaries were open for conductive heat exchange and closed for fluid flow. The upper boundary, on the other hand, was open for both heat and fluid flow. The simulations were executed for a simulation time of 1,000,000 years to achieve a steady state.

Part 3: Concluding remarks

7. Conclusions

The research described in this thesis was conducted via a multidisciplinary approach that integrates geochemical, geophysical, and geological data with quantitative 3D thermal–hydraulic simulations using the TOUGH software. The focus was placed on the amagmatic geothermal systems that occur along the Agua Blanca Fault (ABF) in Baja California, Mexico. This short concluding Chapter summarizes the main findings and insights that enhance our comprehension of the key parameters governing the behavior of such amagmatic orogenic geothermal systems.

Amagmatic orogenic geothermal systems derive their heat from deep-seated bedrocks characterized by normal geothermal gradients (20–35 °C/km), rather than from rocks directly heated by magma bodies. The heat carrier is meteoric water that infiltrates deep into major fault systems, such as the ABF, in response to high hydraulic head gradients generated by rugged mountainous topography. Along the deep flow path, the meteoric water undergoes substantial physical and chemical changes, including an increase in temperature, salinity, and helium content. Residence times of the water within these flow paths are typically on the order of tens of thousands of years. Along the ABF, the hottest systems (94–102 °C) discharge on the Pacific coast, precisely where degree of tectonic fault extension and fault permeability reach their maximum values. This demonstrates the key role of permeability in controlling the discharge temperature of thermal waters as well as the magnitude of the thermal anomalies generated by amagmatic geothermal systems. Moreover, the hydraulic head gradient emerges as a second critical parameter of water flow pathways, influencing the depth of infiltration, water residence times, and $^3\text{He}/\text{He}_{\text{total}}$ ratios.

La Jolla Beach, as the hottest system along the ABF, has been a major point of interest for this research. The results of our 3D thermal–hydraulic simulations reveal the interplay of a series of factors that influence the location, size, temperature, and salinity of this geothermal system. These factors are the inshore and offshore topography, fault zone geometry and permeability, the presence of subvertical preferentially permeable channels within the fault, and the topography of the contact surface between unconsolidated sediments and the crystalline basement. Sensitivity analyses have demonstrated the key role of the ocean as a hydraulic barrier, limiting the circulation of meteoric water beyond the coastline. Furthermore, the particular subsurface topography of the basement and the layer of sediments above it hinder the

infiltration of seawater, thereby controlling the precise location and extent of the La Jolla Beach system. The sensitivity analysis also demonstrates that higher permeability correlates with hotter water discharge and with higher seawater infiltration, demonstrating the importance of the local structural configuration in influencing fluid flow behavior.

The exceptionally high discharge temperature observed at La Jolla Beach –a world record to our knowledge– is caused by the spatial coincidence of two key features: 1) Its position right along the beachfront is due to an underlying upflow area created by the convergence of seaward-moving rainwater and landward-moving seawater; 2) the active ABF plane and the inferred presence of a subvertical permeable anomaly within the fault directly beneath the beach. This anomaly acts like a narrow 1D tube, allowing very high upflow rates. Without this preferential conduit, discharges temperatures would be significantly lower (e.g., ~50 °C).

The focus on understanding the dynamics of the ABF in Mexico prompted our literature search for other similar systems worldwide. This revealed that analogous hot springs on ocean beaches are a global phenomenon. In all the 61 cases found, steeply dipping faults cut across a rugged inland topography, intersecting the coastline and continuing offshore for some distance. Our generic modelling of these systems was inspired by the key factors that drive the La Jolla geothermal system. The average discharge temperatures of the worldwide occurrences are around 50 °C, which means that no preferentially permeable conduits need to be invoked to explain their dynamics. Instead, the systems can be well accounted for by the impinging convection cells of the type and geometry identified at La Jolla, provided offshore sediments dampen the recharge of seawater into the host faults.

The results of this thesis suggest that the most promising amagmatic systems for the exploitation of geothermal energy occur where strong hydraulic head gradients for meteoric water coincide with the traces of major fault zones. This leads to hot spring discharges at the low points of the gradients, for instance where the host faults intersect valley floors or the coastline. Under such conditions, thermal anomalies can be generated where the temperature threshold of approximately 120 °C for electricity production is reached in less than 2 km depth. Thus, the research findings described in this thesis advance our understanding of amagmatic orogenic geothermal systems and thereby promote their use as sustainable energy sources.

References

- Allen, C. R., Silver, L. T., & Stehli, F. G. (1960). Agua Blanca fault - A major transverse structure of northern Baja California, Mexico. *Bulletin of the Geological Society of America*, 71(4), 467–482. [https://doi.org/10.1130/0016-7606\(1960\)71\[467:ABFMTS\]2.0.CO;2](https://doi.org/10.1130/0016-7606(1960)71[467:ABFMTS]2.0.CO;2)
- Alt-Epping, P., Diamond, L. W., Wanner, C., & Hammond, G. E. (2021). Effect of Glacial/Interglacial Recharge Conditions on Flow of Meteoric Water Through Deep Orogenic Faults: Insights Into the Geothermal System at Grimsel Pass, Switzerland. *Journal of Geophysical Research: Solid Earth*, 126(7), 1–21. <https://doi.org/10.1029/2020JB021271>
- Alt-Epping, P., Diamond, L. W., & Wanner, C. (2022). Permeability and groundwater flow dynamics in deep-reaching orogenic faults estimated from regional-scale hydraulic simulations. *Geochemistry, Geophysics, Geosystems*. <https://doi.org/10.1029/2022gc0110512>
- Andrews, J. N., & Lee, D. J. (1979). Inert gases in groundwater from the Bunter Sandstone of England as indicators of age and palaeoclimatic trends. *Journal of Hydrology*, 41(3–4), 233–252. [https://doi.org/10.1016/0022-1694\(79\)90064-7](https://doi.org/10.1016/0022-1694(79)90064-7)
- Arango-Galván, C., Prol-Ledesma, R. M., Flores-Márquez, E. L., Canet, C., & Villanueva Estrada, R. E. (2011). Shallow submarine and subaerial, low-enthalpy hydrothermal manifestations in Punta Banda, Baja California, Mexico: Geophysical and geochemical characterization. *Geothermics*, 40(2), 102–111. <https://doi.org/10.1016/j.geothermics.2011.03.002>
- Arnorsson, S. (1975). Application of the Silica Geothermometer in Low Temperature Hydrothermal Areas in Iceland. *Am J Sci*. <https://doi.org/10.2475/ajs.275.7.763>
- Asta, M. P., Gimeno, M. J., Auqué, L. F., Gómez, J., Acero, P., & Lapuente, P. (2010). Secondary processes determining the pH of alkaline waters in crystalline rock systems. *Chemical Geology*, 276(1–2), 41–52. <https://doi.org/10.1016/j.chemgeo.2010.05.019>
- Barry, P. H., Negrete-Aranda, R., Spelz, R. M., Seltzer, A. M., Bekaert, D. V., Virrueta, C., & Kulongoski, J. T. (2020). Volatile sources, sinks and pathways: A helium-carbon isotope study of Baja California fluids and gases. *Chemical Geology*, 550(May), 119722. <https://doi.org/10.1016/j.chemgeo.2020.119722>

- Batista Cruz, R. Y., Rizzo, A. L., Grassa, F., Bernard Romero, R., González Fernández, A., Kretzschmar, T. G., & Gómez-Arias, E. (2019). Mantle Degassing Through Continental Crust Triggered by Active Faults: The Case of the Baja California Peninsula, Mexico. *Geochemistry, Geophysics, Geosystems*, 20(4), 1912–1936.
<https://doi.org/10.1029/2018GC007987>
- Bear, J. (2013). *Dynamics of fluids in porous media*. (Courier Corporation, Ed.).
- Belgrano, T. M., Herwegh, M., & Berger, A. (2016). Inherited structural controls on fault geometry, architecture and hydrothermal activity: an example from Grimsel Pass, Switzerland. *Swiss Journal of Geosciences*, 109(3), 345–364.
<https://doi.org/10.1007/s00015-016-0212-9>
- Beltrán-Abaunza, J. M., & Quintanilla-Montoya, A. L. (2001). Calculated heat flow for the Ensenada region, Baja California, Mexico. *Ciencias Marinas*, 27(4), 619–634.
- Bergman, T. L. (2011). *Fundamentals of Heat and Mass Transfer*. (John Wiley & Sons., Ed.).
- Bird, P. (2003). An updated digital model of plate boundaries. *Geochemistry, Geophysics, Geosystems*, 4(3). <https://doi.org/10.1029/2001GC000252>
- Bonner, J. L., Blackwell, D. D., & Herrin, E. T. (2003). Thermal constraints on earthquake depths in California. *Bulletin of the Seismological Society of America*, 93(6), 2333–2354.
<https://doi.org/10.1785/0120030041>
- Brodi, B. (1996). Thermal state, rheology and seismicity in the Pannonian Basin, Hungary. *Journal of Geodynamics*, 21(4), 309–328. [https://doi.org/10.1016/0264-3707\(96\)00002-6](https://doi.org/10.1016/0264-3707(96)00002-6)
- Brodi, B., & Iizuka, S. (1993a). Earthquake cutoff depth as a possible geothermometer-applications to central Japan. *Tectonophysics*, 225(1–2), 63–78.
[https://doi.org/10.1016/0040-1951\(93\)90249-J](https://doi.org/10.1016/0040-1951(93)90249-J)
- Brodi, B., & Iizuka, S. (1993b). On possible rheological constraints on lithosphere geothermal models. *Geodynamic*, 17(1), 77–92.
- Byerlee, J. (1978). Friction of rocks. *Pure and Applied Geophysics PAGEOPH*, 116(4–5), 615–626. <https://doi.org/10.1007/BF00876528>
- Caine, J. S., & Forster, C. B. (1999). Fault Zone Architecture and Fluid Flow : Insights from Field Data and Numerical Modeling. In *Faults and subsurface fluid flow in the shallow crust*. (pp. 100–127). American Geophysical Union.
<https://doi.org/10.1029/GM113p0101>
- Caine, J. S., Evans, J. P., & Forster, C. B. (1996). Fault zone architecture and permeability

- structure. *Geology*, 24(11), 1025–1028. [https://doi.org/10.1130/0091-7613\(1996\)024<1025:FZAAPS>2.3.CO;2](https://doi.org/10.1130/0091-7613(1996)024<1025:FZAAPS>2.3.CO;2)
- Camprubí, A., Canet, C., Rodríguez-Díaz, A. A., Prol-Ledesma, R. M., Blanco-Florido, D., Villanueva, R. E., & López-Sánchez, A. (2008). Geology, ore deposits and hydrothermal venting in Bahía Concepción, Baja California Sur, Mexico. *Island Arc*, 17(1), 6–25. <https://doi.org/10.1111/j.1440-1738.2007.00586.x>
- Capasso, G., & Inguaggiato, S. (1998). A simple method for the determination of dissolved gases in natural waters. An application to thermal waters from Vulcano Island. *Applied Geochemistry*, 13(5), 631–642. [https://doi.org/10.1016/S0883-2927\(97\)00109-1](https://doi.org/10.1016/S0883-2927(97)00109-1)
- Carbajal-Martínez, D. (2019). *Exploración geotérmica en el municipio de Ensenada, Baja California, mediante métodos geoquímicos y geofísicos*. Tesis de Maestría en Ciencias. Centro de Investigación Científica y de Educación Superior de Ensenada, Baja California. 125 pp.
- Carbajal-Martínez, D., Peiffer, L., Hinojosa-Corona, A., Trasviña-Castro, A., Arregui-Ojeda, S. M., Carranza-Chávez, F. J., et al. (2020). UAV-based thermal imaging and heat output estimation of a coastal geothermal resource: La Jolla beach, Baja California, Mexico. *Renewable Energy*, 168. <https://doi.org/10.1016/j.renene.2020.12.113>
- Carbajal-Martínez, D., Wanner, C., Diamond, L. W., & Peiffer, L. (2023). Behavior of amagmatic orogenic geothermal systems: insights from the Agua Blanca Fault, Baja California, Mexico. *Submitted to Geochemistry, Geophysics, Geosystems, July 2023*.
- Castillo, P. R., Hawkins, J. W., Lonsdale, P. F., Hilton, D. R., Shaw, A. M., & Glascock, M. D. (2002). Petrology of Alarcon Rise lavas, Gulf of California: Nascent intracontinental ocean crust. *Journal of Geophysical Research: Solid Earth*, 107(B10), ECV 5-1-ECV 5-15. <https://doi.org/10.1029/2001jb000666>
- Cavcar, M. (2000). The International Standard Atmosphere (ISA), 1–6.
- Chen, C. H. (1985). Chemical characteristics of thermal waters in the Central Range of Taiwan, R.O.C. *Chemical Geology*, 49(1–3), 303–317. [https://doi.org/10.1016/0009-2541\(85\)90163-9](https://doi.org/10.1016/0009-2541(85)90163-9)
- Chester, F. M. (1995). A rheologic model for wet crust applied to strike-slip faults. *Journal of Geophysical Research*, 100, 33–44.
- CICESE. (2019). Datos climáticos diarios del CLICOM del SMN a través de su plataforma web del CICESE. Retrieved from <http://clicom-mex.cicese.mx/>

- COP21. (2015). The Paris Agreement. Retrieved from <https://unfccc.int/process-and-meetings/the-paris-agreement>
- Coussens, J., Woodman, N., Upton, P., Menzies, C. D., Janku-Capova, L., Sutherland, R., & Teagle, D. A. H. (2018). The Significance of Heat Transport by Shallow Fluid Flow at an Active Plate Boundary: The Southern Alps, New Zealand. *Geophysical Research Letters*, *45*(19), 10,323-10,331. <https://doi.org/10.1029/2018GL078692>
- Craig, H. (1961). Isotopic Variations in Meteoric Waters. *Science (New York, N.Y.)*, *133*(3465), 1702–3. <https://doi.org/10.1126/science.133.3465.1702>
- Croucher, A. E. (2015). Recent developments in the PyTOUGH scripting library for TOUGH2 simulations. In *In Proceedings 37th New Zealand Geothermal Workshop. Taupo, New Zealand: The University of Auckland*. Retrieved from http://www.geothermalworkshop.co.nz/wp-content/uploads/NZGW2015_Programme_1511_17Nov.pdf
- Cruz Falcón, A., & Vázquez González, R. (1989). Gravimetría del Valle de Maneadero-Chapultepec, Ensenada, B.C., con aplicación a la geohidrología. *Ciencias Marinas*, *15*, 21–38.
- Daesslé, L. W., Ruiz-Montoya, L., Tobschall, H. J., Chandrajith, R., Camacho-Ibar, V. F., Mendoza-Espinosa, L. G., et al. (2009). Fluoride, nitrate and water hardness in groundwater supplied to the rural communities of Ensenada County, Baja California, Mexico. *Environmental Geology*, *58*(2), 419–429. <https://doi.org/10.1007/s00254-008-1512-9>
- Dansgaard, W. (1964). Stable isotopes in precipitation. *Tellus*, *16*(4), 436–468. <https://doi.org/10.3402/tellusa.v16i4.8993>
- Darcy, H. (1856). *The public fountains of the city of Dijon*. Victor Dalmont, Paris, France.
- Diamond, L. W., Wanner, C., & Waber, H. N. (2018). Penetration depth of meteoric water in orogenic geothermal systems. *Geology*, *46*(12), 1083–1066. <https://doi.org/10.1130/G45394.1>
- Diesing, M. (2020). Deep-sea sediments of the global ocean. *Earth System Science Data*, *12*(4), 3367–3381. <https://doi.org/10.5194/essd-12-3367-2020>
- Dragonì, M. (1993). The brittle-ductile transition in tectonic boundary zones. *Annals of Geophysics*. <https://doi.org/10.4401/ag-4282>
- Dutkiewicz, A., S., O., & Müller, R. D. (2016). Controls on the distribution of deep-sea

- sediments. *Geochemistry Geophysics Geosystems*, 17, 1312–1338.
<https://doi.org/10.1002/2015GC006205>. Received
- Emerson, D. W. (1990). Notes on Mass Properties of Rocks — Density, Porosity, Permeability. *Exploration Geophysics*, 21, 209–216.
- Emery, K.O., Gorsline, D. S., & Uch, E. (1957). Sediments of Three Bays of Baja California: Sebastian Viscaïno, San Cristobal, and Todos Santos. *SEPM Journal of Sedimentary Research*, Vol. 27(2), 95–115. <https://doi.org/10.1306/74d70669-2b21-11d7-8648000102c1865d>
- Emery, W. J., & Dewar, J. S. (1982). Mean Temperature-Salinity, Salinity-Depth and Temperature-Depth Curves for the North Atlantic and the North Pacific. *Progress in Oceanography*, 11(3), 219–256. [https://doi.org/10.1016/0079-6611\(82\)90015-5](https://doi.org/10.1016/0079-6611(82)90015-5)
- Erkan, K., & Blackwell, D. (2009). Transient thermal regimes in the Sierra Nevada and Baja California extinct outer arcs following the cessation of Farallon subduction. *Journal of Geophysical Research: Solid Earth*, 114(2), 1–18. <https://doi.org/10.1029/2007JB005498>
- Evans, J. P., Forster, C. B., & Goddard, J. V. (1997). Permeability of fault-related rocks, and implications for hydraulic structure of fault zones. *Journal of Structural Geology*, 19(11), 1393–1404. [https://doi.org/10.1016/S0191-8141\(97\)00057-6](https://doi.org/10.1016/S0191-8141(97)00057-6)
- Faulkner, D. R., Jackson, C. A. L., Lunn, R. J., Schlische, R. W., Shipton, Z. K., Wibberley, C. A. J., & Withjack, M. O. (2010). A review of recent developments concerning the structure, mechanics and fluid flow properties of fault zones. *Journal of Structural Geology*, 32(11), 1557–1575. <https://doi.org/10.1016/j.jsg.2010.06.009>
- Fournier, R. O. (1977). Chemical geothermometers and mixing models for geothermal systems. *Geothermics*, 5(1–4), 41–50. [https://doi.org/10.1016/0375-6505\(77\)90007-4](https://doi.org/10.1016/0375-6505(77)90007-4)
- Fournier, R.O., White, D. E., & Truesdell, A. H. (1973). Geochemical indicators of subsurface temperature-part 1, basic assumptions. *USGS*, 2, 259–262.
- Fournier, Robert O., & Potter, I. R. W. (1982). An equation correlating the solubility of quartz in water from 25° to 900°C at pressures up to 10,000 bars, 46, 1969–1973.
- Frez, J., Acosta, J., Nava, A., Suarez, F., Gonzalez, J., Arellano, G., et al. (2004). Microseismicity Studies in Northern Baja California, Mexico: the Agua Blanca Fault. AGU. Retrieved from <https://ui.adsabs.harvard.edu/abs/2004AGUFM.S51A0129F/abstract>
- Gastil, G., & Bertine, K. (1986). Correlation between seismicity and the distribution of thermal

- and carbonate water in southern and Baja California, United States and Mexico. *Geology*, *14*(4), 287–290. [https://doi.org/10.1130/0091-7613\(1986\)14<287:CBSATD>2.0.CO;2](https://doi.org/10.1130/0091-7613(1986)14<287:CBSATD>2.0.CO;2)
- Gastil, R. G., Phillips, R. P., & Allison, E. C. (1975). Reconnaissance geology of the state of Baja California. *Geological Society of America*, *140*, 201.
- Giggenbach, W. (1989). *Collection and analysis of geothermal and volcanic water and gas discharges* (4th ed.). Petone N.Z.: Chemistry Division Dept. of Scientific and Industrial Research. Retrieved from <https://www.worldcat.org/title/collection-and-analysis-of-geothermal-and-volcanic-water-and-gas-discharges/oclc/153677478>
- Giggenbach, W. F. (1988). Geothermal solute equilibria. derivation of Na-K-Mg-Ca geoindicators. *Geochimica et Cosmochimica Acta*, *52*(12), 2749-2765.
- Gökgöz, A., & Akdağoğlu, H. (2016). Hydrogeology and hydrogeochemistry of a coastal low-temperature geothermal field : a case study from the Datça Peninsula (SW Turkey). *Environmental Earth Sciences*, *75*, 1–18. <https://doi.org/10.1007/s12665-016-5957-y>
- Gold, P. O., Behr, W. M., Fletcher, J. M., Rockwell, T. K., & Figueiredo, P. M. (2020). Time-Invariant Late Quaternary Slip Rates Along the Agua Blanca Fault, Northern Baja California, Mexico. *Tectonics*, *39*(9), 1–26. <https://doi.org/10.1029/2019TC005788>
- Grasby, S. E., & Hutcheon, I. (2001). Controls on the distribution of thermal springs in the southern Canadian Cordillera. *Canadian Journal of Earth Sciences*, *38*(3), 427–440. <https://doi.org/10.1139/e00-091>
- Guillong, M., Meier, D. L., Allan, M. M., Heinrich, C. A., & Yardley, B. W. D. (2008). SILLS: A Matlab-Based Program for the Reduction of Laser Ablation ICP–MS Data of Homogeneous Materials and Inclusions. *Mineralogical Association of Canada Short Course*, *40*, 328–333.
- Guillou-Frottier, L., Milesi, G., Roche, V., Duwiquet, H., & Tallefer, A. (2023). Comptes Rendus Géoscience. *Comptes Rendus Géoscience*, 0–33.
- Gutiérrez-Gutiérrez, A., & Suárez-Vidal, F. (1988). Tectonic Reconstruction Of Agua Blanca Fault In The Bahia De Todos Santos, Baja California, Mexico. *Ciencias Marinas*, *14*(2), 15–28. <https://doi.org/10.7773/cm.v14i2.595>
- Hamme, R. C., & Emerson, S. R. (2004). The solubility of neon, nitrogen and argon in distilled water and seawater. *Deep-Sea Research Part I: Oceanographic Research Papers*, *51*(11), 1517–1528. <https://doi.org/10.1016/j.dsr.2004.06.009>
- Hernández-Morales, P., & Wurl, J. (2017). Hydrogeochemical characterization of the thermal

- springs in northeastern of Los Cabos Block, Baja California Sur, México. *Environmental Science and Pollution Research*, 24(15), 13184–13202. <https://doi.org/10.1007/s11356-016-8087-x>
- Hernández-Morales, P., Wurl, J., Green-Ruiz, C., & Morata, D. (2021). Hydrogeochemical characterization as a tool to recognize “masked geothermal waters” in bahía concepción, Mexico. *Resources*, 10(3), 1–24. <https://doi.org/10.3390/resources10030023>
- Hilton, D. R. (1996). The helium and carbon isotope systematics of a continental geothermal system: Results from monitoring studies at Long Valley caldera (California, U.S.A.). *Chemical Geology*, 127(4), 269–295. [https://doi.org/10.1016/0009-2541\(95\)00134-4](https://doi.org/10.1016/0009-2541(95)00134-4)
- Hubbert, K. M. (1940). The theory of ground-water motion. *Journal of Geology*, 47(8).
- Ikari, M. J., Marone, C., & Saffer, D. M. (2011). On the relation between fault strength and frictional stability. *Geology*, 39(1), 83–86. <https://doi.org/10.1130/G31416.1>
- INEGI. (2022). Continuo de Elevaciones Mexicano (CEM). Retrieved from <https://sinegi.page.link/1av6>
- Ingebritsen, S. E., & Manning, C. E. (2010). Permeability of the continental crust: Dynamic variations inferred from seismicity and metamorphism. *Geofluids*, 10(1–2), 193–205. <https://doi.org/10.1111/j.1468-8123.2010.00278.x>
- Inguaggiato, S., & Rizzo, A. (2004). Dissolved helium isotope ratios in ground-waters: A new technique based on gas-water re-equilibration and its application to Stromboli volcanic system. *Applied Geochemistry*, 19(5), 665–673. <https://doi.org/10.1016/j.apgeochem.2003.10.009>
- International Formulation Committee. (1967). *A formulation of the thermodynamic properties of ordinary water substance*.
- Jolie, E., Scott, S., Faulds, J., Chambefort, I., Axelsson, G., Gutiérrez-Negrín, L. C., et al. (2021). Geological controls on geothermal resources for power generation. *Nature Reviews Earth and Environment*, 2(5), 324–339. <https://doi.org/10.1038/s43017-021-00154-y>
- Junge, C. E., & Werby, R. T. (1958). The concentration of chloride, sodium, potassium, calcium, and sulfate in rain water over the United States. *Journal of Meteorology*, 15 (5), 417–425.
- Karasaki, K., Ito, K., Wu, Y. S., Shimo, M., Sawada, A., Maekawa, K., & Hatanaka, K. (2011). Uncertainty reduction of hydrologic models using data from surface-based

- investigation. *Journal of Hydrology*, 403(1–2), 49–57.
<https://doi.org/10.1016/j.jhydrol.2011.03.039>
- Karytsas, K., Alexandrou, V., & Boukis, I. (2002). The Kimolos Geothermal Desalination Project. *Proceedings of International Workshop on Possibilities of Geothermal Energy Development in the Aegean Islands Region*, 206–219.
- Kennedy, B. M., & Van Soest, M. C. (2007). Flow of mantle fluids through the ductile lower crust: Helium isotope trends. *Science*, 318(5855), 1433–1436.
<https://doi.org/10.1126/science.1147537>
- Kretzschmar, T. G., & Frommen, T. (2013). Stable Isotope Composition of Surface and Groundwater in Baja California, Mexico. *Procedia Earth and Planetary Science*, 7, 451–454. <https://doi.org/10.1016/j.proeps.2013.03.194>
- Kulongoski, J. T., Hilton, D. R., Cresswell, R. G., Hostetler, S., & Jacobson, G. (2008). Helium-4 characteristics of groundwaters from Central Australia: Comparative chronology with chlorine-36 and carbon-14 dating techniques. *Journal of Hydrology*, 348(1–2), 176–194. <https://doi.org/10.1016/j.jhydrol.2007.09.048>
- Lay, T., Hernlund, J., & Buffett, B. A. (2008). Core–mantle boundary heat flow. *Nature Geoscience*, 13–15.
- Lichtner, P. (1996). Continuum formulation of multicomponent-multi-phase reactive transport. *Reviews in Mineralogy*, 34, 1–81.
- López-Sánchez, A., Báncora-Alsina, C., Prol-Ledesma, R. M., & Hiriart, G. (2006). A new geothermal resource in Los Cabos, Baja California Sur, Mexico. *Proceedings 28th NZ Geothermal Workshop 2006*, (5255), pp: 6. Retrieved from <http://www.geothermal-energy.org/pdf/IGASTandard/NZGW/2006/PDF/S3.pdf>
- López, D. L., & Smith, L. (1995). Fluid Flow in Fault Zones: Analysis of the Interplay of Convective Circulation and Topographically Driven Groundwater Flow. *Water Resources Research*, 31(6), 1489–1503. <https://doi.org/10.1029/95WR00422>
- Lucazeau, F. (2019). Analysis and Mapping of an Updated Terrestrial Heat Flow Data Set. *Geochemistry, Geophysics, Geosystems*, 20(8), 4001–4024.
<https://doi.org/10.1029/2019GC008389>
- Luijendijk, E., & Gleeson, T. (2017). How well can we predict permeability in sedimentary basins? Deriving and evaluating porosity – permeability equations for noncemented sand and clay mixtures. In *Crustal Permeability* (John Wiley, p. 539).

- Lund, J. W., & Toth, A. N. (2021). Direct utilization of geothermal energy 2020 worldwide review. *Geothermics*, *90*(November 2020), 101915.
<https://doi.org/10.1016/j.geothermics.2020.101915>
- Lynn, M. S. (1978). *Coastal warm spring systems along northeastern Baja California. (Master's thesis)*. San Diego State University.
- Lyon, G. L., & Giggenbach, W. (1992). The Isotope Geochemistry of Hot Spring Gases and Waters From Coromandel and Hauraki. *Proceeding of 14th New Zealand Geothermal Workshop*, 57–62.
- Magri, F., Akar, T., Gemici, U., & Pekdeger, A. (2012a). Numerical investigations of fault-induced seawater circulation in the Seferihisar-Balçova Geothermal system, western Turkey. *Hydrogeology Journal*, *20*(1), 103–118. <https://doi.org/10.1007/s10040-011-0797-z>
- Marine, I. W. (1979). The use of naturally occurring helium to estimate groundwater velocities for studies of geologic storage of radioactive waste. *Water Resources Research*, *15*(5), 1130–1136. <https://doi.org/10.1029/WR015i005p01130>
- Marone, C. (1995). Fault zone strength and failure criteria. *Geophysical Research Letters*, *22*(6), 723–726. <https://doi.org/10.1029/95GL00268>
- McCaig, A. M. (1988). Deep fluid circulation in fault zones. *Geology*, *16*(10), 867–870.
[https://doi.org/10.1130/0091-7613\(1988\)016<0867:DFCIFZ>2.3.CO;2](https://doi.org/10.1130/0091-7613(1988)016<0867:DFCIFZ>2.3.CO;2)
- McKenna, J. R., & Blackwell, D. D. (2004). Numerical modeling of transient Basin and Range extensional geothermal systems. *Geothermics*, *33*(4), 457–476.
<https://doi.org/10.1016/j.geothermics.2003.10.001>
- Menzies, C. D., Teagle, D. A. H., Craw, D., Cox, S. C., Boyce, A. J., Barrie, C. D., & Roberts, S. (2014). Incursion of meteoric waters into the ductile regime in an active orogen. *Earth and Planetary Science Letters*, *399*, 1–13. <https://doi.org/10.1016/j.epsl.2014.04.046>
- Menzies, C. D., Teagle, D. A. H., Niedermann, S., Cox, S. C., Craw, D., Zimmer, M., et al. (2016). The fluid budget of a continental plate boundary fault: Quantification from the Alpine Fault, New Zealand. *Earth and Planetary Science Letters*, *445*, 125–135.
<https://doi.org/10.1016/j.epsl.2016.03.046>
- Michailos, K., Sutherland, R., Townend, J., & Savage, M. K. (2020). Crustal Thermal Structure and Exhumation Rates in the Southern Alps Near the Central Alpine Fault, New Zealand. *Geochemistry, Geophysics, Geosystems*, *21*(8).

- <https://doi.org/10.1029/2020GC008972>
- Middtømme, K., Roaldset, E., & P., A. (1998). Thermal Conductivity of Selected Claystones and Mudstones from England. *Clay Minerals*, 33(1), 131–145.
<https://doi.org/10.1180/claymin.1998.033.1.12>
- Mitchell, T. M., & Faulkner, D. R. (2009). The nature and origin of off-fault damage surrounding strike-slip fault zones with a wide range of displacements : A field study from the Atacama fault system , northern Chile. *Journal of Structural Geology*, 31(8), 802–816. <https://doi.org/10.1016/j.jsg.2009.05.002>
- Moeck, I. S. (2014). Catalog of geothermal play types based on geologic controls. *Renewable and Sustainable Energy Reviews*, 37, 867–882. <https://doi.org/10.1016/j.rser.2014.05.032>
- Mulligan, A. E., & Charette, M. A. (2009). Groundwater Flow to the Coastal Ocean. *Encyclopedia of Ocean Sciences*, 88–97. <https://doi.org/10.1016/B978-012374473-9.00645-7>
- Na, J., Chi, B., Zhang, Y., Li, J., & Jiang, X. (2019). Study on the influence of seawater density variation on sea water intrusion in confined coastal aquifers. *Environmental Earth Sciences*, 78(24), 1–9. <https://doi.org/10.1007/s12665-019-8684-3>
- Nicholson, K. (1993). *Geothermal Fluids* (Springer New York).
- NOAA National Geophysical Data Center. (2006). Port Ensenada, Mexico Digital Elevation Model - 3 arc-second. Retrieved from <https://data.noaa.gov/waf/NOAA/NESDIS/NGDC/MGG/DEM//iso/>
- Olguín-Martínez, M. G., Peiffer, L., Dobson, P. F., Spycher, N., Inguaggiato, C., Wanner, C., et al. (2022). PyGeoT: A tool to automate mineral selection for multicomponent geothermometry. *Geothermics*, 104(August 2021), 102467.
<https://doi.org/10.1016/j.geothermics.2022.102467>
- Ortega-Rivera, A. (2003). Geochronological constraints on the tectonic history of the Peninsular Ranges batholith of Alta and Baja California: Tectonic implications for western México. *Special Paper of the Geological Society of America*, 374, 297–335.
<https://doi.org/10.1130/0-8137-2374-4.297>
- Ortega-Rivera, A., Suárez-Vidal, F., Mendoza-Borunda, R., & de la O, M. (2018). A multidisciplinary approach to estimate slip rate-magnitude and recurrence time for a segment of a major active fault. Case study: The Agua Blanca Fault, Valle de Agua Blanca, B.C., México. *Journal of South American Earth Sciences*, 88(May), 1–15.

- <https://doi.org/10.1016/j.jsames.2018.08.005>
- Papachristou, M., Dalampakis, P., Arvanitis, A., Mendrinou, D., & Andritsos, N. (2021). Geothermal developments in Greece – Country update 2015-2020, (October), 1–14.
- Pérez-Flores, M. A., Suárez Vidal, F., Gallardo Delgado, L. A., González Fernández, A., & Vázquez, R. (2004). Structural pattern of the Todos Santos Coastal Plain, based on geophysical data. *Ciencias Marinas*, *30*(2), 349–364.
- Peters, D., & Pettke, T. (2017). Evaluation of Major to Ultra Trace Element Bulk Rock Chemical Analysis of Nanoparticulate Pressed Powder Pellets by LA-ICP-MS. *Geostandards and Geoanalytical Research*, *41*(1), 5–28. <https://doi.org/10.1111/ggr.12125>
- Van der Pluijm, B. A., & Marshak, S. (2004). *Earth structure : an introduction to structural geology and tectonics*. W.W. Norton. Retrieved from <https://ben.earth.lsa.umich.edu/ES/>
- Pollack, H. N., Hurter, S. J., & Johnson, J. R. (1993). Heat flow from the Earth's interior: Analysis of the global data set. *Reviews of Geophysics*, *31*(3), 267–280. <https://doi.org/10.1029/93RG01249>
- Polyak, B. G., Kononov, V. I., Fernandez, R., Kamenskiy, I. L., & Zinkevich, V. P. (1991). Helium isotopes in thermal fluids of Baja California and adjacent areas. *International Geology Review*, *33*(12), 1218–1232. <https://doi.org/10.1080/00206819109465747>
- Pruess, K., Oldenburg, C. M., & Moridis, G. J. (1999). TOUGH2 user's guide version 2 (No. LBNL-43134). Lawrence Berkeley National Lab.(LBNL), Berkeley, CA (United States).
- Pruess, Karsten, & Narismhan, T. N. (1985). A Practical Method for Modeling Fluid and Heat Flow in Fractured Porous Media. *Society of Petroleum Engineers Journal*.
- Pruess, Karsten, Oldenburg, C., & Moridis, G. (1999). *TOUGH2 USER'S GUIDE, VERSION 2.0*. Retrieved from <http://citeseerx.ist.psu.edu/viewdoc/download?doi=10.1.1.396.8810&rep=rep1&type=pdf>
- Ranalli, G., & Murphy, D. C. (1987). Rheological stratification of the lithosphere. *Tectonophysics*, *132*(4), 281–295. [https://doi.org/10.1016/0040-1951\(87\)90348-9](https://doi.org/10.1016/0040-1951(87)90348-9)
- Renard, F., Gratier, J. P., & Jamtveit, B. (2000). Kinetics of crack-sealing, intergranular pressure solution, and compaction around active faults. *Journal of Structural Geology*, *22*(10), 1395–1407. [https://doi.org/10.1016/S0191-8141\(00\)00064-X](https://doi.org/10.1016/S0191-8141(00)00064-X)
- RESNOM. (2017). Red Sísmica del Noroeste de México. <https://doi.org/10.7914/SN/BC>
- Reyes, L. M., Rebolgar, C. J., & Castro, R. (2001). Depth of the Moho in northern Baja

- California using (Pg-Pn) travel times. *Geofisica Internacional*, 40(1), 21–29.
- Rimstidt, J. D., & Barnes, H. L. (1980). The kinetics of silica-water reactions. *Geochimica et Cosmochimica Acta*, 44(11), 1683–1699. [https://doi.org/10.1016/0016-7037\(80\)90220-3](https://doi.org/10.1016/0016-7037(80)90220-3)
- Rockwell, T. K., Muhs, D. R., Kennedy, G. L., Hatch, M. E., Wilson, S. M., & Klinger, R. E. (1989). Uranium-series ages, faunal correlations and tectonic deformation of marine terraces within the Agua Blanca fault zone at Punta Banda, northern Baja California, Mexico. In *Los Angeles, Society of Economic Paleontologists and Mineralogists (Pacific Section)* (pp. 1–16).
- Sano, Y., & Wakita, H. (1985). Geographical distribution of He³/He⁴ ratios in Japan: implications for arc tectonics and incipient magmatism. *Journal of Geophysical Research*, 90(B10), 8729–8741. <https://doi.org/10.1029/JB090iB10p08729>
- Sano, Yuji, & Takahata, N. (2005). Measurement of noble gas solubility in seawater using a quadrupole mass spectrometer. *Journal of Oceanography*, 61(3), 465–473. <https://doi.org/10.1007/s10872-005-0055-x>
- Scarpa, R., Tilling, R. I., & Giggenbach, W. F. (1996). Chemical Composition of Volcanic Gases. *Monitoring and Mitigation of Volcano Hazards*, 221–256.
- Seelig, U., & Bucher, K. (2010). Halogens in water from the crystalline basement of the Gotthard rail base tunnel (central Alps). *Geochimica et Cosmochimica Acta*, 74(9), 2581–2595. <https://doi.org/10.1016/j.gca.2010.01.030>
- Seigneur, N., Mayer, K. U., & Steefel, C. I. (2019). Reactive Transport in Evolving Porous Media. *Reviews in Mineralogy and Geochemistry*, 85, 197–238. <https://doi.org/10.2138/rmg.2019.85.7>
- Seyfried, W. E., & Bischoff, J. L. (1979). Low temperature basalt alteration by sea water: an experimental study at 70°C and 150°C. *Geochimica et Cosmochimica Acta*, 43(12), 1937–1947. [https://doi.org/10.1016/0016-7037\(79\)90006-1](https://doi.org/10.1016/0016-7037(79)90006-1)
- Shalev, E., & Yechieli, Y. (2007). The effect of Dead Sea level fluctuations on the discharge of thermal springs. *Israel Journal of Earth Sciences*, 56(1), 19–27. <https://doi.org/10.1560/IJES.56.1.19>
- Shalev, E., Lyakhovskiy, V., & Yechieli, Y. (2007). Is advective heat transport significant at the Dead Sea basin? *Geofluids*, 7(3), 292–300. <https://doi.org/10.1111/j.1468-8123.2007.00190.x>
- Sibson, R. H. (1983). Continental fault structure and the shallow earthquake source. *Journal of*

- the Geological Society*, 140(5), 741–767. <https://doi.org/10.1144/gsjgs.140.5.0741>
- Sibson, Richard H. (1982). Fault zone models, heat flow, and the depth distribution of earthquakes in the continental crust of the United States. *Bulletin of the Seismological Society of America*, 72, 151–163.
- Sibson, Richard H. (1994). Crustal stress, faulting and fluid flow. *Geological Society Special Publication*, 78, 69–84. <https://doi.org/10.1144/GSL.SP.1994.078.01.07>
- Siegfried, S., & Helmut, D. (2004). Physical and Mechanical Properties of Rocks. In Springer Heidelberg Dordrecht London New York (Ed.), *Stone in Architecture* (4th Editio, p. 559). <https://doi.org/10.1007/978-3-642-14475-2>
- Smith, D. L., Nuckels, E. I., Jones, R. L., & Cook, G. A. (1979). Distribution of heat flow and radioactive heat generation in northern Mexico. *Journal of Geophysical Research*, 84(9).
- Snelgrove, S. H., & Forster, C. B. (1996). Impact of seafloor sediment permability and thickness on off-axis hydrothermal circulation: Juan de Fuca Ridge eastern flank. *Journal of Geophysical Research: Solid Earth*, 101(2), 2915–2925. <https://doi.org/10.1029/95jb03115>
- Sonney, R., & Vuataz, F. D. (2008). Properties of geothermal fluids in Switzerland: A new interactive database. *Geothermics*, 37(5), 496–509. <https://doi.org/10.1016/j.geothermics.2008.07.001>
- Steeffel, Carl I., & Maher, K. (2009). Fluid-Rock Interaction: a Reactive Transport approach. *Reviews in Mineralogy & Geochemistry*, 70(1988), 485–532. <https://doi.org/10.2138/rmg.2009.70.11>
- Steeffel, Carl I., DePaolo, D. J., & Lichtner, P. C. (2005). Reactive transport modeling: An essential tool and a new research approach for the Earth sciences. *Earth and Planetary Science Letters*, 240(3–4), 539–558. <https://doi.org/10.1016/j.epsl.2005.09.017>
- Stern, R. J. (2018). The evolution of plate tectonics. *Philosophical Transactions of the Royal Society A: Mathematical, Physical and Engineering Sciences*, 376(2132). <https://doi.org/10.1098/rsta.2017.0406>
- Stipp, M., Stünitz, H., Heilbronner, R., & Schmid, S. M. (2002). The eastern Tonale fault zone: A “natural laboratory” for crystal plastic deformation of quartz over a temperature range from 250 to 700 °C. *Journal of Structural Geology*, 24(12), 1861–1884. [https://doi.org/10.1016/S0191-8141\(02\)00035-4](https://doi.org/10.1016/S0191-8141(02)00035-4)
- Stober, I., Zhong, J., Zhang, L., & Bucher, K. (2016). Deep hydrothermal fluid–rock

- interaction: the thermal springs of Da Qaidam, China. *Geofluids*, 16(4), 711–728.
<https://doi.org/10.1111/gfl.12190>
- Stober, I., & Bucher, K. (2007). Hydraulic properties of the crystalline basement. *Hydrogeology Journal*, 15(2), 213–224. <https://doi.org/10.1007/s10040-006-0094-4>
- Stober, I., & Bucher, K. (1999). Origin of salinity of deep groundwater in crystalline rocks. *Terra Nova*, 11(4), 181–185. <https://doi.org/10.1046/j.1365-3121.1999.00241.x>
- Stober, I., & Bucher, K. (2013). *Geothermal energy: From theoretical models to exploration and development*. (Springer Nature Switzerland AG, Ed.). <https://doi.org/10.1007/978-3-030-71685-1>
- Stober, I., Giovanoli, F., Wiebe, V., & Bucher, K. (2022). Deep hydrochemical section through the Central Alps: evolution of deep water in the continental upper crust and solute acquisition during water–rock–interaction along the Sedrun section of the Gotthard Base Tunnel. *Swiss Journal of Geosciences*, 115(1). <https://doi.org/10.1186/s00015-022-00413-0>
- Storey, M., Rogers, G., Saunders, A. D., & Terrell, D. J. (1989). San Quintín volcanic field, Baja California, Mexico: ‘within-plate’ magmatism following ridge subduction. *Terra Nova*, 1(2), 195–202. <https://doi.org/10.1111/j.1365-3121.1989.tb00352.x>
- Sullivan, M. J. O., & Sullivan, J. P. O. (2016). *Reservoir modeling and simulation for geothermal resource characterization and evaluation*. *Geothermal Power Generation*. Elsevier Ltd. <https://doi.org/10.1016/B978-0-08-100337-4.00007-3>
- Sutherland, R., Townend, J., Toy, V., Upton, P., Coussens, J., Allen, M., et al. (2017). Extreme hydrothermal conditions at an active plate-bounding fault. *Nature*, 546(7656), 137–140. <https://doi.org/10.1038/nature22355>
- Taillefer, A., Guillou-Frottier, L., Soliva, R., Magri, F., Lopez, S., Courrioux, G., et al. (2018). Topographic and Faults Control of Hydrothermal Circulation Along Dormant Faults in an Orogen. *Geochemistry, Geophysics, Geosystems*, 19(12), 4972–4995. <https://doi.org/10.1029/2018GC007965>
- ThinkGeoEnergy. (2022). ThinkGeoEnergy’s Top 10 Geothermal Countries 2022 - Power Generation Capacity (MW). Retrieved August 4, 2023, from <https://www.thinkgeoenergy.com/thinkgeoenergys-top-10-geothermal-countries-2022-power-generation-capacity-mw/>
- Tian, J., Stefánsson, A., Li, Y., Li, L., Xing, L., Li, Z., et al. (2023). Geothermics

- Geochemistry of thermal fluids and the genesis of granite-hosted Huangshadong geothermal system, Southeast China, *109*(October 2022), 1–12.
<https://doi.org/10.1016/j.geothermics.2023.102647>
- Torgersen, T. (1980). Controls on pore-fluid concentration of 4He and ^{222}Rn and the calculation of $4\text{He}/^{222}\text{Rn}$ ages. *Journal of Geochemical Exploration*, *13*(1), 57–75.
[https://doi.org/10.1016/0375-6742\(80\)90021-7](https://doi.org/10.1016/0375-6742(80)90021-7)
- Tóth, J. (1962). A Theory of Groundwater Motion in Small Drainage Basins in Central Alberta, Canada. *Journal of Geophysical Research*, *67*(11).
<https://doi.org/10.1029/jz067i011p04375>
- Tóth, J. (2009). *Gravitational systems of groundwater flow: theory, evaluation, utilization*. Cambridge University Press.
- Truesdell, A. H., Thompson, J. M., Coplen, T. B., Nehring, N. L., & Janik, C. J. (1981). The origin of the Cerro Prieto geothermal brine, *10*(3), 225–238.
- Tsunogai, S. (1975). Sea salt particles transported to the land. *Tellus*, *27*(1), 51–58.
<https://doi.org/10.3402/tellusa.v27i1.9883>
- Upton, P., Craw, D., Yu, B., & Chen, Y. G. (2011). Controls on fluid flow in transpressive orogens, Taiwan and New Zealand. *Geological Society Special Publication*, *359*(1), 249–265. <https://doi.org/10.1144/SP359.14>
- Upton, P., Koons, P. O., & Chamberlain, C. P. (1995). Penetration of deformation-driven meteoric water into ductile rocks: Isotopic and model observations from the Southern Alps, New Zealand. *New Zealand Journal of Geology and Geophysics*, *38*(4), 535–543.
<https://doi.org/10.1080/00288306.1995.9514680>
- Vengosh, A., Heumann, K. G., Juraske, S., & Kasher, R. (1994). Boron isotope application for tracing sources of contamination in groundwater. *Environmental Science & Technology*, *28*(11), 1968–1974.
- Vidal, F. V., Welhan, J., & Vidal, V. M. (1982). Stable isotopes of helium, nitrogen and carbon in a coastal submarine hydrothermal system. *Journal of Volcanology and Geothermal Research*, *12*(1–2), 101–110.
- Vidal, V. M. V., Vidal, F. V., Isaacs, J. D., & Young, D. R. (1978). Coastal submarine hydrothermal activity off northern Baja California. *Journal of Geophysical Research: Solid Earth*, *83*(B4), 1757–1774. <https://doi.org/10.1029/JB083iB04p01757>
- Vidal, V. M. V., Vidal, F. V., & Isaacs, J. D. (1981). Coastal submarine hydrothermal activity

- off northern Baja California: 2. Evolutionary history and isotope geochemistry. *Journal of Geophysical Research: Solid Earth*, 86(B10), 9451–9468.
<https://doi.org/10.1029/JB086iB10p09451>
- Violay, M., Heap, M. J., Acosta, M., & Madonna, C. (2017). Porosity evolution at the brittle-ductile transition in the continental crust: Implications for deep hydro-geothermal circulation. *Scientific Reports*, 7(1), 1–10. <https://doi.org/10.1038/s41598-017-08108-5>
- Waber, H. N., & Smellie, J. A. T. (2008). Characterisation of pore water in crystalline rocks. *Applied Geochemistry*, 23(7), 1834–1861.
<https://doi.org/10.1016/j.apgeochem.2008.02.007>
- Waber, H. N., Schneeberger, R., Mäder, U. K., & Wanner, C. (2017). Constraints on Evolution and Residence time of Geothermal Water in Granitic Rocks at Grimsel (Switzerland). *Procedia Earth and Planetary Science*, 17, 774–777.
<https://doi.org/10.1016/j.proeps.2017.01.026>
- Wanner, C., Peiffer, L., Sonnenthal, E., Spycher, N., Iovenitti, J., & Kennedy, B. M. (2014). Reactive transport modeling of the Dixie Valley geothermal area: Insights on flow and geothermometry. *Geothermics*, 51, 130–141.
<https://doi.org/10.1016/j.geothermics.2013.12.003>
- Wanner, C., Diamond, L. W., & Alt-Epping, P. (2019). Quantification of 3-D Thermal Anomalies From Surface Observations of an Orogenic Geothermal System (Grimsel Pass, Swiss Alps). *Journal of Geophysical Research: Solid Earth*, 124(11), 10839–10854.
<https://doi.org/10.1029/2019JB018335>
- Wanner, C., Waber, H. N., & Bucher, K. (2020). Geochemical evidence for regional and long-term topography-driven groundwater flow in an orogenic crystalline basement (Aar Massif, Switzerland). *Journal of Hydrology*, 581(November 2019).
<https://doi.org/10.1016/j.jhydrol.2019.124374>
- Weiss, R. F. (1971). Solubility of Helium and Neon in Water and Seawater. *Journal of Chemical and Engineering Data*, 16(2), 235–241. <https://doi.org/10.1021/je60049a019>
- Wendt, D. S. (2017). Geothermal desalination GeoVision case study analysis: Multiple effect distillation. *Transactions - Geothermal Resources Council*, 41(October), 277–298.
- Wetmore., P. H., Rocco, M., Fletcher., J. M., Helge, A., James, W., Sean, C., et al. (2018). Slip history and the role of the Agua Blanca fault in the tectonics of the North American–Pacific plate boundary of southern California, USA and Baja California, Mexico.

- Geosphere*, 15.
- Wetmore, P. H., Malservisi, R., Fletcher, J. M., Alsleben, H., Wilson, J., Callihan, S., et al. (2019). Slip history and the role of the Agua Blanca fault in the tectonics of the North American-Pacific plate boundary of southern California, USA and Baja California, Mexico. *Geosphere*, 15(1), 119–145. <https://doi.org/10.1130/GES01670.1>
- Whipp, D. M., & Ehlers, T. A. (2007). Influence of groundwater flow on thermochronometer-derived exhumation rates in the central Nepalese Himalaya. *Geology*, 35(9), 851–854. <https://doi.org/10.1130/G23788A.1>
- White, D. E., Brannock, W. W., & Murata, K. J. (1956). Silica in hot-spring waters. *Geochimica et Cosmochimica Acta*, 10(1–2), 27–59. [https://doi.org/10.1016/0016-7037\(56\)90010-2](https://doi.org/10.1016/0016-7037(56)90010-2)
- Williams, A. E., & Rodoni, D. P. (1997). Regional isotope effects and application to hydrologic investigations in southwestern California. *Water Resources Research*, 33(7), 1721–1729. <https://doi.org/10.1029/97WR01035>
- Xu, T., Samper, J., Ayora, C., Manzano, M., & Custodio, E. (1999). Modeling of non-isothermal multi-component reactive transport in field scale porous media flow systems. *Journal of Hydrology*, 214(1–4), 144–164. [https://doi.org/10.1016/S0022-1694\(98\)00283-2](https://doi.org/10.1016/S0022-1694(98)00283-2)
- Yehya, A., & Rice, J. R. (2020). Influence of Fluid-Assisted Healing on Fault Permeability Structure Journal of Geophysical Research : Solid Earth. *Journal of Geophysical Research: Solid Earth*. <https://doi.org/10.1029/2020JB020553>
- Zijl, W. (1999). Scale aspects of groundwater flow and transport systems. *Hydrogeology Journal*, 7(1), 139–150. <https://doi.org/10.1007/s100400050185>
- Zúñiga, W. M. T. (2010). *Mountain block recharge in the Santo Tomás valley, Baja California, México*. CICESE.
- Zuza, A. V., & Cao, W. (2020). Seismogenic thickness of California: Implications for thermal structure and seismic hazard. *Tectonophysics*, 782–783(March). <https://doi.org/10.1016/j.tecto.2020.228426>

Declaration of consent

on the basis of Article 18 of the PromR Phil.-nat. 19

Name/First Name: Daniel Carbajal Martínez

Registration Number: 20-125-753

Study program: PhD of Science in Earth Sciences

Bachelor Master Dissertation

Title of the thesis: Unraveling the behavior of amagmatic geothermal systems through thermal–hydraulic simulations: insights from the Agua Blanca Fault, Baja California, Mexico

Supervisor: PD Dr. Christoph Wanner and
Prof. em. Dr. Laryn W. Diamond


I declare herewith that this thesis is my own work and that I have not used any sources other than those stated. I have indicated the adoption of quotations as well as thoughts taken from other authors as such in the thesis. I am aware that the Senate pursuant to Article 36 paragraph 1 litera r of the University Act of September 5th, 1996 and Article 69 of the University Statute of June 7th, 2011 is authorized to revoke the doctoral degree awarded on the basis of this thesis.

For the purposes of evaluation and verification of compliance with the declaration of originality and the regulations governing plagiarism, I hereby grant the University of Bern the right to process my personal data and to perform the acts of use this requires, in particular, to reproduce the written thesis and to store it permanently in a database, and to use said database, or to make said database available, to enable comparison with theses submitted by others.

Bern, 03.10.2023

Place/Date

Daniel Carbajal
Martinez
Signature

 Firmado digitalmente por Daniel
Carbajal Martinez
Fecha: 2023.08.02 18:37:10 +02'00'